JOHANNES KEPLER
UNIVERSITY LINZ

Submitted by
Fabian Hummer

Submitted at
Insititute of Applied Physics

Supervisor
Univ. Prof. Dr. Thomas Klar

Co-Supervisor
Dr. Stephan Malbrunot-Ettenauer

October 2019

Investigation of Space Charge Effects in MIRACLS' Proof-of-Principle MR-ToF Device

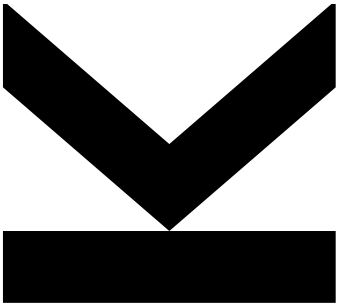

Bachelor Thesis
to obtain the academic degree of
Bachelor of Science
in the Bachelor's Program
Technische Physik

JOHANNES KEPLER UNIVERSITY LINZ
Altenbergerstraße 69
4040 Linz, Österreich
www.jku.at
DVR 0093696

Eidesstattliche Erklärung

Ich erkläre an Eides statt, dass ich die vorliegende Bachelorarbeit selbstständig und ohne fremde Hilfe verfasst, andere als die angegebenen Quellen und Hilfsmittel nicht benutzt bzw. die wörtlich oder sinngemäß entnommenen Stellen als solche kenntlich gemacht habe. Die vorliegende Bachelorarbeit ist mit dem elektronisch übermittelten Textdokument identisch.

Fabian Hummer

Acknowledgement

I'd like to thank my supervisor Stephan Malbrunot-Ettenauer for the awesome opportunity to do my Bachelor thesis at MIRACLS and for the huge amount of time and effort he put into explaining new stuff to me. My time at MIRACLS was an amazing experience and I am glad that I was able to learn so many new things. I also want to thank everyone from the MIRACLS team for their friendly help and support. Special thanks to Peter Plattner for showing me how MIRACLS' simulation files work, to Hanne Heylen and Varvara Lagaki for supporting me with my measurements and my work on the proof-of-principle setup and to Simon Lechner helping me with the data evaluation. Many thanks to Simon Sels and Maxime Mougeot for many discussions about MagneToF detectors and many thanks to the CRIS experiment for lending a MagneToF detector to MIRACLS which was crucial for the final part of my thesis. Moreover, I want to thank Mark Bissell for explaining the optical detection region of COLLAPS to me and helping me with the optical detection simulations. Finally, I want to thank Prof. Thomas Klar for making it possible for me to do my Bachelor thesis at MIRACLS.

Abstract

Over the last years, Electrostatic Ion Beam Traps (EIBT), especially in their function as Multi-Reflection Time-of-Flight (MR-ToF) mass spectrometers, have significantly gained in importance within the ion storage community. MR-ToF devices confine an ion bunch at a defined kinetic energy of typically a few kiloelectronvolts between two electrostatic mirrors. As versatile tools, they are used in various physics fields and have become indispensable for mass spectrometry and mass separation in nuclear physics.

An innovative application of the MR-ToF technique is the Multi Ion Reflection Apparatus for Collinear Laser Spectroscopy MIRACLS, an experimental apparatus located at the radioactive ion beam facility ISOLDE/CERN. The aim of the novel MIRACLS concept is to increase the sensitivity of high-resolution laser spectroscopy measurements by performing the latter technique on trapped ions. This will allow MIRACLS to study exotic short-lived radionuclides produced with very low quantities at ISOLDE which are currently out of reach of conventional methods. Hence, MIRACLS promises to deliver valuable new data for nuclear physics research.

During first measurements on MIRACLS' proof-of-principle setup, it has been observed that high charge densities inside the trap change the characteristics of the ion bunch – so-called **space charge** effects. A particularly interesting phenomenon is **self-bunching**, which makes an ion bunch in the MR-ToF keep its narrow time spread in situations where it would normally disperse. It has soon become apparent that a better understanding of these effects is needed as they will play a role in future measurements.

The investigation of these space charge effects has been the subject of this bachelor thesis. For this purpose, two MagneToF ion detectors have been characterized and the simulations of ion trajectories in MIRACLS' proof-of-principle MR-ToF have been improved. In the following, the experimental methods will be described and recent measurement results will give a new insight into different space charge effects in MIRACLS' MR-ToF device.

Zusammenfassung

In den letzten Jahren haben Elektrostatische Ionenfallen an Bedeutung für die Speicherung von Ionen gewonnen, insbesondere als MR-ToF (Abkürzung für engl. Multi-Reflection Time-of-Flight) Massenspektrometer. Mittlerweile sind sie ein unentbehrliches Werkzeug für Massenspektrometrie und Massenseparation in der Kernphysik geworden. In MR-ToF Apparaten oszillieren Ionenbündel mit einer definierten kinetischen Energie zwischen zwei elektrostatischen Spiegeln.

Eine innovative Anwendung der MR-ToF-Technik ist der Multi Ion Reflection Apparatus for Collinear Laser Spectroscopy MIRACLS. Dieses Experiment ist am ISOLDE, einer Einrichtung zur Erzeugung von radioaktiven Ionenstrahlen am CERN, beheimatet. Das Ziel von MIRACLS ist es, die Sensitivität von hochauflösender Laserspektroskopie (CLS) zu verbessern, indem diese Messungen an Ionen in der Falle durchgeführt werden und so die Beobachtungszeit erhöht wird. Dadurch wird es MIRACLS möglich sein, exotische Isotope zu untersuchen, die am ISOLDE nur mit sehr geringer Ausbeute produziert werden können und so wertvolle neue Daten für die Kernforschung zu liefern.

Während erster Messungen am MIRACLS-Pilotaufbau wurde beobachtet, dass hohe Ladungsdichten innerhalb des MR-ToF Gerätes das Verhalten der gefangenen Ionen beeinflussen – sogenannte Space Charge Effekte. Ein besonders interessantes Phänomen ist Self-Bunching, bei dem die Ionenbündel durch die gegenseitige Coulomb-Abstoßung zusammenbleiben, ohne Interaktion aber auseinanderlaufen würden. Da diese Effekte auch bei zukünftigen Messungen eine Rolle spielen werden, ist es wichtig, Space Charge Effekte besser zu verstehen.

Ziel dieser Bachelorarbeit war die Untersuchung der Space Charge Effekte im MIRACLS-Pilotexperiment. Dazu wurden MagneToF-Ionendetektoren in Betrieb genommen und charakterisiert und bestehende Simulationen der Ionenflugbahnen im MR-ToF Gerät von MIRACLS verbessert. Im Folgenden werden die experimentellen Methoden beschrieben und neue Messergebnisse vorgestellt, die einen besseren Einblick in verschiedene Space Charge Effekte geben.

Contents

1 Introduction **9**

2 Experimental Background and Concepts **11**
2.1 ISOLDE . . . 11
2.2 Laser Spectroscopy . . . 12
2.2.1 Hyperfine Interaction . . . 12
2.2.2 Collinear Laser Spectroscopy . . . 12
2.3 Linear Paul Trap . . . 14
2.4 MR-ToF Devices . . . 15
2.5 MIRACLS . . . 17
2.6 Electron Multipliers . . . 18
2.6.1 Photo Multiplier Tubes . . . 18
2.6.2 Microchannel Plates . . . 19
2.6.3 MagneToF Detectors . . . 19

3 MIRACLS' Proof-of-Principle Setup **21**
3.1 Paul Trap Operation . . . 22
3.2 Ion Species Used in the Proof-of-Principle Experiment . . . 22
3.3 Collisional Excitation . . . 23
3.4 Summary of Previous Work and Open Questions . . . 24
3.4.1 MR-ToF Operation . . . 25
3.4.2 Space Charge Effects in an MR-ToF Device . . . 25

4 Characterization of MagneToF Detectors **28**
4.1 Characterization of the First MagneToF Detector with Ca^+ ions . . . 29
4.1.1 Finding the Correct Operation Voltage . . . 29
4.1.2 Single Ion Peak Measurements . . . 31
4.1.3 Integration Over Multiple Peaks . . . 33
4.1.4 Comparison of Characterization Methods . . . 39
4.1.5 Measuring the Mean Peak Area for one Ion . . . 39
4.2 Characterization Procedures applied to Mg^+ ions . . . 39
4.2.1 Characterization procedure . . . 39
4.2.2 Re-Characterization of the First MagneToF with Mg^+ ions . . . 40
4.2.3 Characterization of the Second MagneToF with Mg^+ ions . . . 40
4.2.4 Detector Efficiency . . . 41
4.3 Linearity of the First MagneToF . . . 42
4.3.1 Working Principle of the Linearity Measurements . . . 42
4.3.2 First Loading Time Scans . . . 42

4.3.3 Cooling Time Scan . . . 43
4.3.4 Steer the Ion Beam . . . 44
4.3.5 Conclusion . . . 44

5 Simulation of Fluorescence Light Detection in the MR-ToF Device 46
5.1 Simulations of Photon Traces in the ODR . . . 47
5.1.1 Position Dependent Detection Efficiency of the Optical Detection Region 47
5.1.2 Other Applications . . . 48
5.2 SIMION Simulations of Ion Trajectories in the MR-ToF Device . . . 49
5.2.1 Simulation of Space Charge Effects . . . 50
5.2.2 Output of the SIMION Simulations . . . 50
5.2.3 Residual Gas in the MR-ToF Device . . . 51
5.3 Simulating the Time Profile of Fluorescence Emitting Ions Passing the ODR . 51
5.3.1 Calculation of Ion Positions in the Optical Detection Region . . . 51
5.3.2 Simulation of the Optical Detection of Fluorescence Light . . . 52
5.3.3 Comparison of Ion Bunch Width and Fluorescence Signal Width . . . 52

6 Study of Ion Bunch Properties in the MR-ToF Device 55
6.1 Collisional Excitation Measurements . . . 55
6.2 First Benchmark of Simulations with Small Numbers of Stored Ions . . . 57
6.2.1 Possible Reasons for the Disagreements . . . 57
6.2.2 Findings in the Second Collisional Excitation Campaign . . . 61
6.2.3 Impact on Further Measurements and Simulations . . . 61
6.3 Space Charge Effects Predicted by the Simulation . . . 62
6.3.1 Isochronous Area . . . 62
6.3.2 Non-Isochronous, Self-Bunching Area . . . 62
6.3.3 Left Non-Isochronous Area . . . 63
6.4 Space Charge Effects Observed Experimentally . . . 64
6.4.1 Comparison Between Experiment and Simulation . . . 64
6.4.2 Isochronous Area . . . 65
6.4.3 Non-Isochronous, Self-Bunching Area . . . 66
6.4.4 Left Non-Isochronous Area . . . 67
6.4.5 Disagreements Between Experiment and Simulations . . . 68
6.5 Conclusion . . . 68

7 Summary and Conclusion 70

A MagneToF Mini 14924 Datasheet 73

B Further Analysis of MagneToF Measurements 76
B.1 Further Comparison Between Characterization Methods . . . 76
B.2 Investigation of Non-Linearities: Steering the Ion Beam . . . 80

C MagneToF Procedures 82
C.1 Characterization of a New MagneToF Detector . . . 82
C.2 Measuring the Number of Ions in an Ion Bunch . . . 84

D Second Collisional Excitation Campaign 87
D.1 Ion Numbers in Collisional Excitation Measurements . . . 87

D.2 Trapping Efficiency of the MR-ToF Device 89

E Additional Information on the Ray Tracer 91
E.1 Other Applications of the Ray Tracer 91
E.1.1 Finding the Optimal Distance Between PMT and Lens 2 91
E.1.2 Aperture in Front of Lens 1 92
E.2 Emission Patterns 95
E.3 Documentation of the COLLAPS Ray Tracer 95

F Documentation of the Collisional Excitation Data Fitting Tool 102
F.1 A Few Words on Lmfit 102
F.2 Peak Shapes 103
F.3 Work flow of the Collisional Excitation Data Fitting Tool 104
F.3.1 Fitting Experimental Data 104
F.3.2 Fitting Simulation Data 105
F.4 How To Use the Collisional Excitation Data Fitting Tool 105
F.4.1 Example Usage: Step-by-Step Code 105
F.4.2 The Fit Parameter Config Object 107
F.4.3 Further Options and Functions 110

Bibliography 112

Chapter 1

Introduction

The **M**ulti **I**on **R**eflection **A**pparatus for **C**ollinear **L**aser **S**pectroscopy (MIRACLS), located at the radioactive ion beam facility ISOLDE/CERN, is a novel approach to increase the sensitivity of high-precision laser spectroscopy in order to probe short lived radionuclides. This is achieved by storing the singly charged ions of these radionuclides in an electrostatic ion beam trap, often also called Multi-Reflection Time-of-Flight device (MR-ToF), where the ions are confined between two electrostatic mirrors at a defined kinetic energy. In every revolution, they pass an optical detection region used for the laser spectroscopy measurement, which increases the observation time and leads to an improvement in sensitivity between 20 and 600, compared to conventional collinear laser spectroscopy techniques [1]. This increase in sensitivity is particularly important when radioactive isotopes are to be studied which are generally produced in minute quantities.

While collinear laser spectroscopy is a well-established technique used since the eighties to investigate the nuclear structure of radioactive isotopes, MR-ToF devices are a relatively new addition to nuclear physics or rare isotopes. In this field, important applications of MR-ToF devices are mass separation and mass spectroscopy. More generally, they are also used in a wide rage of other research areas, such as atomic and molecular physics or cluster studies [2].

When large numbers of ions are injected into an MR-ToF device, the electrostatic repulsion due to the Coulomb force between the ions significantly alters the ions' trajectories inside the trap and hence, the global behaviour of the ion cloud. An especially interesting example for such a space charge effect is **self-bunching** [3], in which the ion bunch keeps its narrow time spread under conditions where it would disperse without the space charge of the ion cloud. It has been observed that space charge effects and self-bunching can occur in MIRACLS' MR-ToF device and may be important in future measurements.

With the introduction of an optical detection region in the center of the MIRACLS MR-ToF device, not only laser-induced fluorescence but also photons arising from collisions between ions and the residual gas can be detected. This collisionally induced fluorescence, also called collisional excitation in the rest of this thesis, has been shown to be a powerful diagnostic tool to investigate self-bunching [3]. Indeed, measurements have qualitatively confirmed the occurrence of self-bunching. However, for detailed and quantitative studies, knowledge about the absolute number of stored ions is required. This information has been missing in previous studies, as the ion detectors still needed to be calibrated.

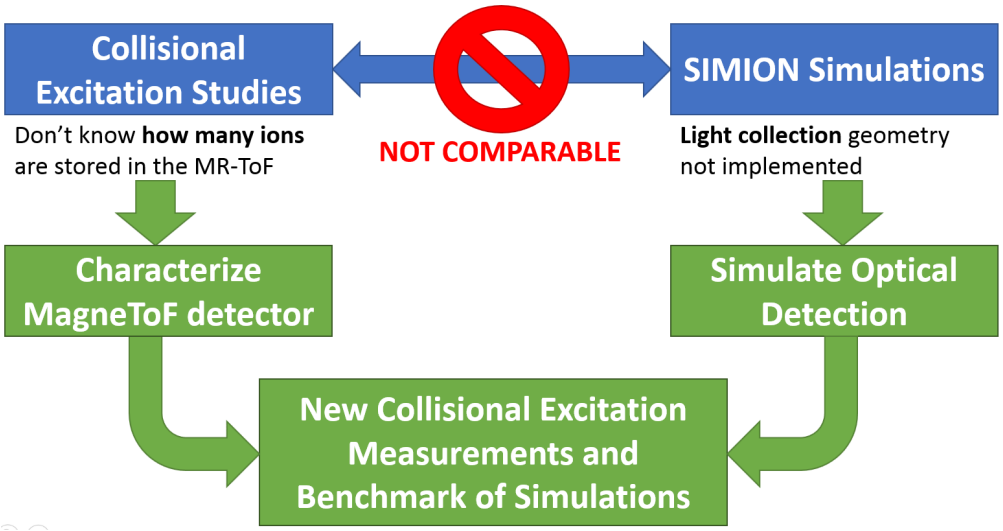

Figure 1.1: *Overview of the three different parts of this thesis.*

To learn more about the properties of an ion bunch in the MR-ToF, also simulations of ion trajectories have been conducted using SIMION. For these simulations, the number of ions is well known, but the results are not comparable to the experimental results as the details of the optical detection are not considered in the simulation process.

The goal of this thesis is to advance the investigation of space charge effects in the MR-ToF of MIRACLS' proof-of-principle setup in order to obtain the first quantitative comparisons between experimental data and simulation. For the future work at MIRACLS, it is essential to know under which conditions space charge effects can occur and how they can be employed to advantage or how they can be avoided.

Chapter 2 gives a short overview of MIRACLS and techniques and devices used throughout this thesis. An overview of the current status of research on space charge in MR-ToF devices and of the experimental setup used for the work on this thesis can be found in chapter 3.

The main part of this thesis has been divided into three different chapters, which are also visualized in figure 1.1:

- As mentioned before, the number of ions in the MR-ToF device needs to be known. For this purpose, new MagneToF detectors have been installed and characterized as described in chapter 4.
- Simulations of ion trajectories in the MR-ToF apparatus need to deliver results that are quantitatively comparable to experimental data. Chapter 5 describes how the simulations have been improved so that they generate a time resolved response using the characteristics of the optical detection region inside of the MR-ToF device.
- Finally, new collisional excitation measurements have been conducted during which the MagneToF detectors have been used to determine the number of ions in the MR-ToF device. A benchmark of the simulations and observed space charge effects are discussed in chapter 6.

Chapter 2

Experimental Background and Concepts

This chapter introduces the basic concepts and experimental techniques used throughout this thesis.

2.1 ISOLDE

The **I**sotope **S**eparator **O**n **L**ine **D**evice (ISOLDE) is a radioactive ion beam (RIB) facility at the European Organization for Nuclear Research (CERN). It is a world-leading laboratory for the production and studies of short lived radioactive nuclei.

In the ISOLDE target area, high-energy protons impinge on a target material and via spallation, fission or fragmentation reactions, radioactive nuclides are produced. These nuclides are extracted from the target, ionized and separated by mass so that the outgoing ion beam contains one specific nuclide with ideally little contaminants. ISOLDE can deliver beams of more than 700 different nuclides with production yields ranging from 1 to more than 10^{10} ions per second. These beams are delivered to various experimental stations from many different fields, such as nuclear physics and fundamental physics to solid state physics, astrophysics and life sciences [4].

The first ISOLDE experiments were performed in 1967 using protons from CERN's *Synchro-cyclotron* (SC). The facility moved to a new hall in 1992 and is since provided with 1.4 GeV [5] protons from the *Proton Synchrotron Booster* [6],[7]. In more than 50 years of operation, ISOLDE has achieved remarkable results for nuclear physics by extending our knowledge of the nuclear structure in many different areas of the nuclear chart.

Since the late eighties, an important contribution to nuclear research is the COLLAPS experiment at ISOLDE, performing high precision measurements of the atomic hyperfine structure using collinear laser spectroscopy. A novel approach to increase the sensitivity of this technique is MIRACLS, an experimental setup also located at ISOLDE. It is introduced in section 2.5 and a detailed description can be found in chapter 3.

2.2 Laser Spectroscopy

2.2.1 Hyperfine Interaction

The hyperfine interaction causes the splitting of atomic energy levels due to electromagnetic interactions between the atomic nucleus and its surrounding electrons [8]. Laser spectroscopy gives direct access this hyperfine structure, as shown in figure 2.1. When scanning the laser frequency and measuring the emission of fluorescence from the atoms or ions, resonant transitions appear as peaks of high intensity.

From the measured hyperfine structure, one can determine nuclear ground state properties such as

- nuclear spin,
- magnetic dipole moment,
- electric quadruple moment and
- mean-square charge radius.

Hyperfine splitting contains information on the nuclear properties but does not depend on any nuclear models. This makes data obtained from laser spectroscopy a valuable tool for nuclear physics research.

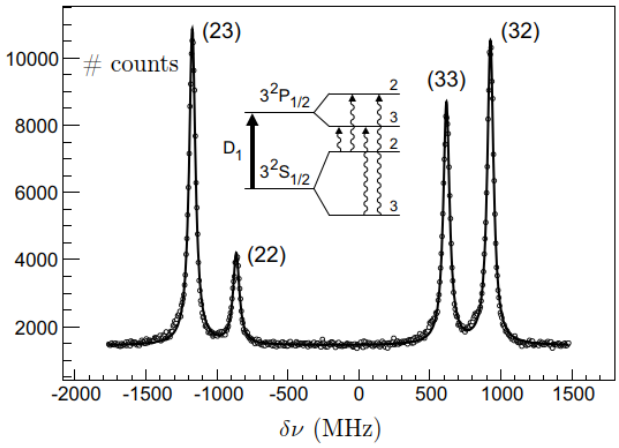

Figure 2.1: *Hyperfine splitting of the D_1 line in the $^{25}Mg^+$ ion energy levels and the corresponding spectrum. Every peak arises due to one resonant transition between two levels as indicated by the level scheme in the center of the figure. Figure adapted from [9].*

2.2.2 Collinear Laser Spectroscopy

Collinear Laser Spectroscopy (CLS) allows the measurement of the atomic hyperfine structure with high resolution. As shown in figure 2.2, a fast ion beam is overlapped with a laser beam (thus the name *collinear* laser spectroscopy), which leads to sufficiently long interaction times between ions and laser light [10]. The laser light is set to an accurate wavelength so that it can excite specific transitions in the hyperfine spectrum. Upon de-excitation, resonance fluorescence photons are detected with PMTs in the optical detection region. Depending on

the application, a charge exchange cell can neutralize the ions before they enter the optical detection region. This way, neutral atoms are measured instead of ions.

The COLLAPS experiment at ISOLDE/CERN, shown in figure 2.2, has pioneered the field of CLS since the eighties.

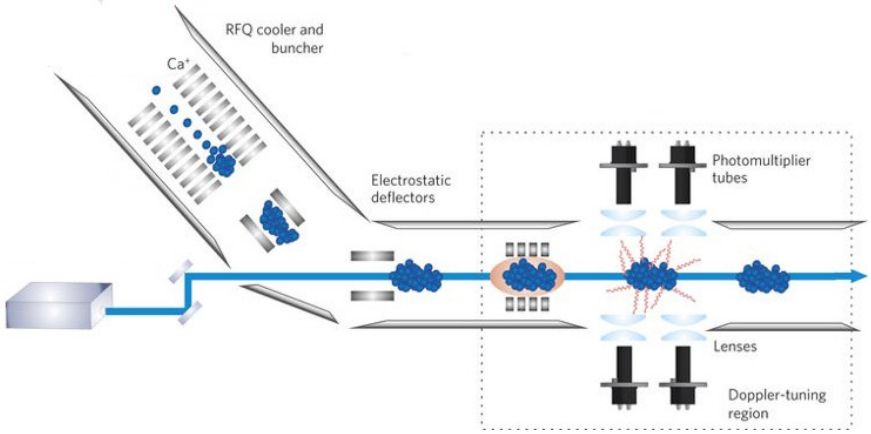

Figure 2.2: *Outline of the COLLAPS experiment at ISOLDE/CERN as an example of a CLS setup. Figure adapted from [11].*

In many applications of CLS, the laser is locked to a well known reference frequency. Instead of scanning the laser frequency, the kinetic energy of the ions or atoms is scanned by changing the acceleration voltage. Due to the Doppler effect, the excitation frequency of the ions or atoms shifts with the kinetic energy according to

$$\nu = \nu_L \cdot (1 + \alpha \pm \sqrt{2\alpha + \alpha^2}) \tag{2.1}$$

with

$$\alpha = \frac{E_{kin}}{m \cdot c^2} \tag{2.2}$$

where ν is the observed frequency, ν_L is the laser frequency, m is the mass of the ion and E_{kin} is the kinetic energy of the ions. In equation 2.1, the '$\pm$' sign is negative for collinear laser spectroscopy (ions travelling in the same direction as laser beam) and positive for anti-collinear laser spectroscopy (ions travelling in opposite direction). This technique is called **Doppler tuning** [12].

The longitudinal velocity spread has to be reduced as far as possible to achieve the narrow line widths that are required to be able to resolve the hyperfine structure. This is done by accelerating the ion beam before it reaches the CLS setup. With an acceleration voltage of 30 kV, the line width can be reduced to a level that is similar to the natural line width [12].

The sensitivity of the experiment can be further improved by using bunched ion beams. A cooler and buncher linear Paul trap as described in section 2.3 improves the emittance of the beam. This leads to a better laser-ion-overlap in the optical detection region.

The main advantage of a bunched beam in CLS is background suppression. The main source of background in CLS is laser stray light and dark counts in the PMT [13]. Both represent

a continuous background sources, by gating the signal from the PMTs on the narrow ion bunch, the background counts can be reduced significantly, as shown in figure 2.3.

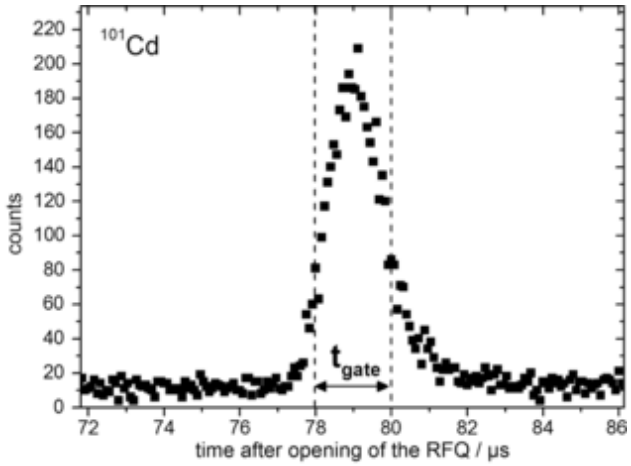

Figure 2.3: *Time gating of a CLS measurement reduces background photons. Figure taken from [13].*

2.3 Linear Paul Trap

A Paul trap is a radio frequency ion trap named after the physicist Wolfgang Paul who invented the trap and shared the Nobel price in 1989 for the development of the ion trap technique [14].

By using only electrostatic fields, it is not possible to confine charged particles in all three spatial directions. This restriction is known as *Earnshaw's theorem* [15]. In a Paul trap however, ions are confined in an alternating electric field.

Figure 2.4 shows a cloud of positively charges ions in an alternating quadrupole field. As the field is inhomogeneous, the average force acting on the particle is not zero. If the frequency and amplitudes of the quadrupole field are configured correctly, the net field can be convergent towards the center [16].

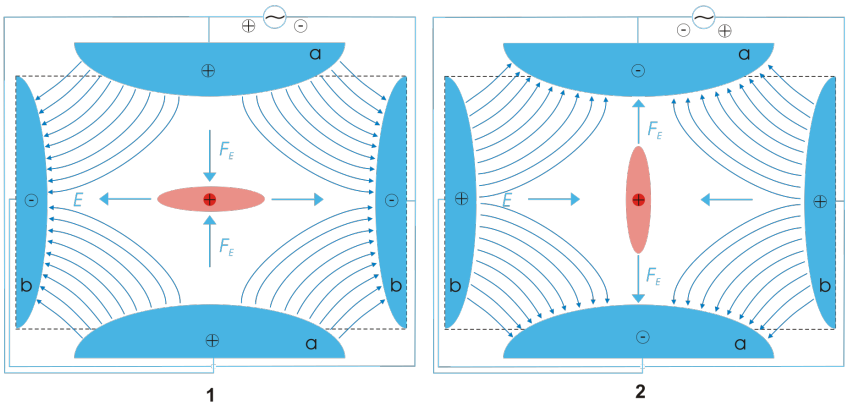

Figure 2.4: *Charged particles in an electric quadrupole field. Figure taken from [17].*

A widely used type of Paul traps is a **linear Paul trap** as shown in figure 2.5. This Paul trap consists of four quadrupole rods for radial confinement. The rods are separated into

different segments with different DC voltages applied in addition to the radio frequency AC voltage for the alternating quadrupole field. The different segment voltages result in an axial potential well as shown in figure 2.5 to establish the axial confinement.

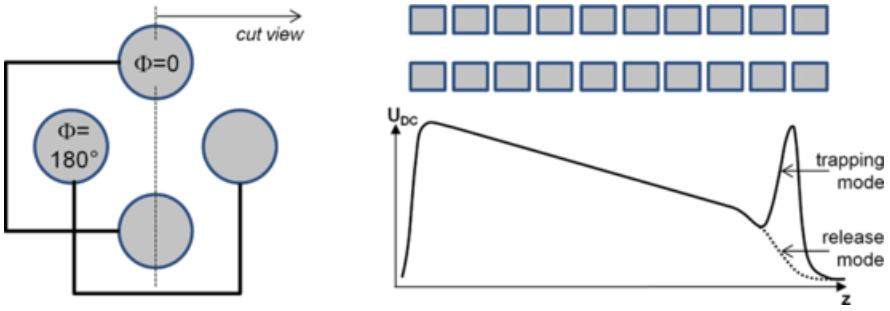

Figure 2.5: *Schematic representation of a linear Paul trap. Figure taken from [13].*

When filled with a Helium buffer gas, a linear Paul trap as shown in figure 2.5 can operate as **cooler and buncher**. This means that the trap collects ions, cools them through collisions with the buffer gas so that they stay in the potential well until the ions are released in well defined ion bunches [16]. The release mechanism is also shown in figure 2.5. The electric potential of the last segment can be switched from a higher to a lower voltage, so that the trap is open on one side. The resulting axial potential accelerates the ion bunch out of the trap.

2.4 MR-ToF Devices

In addition to the use of Paul traps at radioactive ion beam facilities, a new type of ion trap has gained significant importance in rare isotope science during the last years: A Multi-Reflection Time-of-Flight device (MR-ToF) is an electrostatic ion beam trap (EIBT) that captures ions by reflecting them between two electrostatic mirrors. In the case of an MR-ToF device, the Earnshaw theorem does not apply because the kinetic energy of the ions is not zero and therefore the electric field is changing in the frame of reference of the ions [18].

As an example, figure 2.6 shows the mass spectrometry setup of the MR-ToF device of the ISOLTRAP collaboration at ISOLDE/CERN [19]. The electrostatic mirrors consist of different electrodes that do not only reflect, but also radially focus the ion beam. The central drift section is kept on the constant potential of the drift tube, an electrode that encases the drift section.

To inject ions into the MR-ToF device and to release them from the trap afterwards, two different techniques are employed:

- The principle of the **mirror switching** technique is straightforward: When an ion bunch reaches the MR-ToF device, the injection mirror is switched down so that the ions can pass into the MR-ToF apparatus. Similarly, the ion bunch can be ejected from the trap by switching down a mirror again later. These processes are illustrated in the left part of figure 2.7.
- Another method is to use an **in-trap potential lift**. In this case, the mirror potentials always stay constant and the ions are injected with a kinetic energy high enough to

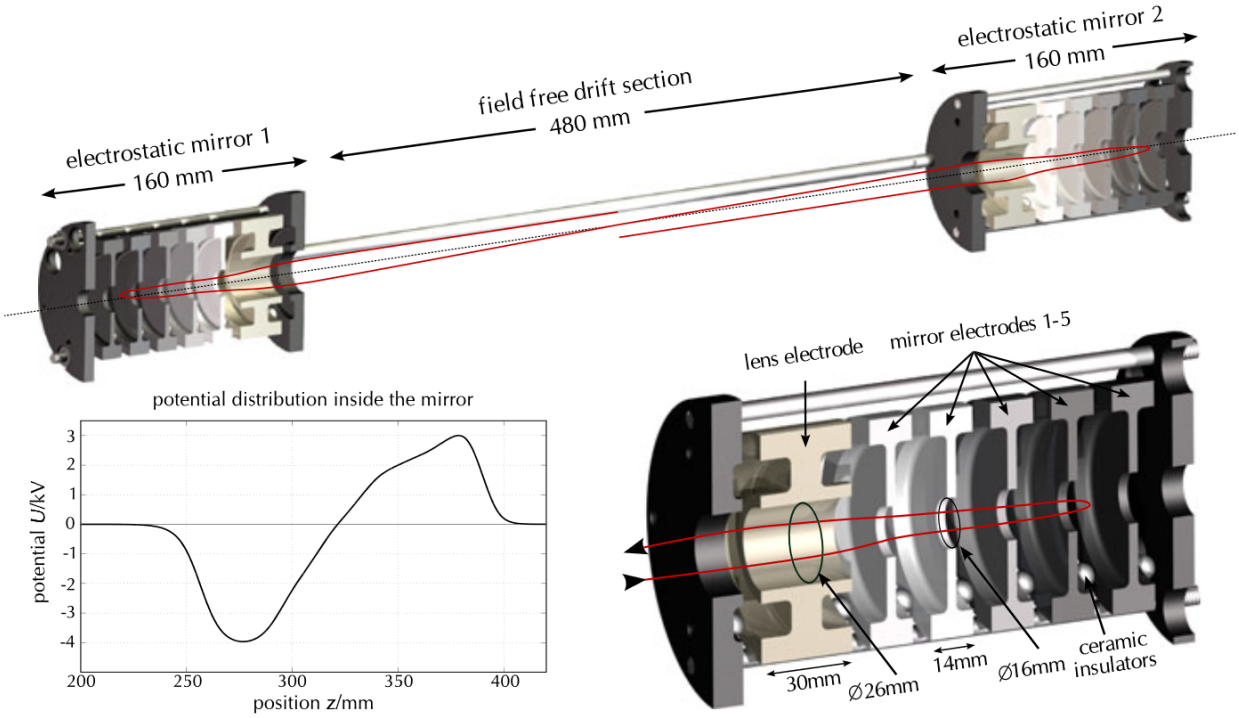

Figure 2.6: *Overview of the MR-ToF device used at ISOLTRAP and a detailed view of one mirror. A possible ion trajectory is drawn in red. Figure taken from [19].*

overcome the mirrors. Initially, the central drift tube is biased to a potential $U_{Lift} \neq 0$. When the ions enter this in-trap lift electrode, their kinetic energy is reduced by $q \cdot U_{Lift}$. As soon as the ion bunch is in the in-trap lift tube, the lift potential is switched to ground ($U_{Lift} = 0$) so that the ions can not overcome the mirror potentials any more. The ejection of the ion bunch works vice versa. The in-trap lift technique is illustrated in the right part of figure 2.7.

Although the in-trap lift technique comes with some technical difficulties, it has several advantages over the mirror switching technique. For example, the sensitive mirror potentials can be easier stabilized if they are kept at a constant voltage all the time.

As already mentioned above, the initial value of the in-trap lift potential determines the ions' energy inside of the MR-ToF device. This means that the energy of the ions inside of the MR-ToF device can be easily adjusted by changing the initial lift potential U_{Lift} [20]. The in-trap lift technique and the lift potential are important concepts used throughout this thesis.

MR-ToF devices have a wide range of applications. Many current works focus on mass separation and mass spectroscopy, but there are also applications in atomic, molecular, and cluster studies [2]. An innovative application of an MR-ToF device is the **M**ulti **I**on **R**eflection **A**pparatus for **C**ollinear **L**aser **S**pectroscopy (MIRACLS), an experimental setup located at the ISOLDE facility, which aims to take advantage of the powerful MR-ToF capabilities for the purpose of collinear laser spectroscopy.

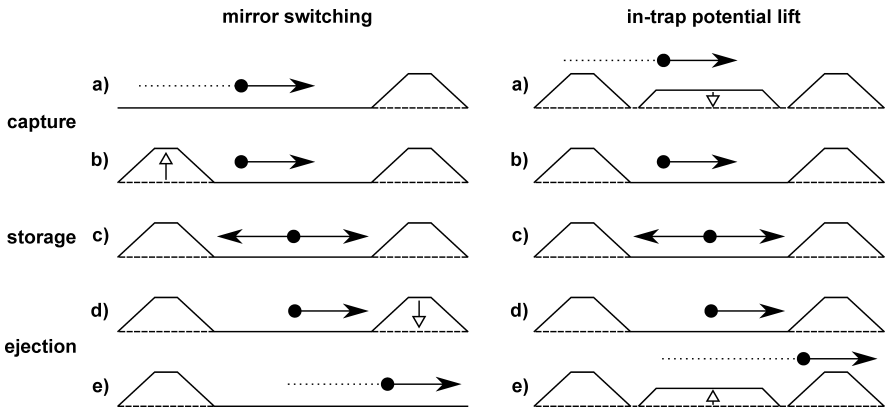

Figure 2.7: *Different techniques to capture ions in an MR-ToF device. Figure taken from [20].*

2.5 MIRACLS

The **M**ulti **I**on **R**eflection **A**pparatus for **C**ollinear **L**aser **S**pectroscopy (MIRACLS) is a novel approach to enhance the sensitivity of collinear laser spectroscopy in order to study those exotic nuclides which are not accessible by conventional techniques.

In collinear laser spectroscopy as it is performed in facilities around the world, every ion bunch passes the optical detection region only once. At MIRACLS, the optical detection region is located in the central drift tube of an MR-ToF device. Therefore the ion bunch can be trapped and passes the optical detection region multiple times. The principle is outlined in figure 2.8.

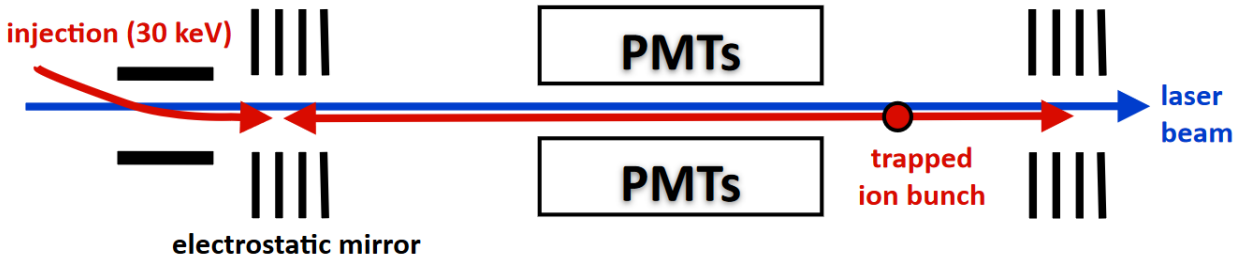

Figure 2.8: *Schematic setup of MIRACLS. An ion bunch is injected into an electrostatic ion beam trap (MR-ToF). The bunch is then reflected between two mirrors and passes the optical detection region with the PMTs multiple times. Figure taken from [1].*

The half-lives of the nuclides produced at RIB facilities like ISOLDE range from several milliseconds up to years or even stable isotopes, while the observation time in CLS is typically a few microseconds [21]. By trapping the ions and thus increasing the observation time, MIRACLS can improve the experimental sensitivity of laser spectroscopy by a factor of 20 up to 600 compared to conventional CLS. The improvement factor is typically limited by the half-life of the nuclide under study which limits the storage time in the MR-ToF device [1].

To demonstrate the concept of MIRACLS and to investigate the properties of laser spectroscopy in an MR-ToF device, a **proof-of-principle (PoP) setup** has been built (see chapter 3). The proof of principle setup receives an ion beam from an offline ion source. As contemporary MR-ToF devices operate with low beam energies of a few keV, typically

around 1.5 keV in MIRACLS' PoP setup, CLS can only be performed at low resolution.

However, In order to maintain the high resolution of conventional CLS, MIRACLS' faster MR-ToF apparatus is planned to operate with 30 keV ion beams from ISOLDE. The **30 keV setup** is being designed right now. It will be ready at the end of the current long term shutdown LS2 of the CERN accelerators, i.e. the beginning of 2021 [22].

2.6 Electron Multipliers

An essential part of this thesis is the understanding about the behaviour of ions and photons inside MIRACLS' proof-of-principle setup. Experimental investigations of these questions require sensitive particle and light detectors. Detectors based on electron multipliers are indispensable tools for many experimental fields and this section shall give a brief overview of the devices used for the work on this thesis.

Electron multipliers are electrode configurations that multiply incident electrons by creating secondary electrons. The electrodes where secondary electron emission takes place are called *dynodes*. Between the dynodes, electric potentials are applied to accelerate the electrons. With different dynode configurations and different sources of initial electrons, particle or light detectors can be created and all of them require good vacuum qualities for operation.

2.6.1 Photo Multiplier Tubes

Photomultiplier tubes (PMT) are electron tubes that are used as highly sensitive photon detectors. The whole working principle is shown in figure 2.9. The initial electrons are created on a photocathode using the photoelectric effect. These initial electrons are amplified with an array of electron multiplier dynodes. The secondary electrons then hit the anode where the signal can be read out. To maintain the vacuum conditions required for operation, PMTs are placed in vacuum tubes [23].

At MIRACLS, a PMT is used in the optical detection region in order to detect photons emitted from laser-excited ions.

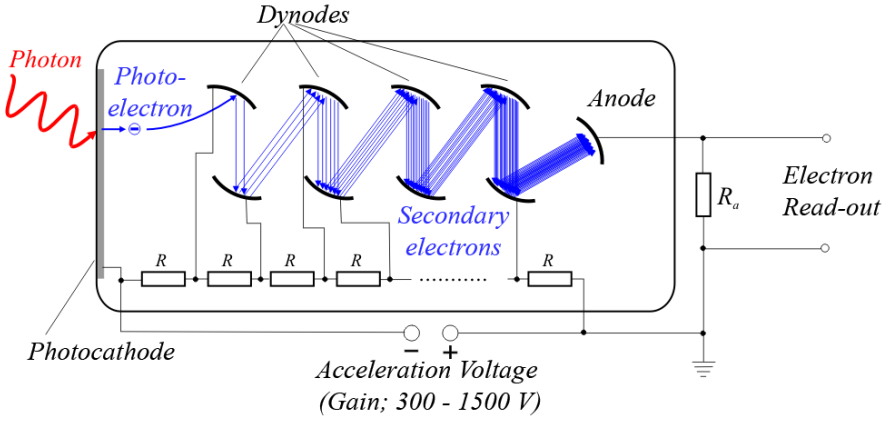

Figure 2.9: *Operation principle of a photomultiplier tube (PMT). See text for details. Figure taken from [24].*

2.6.2 Microchannel Plates

A microchannel plate (MCP) is an electron multiplier with a special continuous dynode configuration. They are widely used as particle detectors but they can also function as the electron multiplier section of a PMT [23].

A MCP is a plate made of a highly insulating material (e.g. lead glass). The operation principle in shown in figure 2.10. The plate is perforated by channels that are typically 10 µm in diameter. The channels are parallel to each other and their inner surfaces are treated with a semiconductor material so that they can operate as a secondary electron emitter. In many applications, the channels are not perpendicular to the plate surface but have a slight angle to the surface. This avoids feedback from positive ions which occasionally form in the channels and are accelerated in the other direction [23].

Multichannel plates can be stacked over one another to increase the overall gain factor.

At MIRACLS' proof-of-principle experiment, an MCP has been used for the detection of ions. However, if too many ions are within an ion bunch, the response of the MCP starts to become non-linear or even saturates. Hence, it is difficult to determine the absolute ion number in this regime.

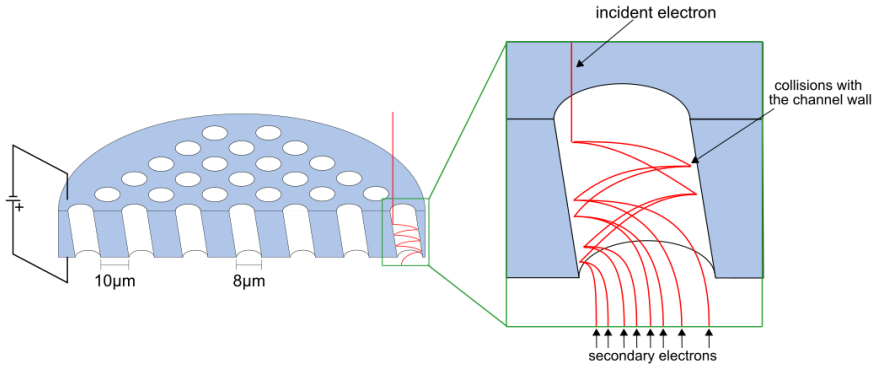

Figure 2.10: *Operation principle of a microchannel plate (MCP). An incident electron or particle hits the wall of one of the channels. The secondary electrons created are accelerated through the channel. Every time one of the electrons hits the channel walls, more secondary electrons are created. Figure adapted from [25].*

2.6.3 MagneToF Detectors

A different approach to ion detection with electron multipliers are the MagneToF detectors developed by the Australian company *ETP Ion Detect* [26]. To minimize the time spread of the electrons in the multiplier section and thus achieve narrower peaks and a higher resolution compared to MCPs, MagneToF detectors use a combination of magnetic and electrostatic fields [27]. The electron optics have unsymmetrical field shapes as shown in figure 2.11, which are optimized to obtain high time resolution and high dynamic range while keeping the spatial dimensions of the detector as small as possible.

At MIRACLS' proof-of-principle setup, a first MagneToF detector has recently been installed to test whether its performance better fits the MIRACLS requirements. This involves in

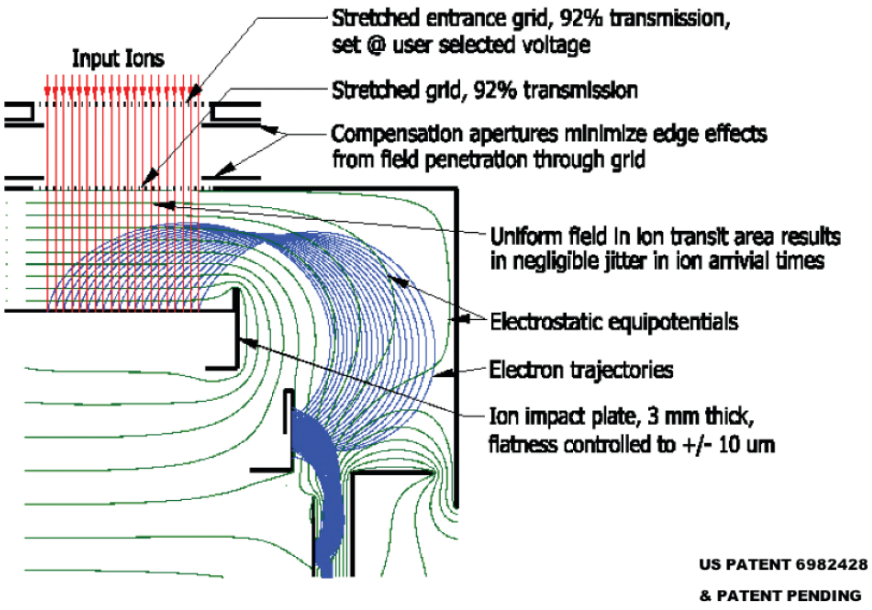

.

Figure 2.11: *Electron optics of the MagneToF detector DM167. A magnetic field perpendicular to the drawing plane forces the electrons on the curved trajectories. Figure taken from [28]*

particular whether MagneToF detectors can reliably determine the ion numbers in bunches with typically 10 000 ions in a few 100 ns.

Chapter 3

MIRACLS' Proof-of-Principle Setup

In MIRACLS' proof-of-principle setup, shown in figure 3.1, singly charged ions of stable magnesium or calcium isotopes are created in an offline ion source and injected into a Helium-filled linear Paul trap, which cools down the ions and traps them. These ions are then ejected from the Paul trap as ion bunches. The number of ions in one bunch can be controlled by changing the loading time, i.e. the interval during which the ions from the source can enter the Paul trap.

The ions leave the Paul trap at a potential of approximately 220 V and are accelerated into the first lift tube (often referred to as "lift 1"), which is initially at -2 kV at this point in time. When the ions are in the middle of the lift tube, it is quickly switched to ground, "lifting" the ions to this potential whilst preserving their kinetic energy of 2.2 keV.

The first quadrupole bender redirects the ion beam onto the beam axis of the MR-ToF device. For laser spectroscopy applications, a laser beam can be injected through the Brewster windows parallel to the ion beam in the MR-ToF apparatus.

In front of the MR-ToF device, a MagneToF detector is installed to measure the number of ions. The detector absorbs the ions it measures, therefore it is mounted on a piston so that it can be retracted and allow ions to be injected into the MR-ToF apparatus.

In the center of the MR-ToF device, the central drift tube forms a second lift (often referenced as "lift 2" or "in-trap lift"). The injection and ejection from the MR-ToF device is done with the in-trap lift technique: Initially, the central drift tube is biased to typically 700 V. When the ion bunch is in the center of the MR-ToF apparatus, the lift potential is switched to ground so that the ion bunch can no longer overcome the mirror potentials on both sides of the MR-ToF device.

The in-trap lift voltage is an important MR-ToF operation parameter, which always refers to the voltage that is applied during injection. In trapping mode, the central drift tube is at ground potential and the ions have energies between 1 keV and 1.3 keV, which corresponds to the initial energy of around 2.2 keV minus the in-trap lift voltage.

The central drift tube is made of a thin metal mesh so that fluorescence photons from the ion beam can be detected with the PMT. The space within the drift tube is on a constant potential and therefore ions will maintain the same velocity when passing the drift tube.

After ejection, the ions are guided through quadrupole bender 2 to an MCP detector which is mostly used as a diagnostics tool during MR-ToF setup and operation.

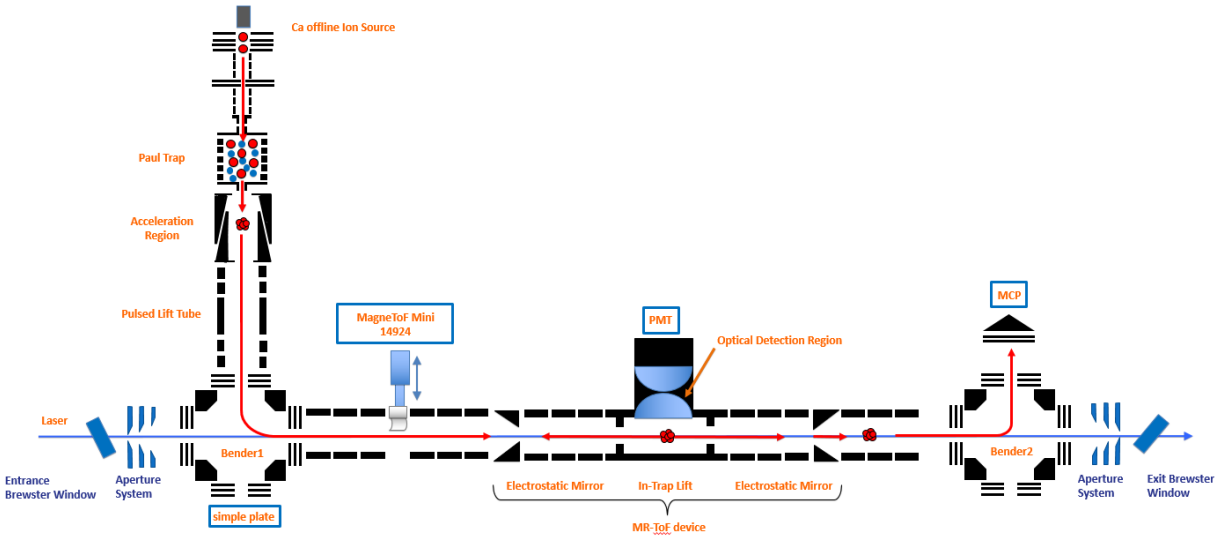

Figure 3.1: *Schematic outline of MIRACLS' proof-of-principle experiment as it was from April to June 2019. Figure adapted from [29].*

3.1 Paul Trap Operation

There are two important Paul trap operation parameters that will be used throughout this thesis:

- The **loading time** is the period of time when the Paul trap injection electrode is open and ions can enter the trap. A longer loading time means that more ions will be in the bunch ejected. Due to long term drifts in the ion source yield, the same loading times do not necessarily correspond to the same number of ions. Moreover, correlation between loading time and number of ions might not be linear in all circumstances.
- The **cooling time** is the time between ion injection (when the injection electrode closes) and release of the trap. For most applications in the PoP experiment, the cooling time is set to 15 ms. This time is needed to ensure the thermalisation of the ions in the buffer gas.

3.2 Ion Species Used in the Proof-of-Principle Experiment

Originally, the PoP experiment used singly charged magnesium ions because their stable even-even isotopes ^{24}Mg and ^{26}Mg do not have hyperfine splitting of the fine-structure levels. In this case, their D_1 and D_2 transitions shown in figure 3.2a form a closed tow-level system. This avoids optical pumping to another energy level during laser spectroscopy measurements as the excited state decays back into the initial state [21]. Hence, even-even isotopes are ideal test cases to demonstrate the MIRACLS concept.

In multi-level systems, the photon yield from laser spectroscopy can decrease over multiple revolutions if metastable states are populated, which are subsequentially no longer available for CLS at the initial spectroscopy transition. An example where this occurs is the $4p\ ^2S_{1/2} - 4p\ ^2P_{1/2}$ transition of singly charged Ca ions shown in figure 3.2b, where about 10 % of the $4p\ ^2P_{1/2}$ states decay to a third metastable level instead of back to $4p\ ^2S_{1/2}$. This problem can be solved with a second laser that re-pumps the ions from the metastable state to the $4p\ ^2P_{1/2}$ state from which they decay back into the ionic ground state $4p\ ^2S_{1/2}$. To demonstrate the re-pumping process, the previously installed magnesium ion source has been exchanged to a calcium ion source at the end of March 2019. At the end of June 2019, the calcium ion source has been changed back to the magnesium ion source.

Therefore, the measurements presented in the following chapters have been done with different ions. In each chapter, it will be indicated which setup has been used to obtain the data shown.

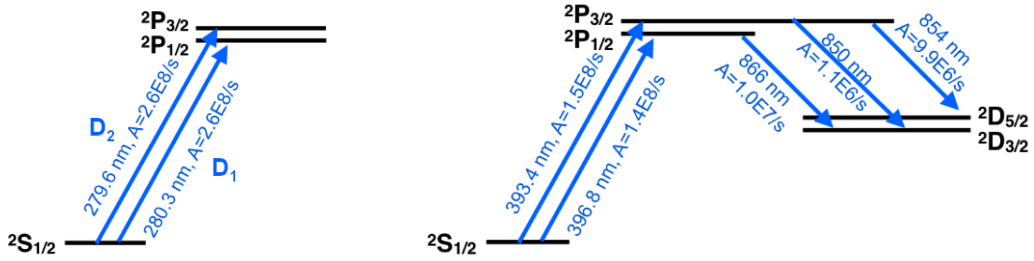

(a) Magnesium Mg^+ *(b) Calcium Ca^+*

Figure 3.2: *Relevant fine structure transitions for ions used in MIRACLS' PoP experiment. For each transition, the wavelength and the Einstein A coefficient is shown. Data taken from [30].*

3.3 Collisional Excitation

Inelastic collisions between ions and residual gas can excite higher level states which leads to the emission of fluorescence light. These collisionally induced photons are unwanted background counts in collinear laser spectroscopy. Additionally, collisions would disturb the ion motion and eventually lead to ion losses. Therefore, an excellent vacuum quality is required to avoid collisions of ions with residual gas molecules.

In MIRACLS' proof-of-principle setup, fluorescence can only be detected when the excitation happens in the center of the MR-ToF device, where the optical detection region is located. The ions spend only a fraction of the storage time in the central drift tube [31], e.g. at an in-trap lift voltage of 700 V, $^{24}Mg^+$ ions spend 720 ns in the optical detection region during a revolution period of 7.4 µs. Hence, an ion bunch with a narrow time profile of typically a few hundreds of nanoseconds can be well resolved in time inside the optical detection region. This makes collisional excitation a potential tool to investigate the ion bunch properties inside of an MR-ToF apparatus [3].

In order to enhance the collisional excitation probability such that it can be used for diagnostic purposes, a small amount of a gas (for example nitrogen) is leaked into the MR-ToF device (at around 1×10^{-7} mbar). The number of collisions in one revolution remains extremely low, to minimize losses caused by these collisions. Thus, the measurement is repeated many times

and the photon counts are added up for each time bin. The result is a photon count signal over the time of flight, as shown in figure 3.3. Since the collisional excitation is assumed to be non-resonant, different (Mg^+) ion species can be followed simultaneously. Moreover, small differences in velocity inside of an ion cloud are normally insignificant in the fluorescence yield from collisional excitation. Hence, collisional excitation could provide a more complete image of the entire ion cloud compared to laser-induced fluorescence which follows a narrow resonance condition (according to equation 2.1) and accesses only ions which radially overlap with the laser beam.

The observables of collisional excitation measurements are the parameters of each peak, like peak amplitude, peak width (FWHM) and peak area. Moreover, the revolution period of an ion bunch in the MR-ToF can be calculated from the centroid positions of the peaks. All these parameters can be obtained from fitting the signal in figure 3.3. A detailed discussion of the fit program used is given in appendix F.

For every revolution in the MR-ToF apparatus, two peaks are observed as collisional excitation happens every time the ion bunch passes the optical detection region. In laser spectroscopy on the other hand, there is only one peak per revolution, as the frequency of the laser light observed by the ions is shifted depending on the direction in which the ions are travelling (see *Doppler shift* in section 2.2.2).

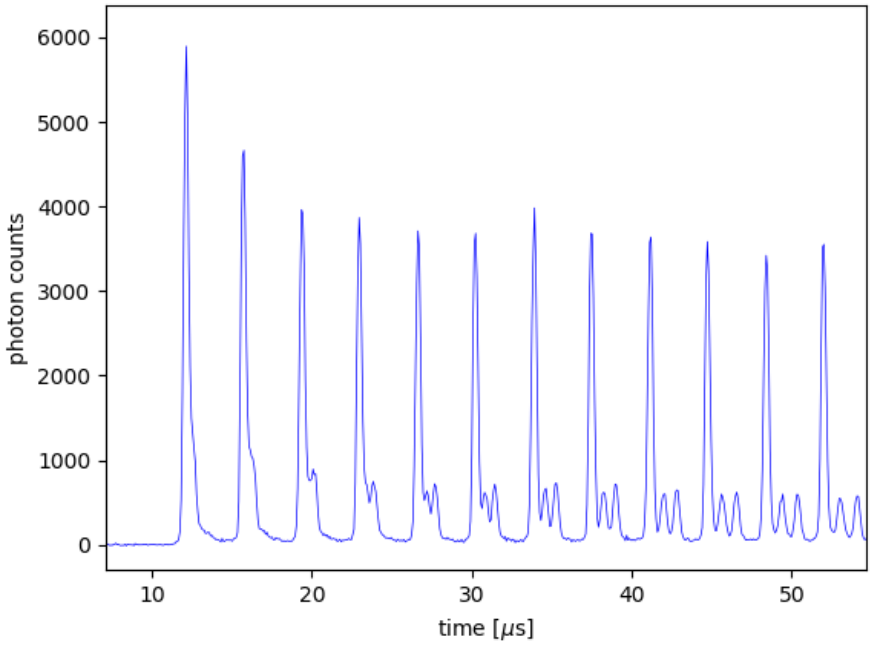

Figure 3.3: *Example of a collisional excitation measurement with magnesium Mg^+ ions. At a time around* 10 µs*, an ion bunch has been injected in the MR-ToF device. The ion bunch passes the optical detection region twice in every revolution, and every time a peak is observed. After a few revolutions, the different magnesium isotopes have been separated in time (small peaks).*

3.4 Summary of Previous Work and Open Questions

First indications of space charge effects in MIRACLS' proof-of-principle MR-ToF device have been observed during laser spectroscopy measurements. Simulations have given a first insight

into this topic and collisional excitation measurements have been conducted in March 2019. It has been shown that these measurements deliver a detailed picture of the properties of ion bunches inside an MR-ToF device [3]. However, a detailed investigation of the effects observed is yet to be done.

This section will give a short overview on what is already known about MR-ToF operation and space charge effects in MIRACLS' PoP experiment and which questions are to be answered in this thesis.

3.4.1 MR-ToF Operation

The revolution period of an ion bunch in a MR-ToF device depends on the kinetic energy of the ion bunch. MIRACLS' proof-of-principle MR-ToF device uses an in-trap lift to capture and release ion bunches. As already mentioned in chapter 2.4, the energy of the trapped ions can be controlled by varying the in-trap lift voltage.

Figure 3.4 shows a simulation of the ion bunch revolution period T for $^{24}Mg^{+}$ ions in the MR-ToF device MIRACLS' PoP experiment as a function of the ions' kinetic energy E. In this graph, there are two different areas of interest:

- In the center of the plot, the revolution period stays almost constant, i.e. $dT/dE \approx 0$. This area is called **isochronous mode**, as slight variations in the ion energy do not change the revolution time. Hence, the width of an ion bunch stays constant for many revolutions in isochronous mode.
- Realms where the revolution time strongly depends on the ion energy are called **non-isochronous mode**. This is the case for in-trap lift voltages smaller than 800 V (higher energies, $dT/dE > 0$) and for voltages higher than 940 V (lower energies, $dT/dE < 0$). In this operation mode, even a small energy spread in the ion bunch will lead to different revolution times. Therefore, the bunches which always have an initial energy spread will get broader and broader with increasing revolution number.

Many MR-ToF applications aim to operate in the isochronous mode, which is however often hard to achieve and conserve. On the other hand, in specific cases it is desirable to operate in the non-isochronous regime in order to focus the ion bunch in time onto the detector after ejection which could lead to comparably high mass resolving power [20].

3.4.2 Space Charge Effects in an MR-ToF Device

While ions typically have a few keV of energy inside the central region of an MR-ToF apparatus, their energy can go down to a few meV at the turning points in the mirrors. As the ions have a lower energy and thus stay longer in the mirror areas and as the ions are radially focused in the mirror, their density can increase by two or three orders of magnitude in comparison to the central drift tube [31]. In regions of high charge density, repulsion between charged particles can change the properties of the ion bunch. Different effects of this kind are summarized with the term **space charge**.

An important space charge effect for MR-ToF operation is **self-bunching** or **self-synchronization** [32], [33], which can occur in MR-ToF operation modes with $dT/dE >$

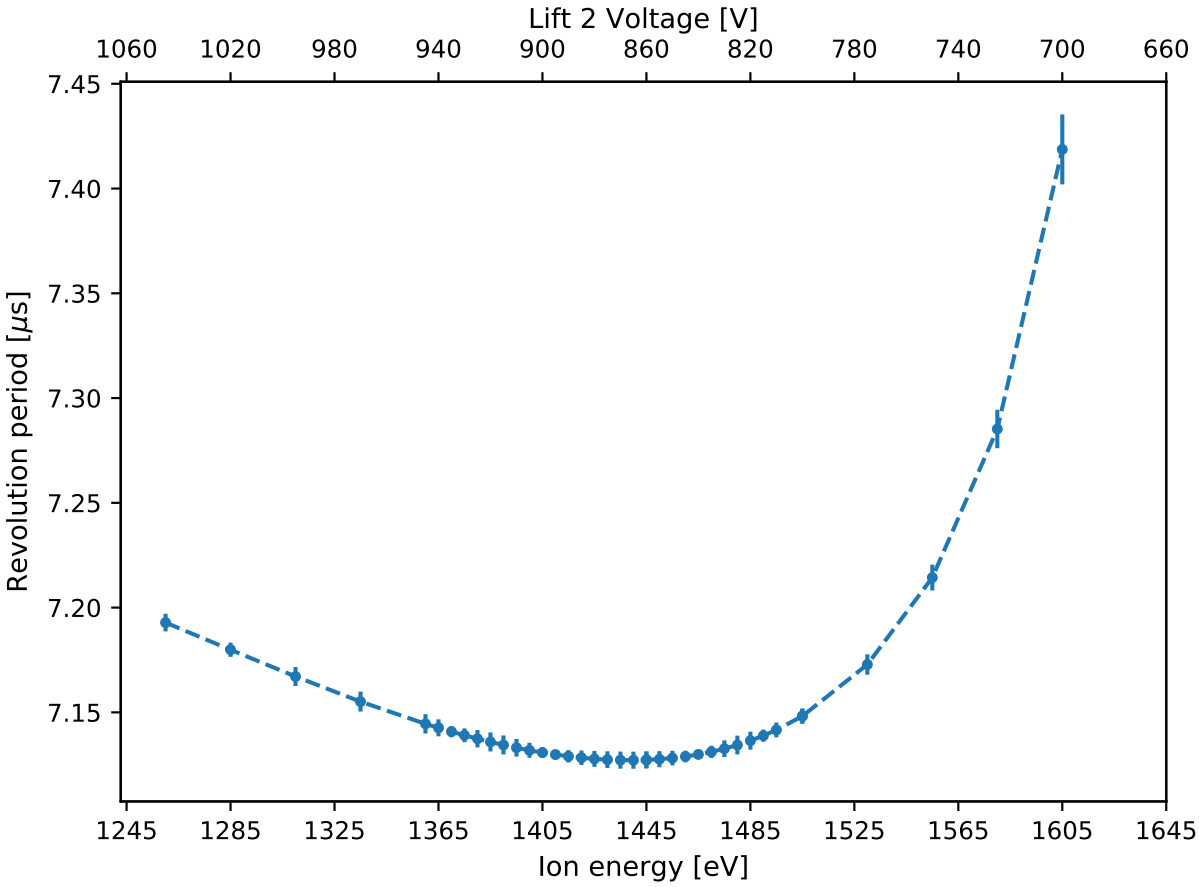

Figure 3.4: *Simulations of the revolution period of $^{24}Mg^{+}$ ions in the MR-ToF device of MIRACLS' PoP setup. Data taken from [3].*

0 [34]. In this non-isochronous region, the ion bunch would normally quickly disperse. However, for high enough ion numbers a constant bunch width has been observed. After the faster ions of an ion bunch have reached the turnaround point in the mirror and travel in the opposite direction, they encounter the slower part of the ion bunch. If the charge density is high enough, the Coulomb interaction between the faster and the slower ions decelerates the faster ions and the ion bunch stays together.

Apart from simulations for MIRACLS' PoP setup, space charge has also been observed experimentally. Figure 3.5 shows the development of bunches with different numbers of ions over multiple revolutions in the MIRACLS' MR-ToF device, measured with collisional excitation.

The data in figure 3.5 has been taken shortly before the work on this thesis was started. While it vividly illustrates space charge effects, it also points to the first problem that need to be tackled next: The different plots shown in the figure measurements are labelled with Paul trap loading times instead of the numbers of ions in one bunch. While one can qualitatively say that a higher loading time means more ions, the exact number of ions is not known. To be able to compare the collisional excitation measurements with simulations, particle detectors need to be installed and characterized to measure the ion number during a collisional excitation measurement.

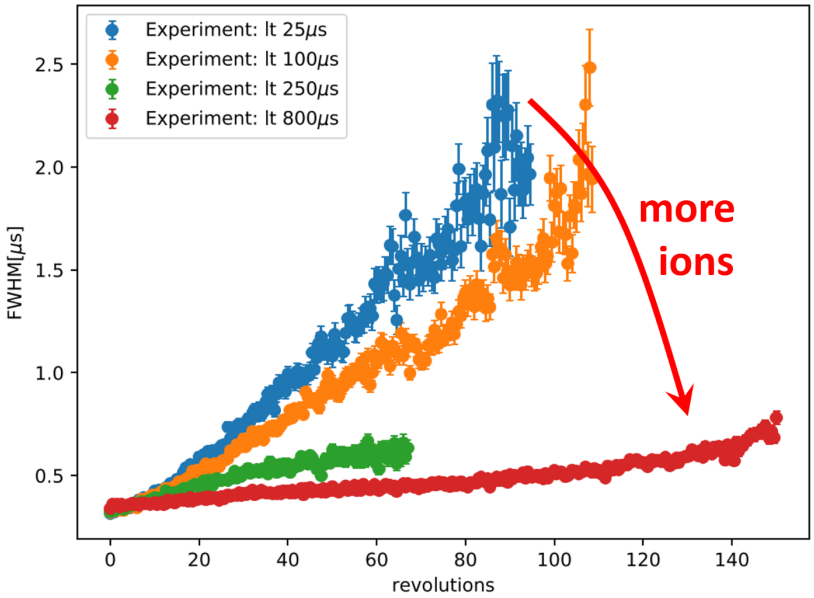

Figure 3.5: *Ion bunch width of $^{24}Mg^{+}$ ions in MIRACLS' proof-of-principle MR-ToF device over multiple revolutions and for four different Paul trap loading times (*25 µs, 100 µs, 250 µs *and* 500 µs*). This data has been taken in March 2019 using the collisional excitation technique. An in-trap lift voltage of* 700 V *has been used, so that the MR-ToF device operates in the self-bunching regime. One can see that for higher loading times (and thus increasing numbers of ions), the ion bunch width disperses less.*

Chapter 4

Characterization of MagneToF Detectors

Knowing the number of ions in MIRACLS' proof-of-principle MR-ToF device is essential for the investigation of space charge effects. MagneToF detectors, introduced in section 2.6.3, have been chosen because of their good time resolution and good linearity for a higher number of impinging particles.

As shown in figure 3.1 of the previous chapter, a MagneToF Mini 14924 detector had already been installed in 2018, located between the first quadrupole bender and the MR-ToF device of the PoP setup. It will be referenced as "first MagneToF" in the following chapter. A second MagneToF detector has been installed after the MR-ToF device during the work on this thesis. Figure 4.1 shows the positions of the two MagneToF detectors. MagneToF devices detect ions that impinge onto the impact surface in the detector. To allow ions to pass, both detectors are mounted on linear motion feedthroughs so that they can be retracted.

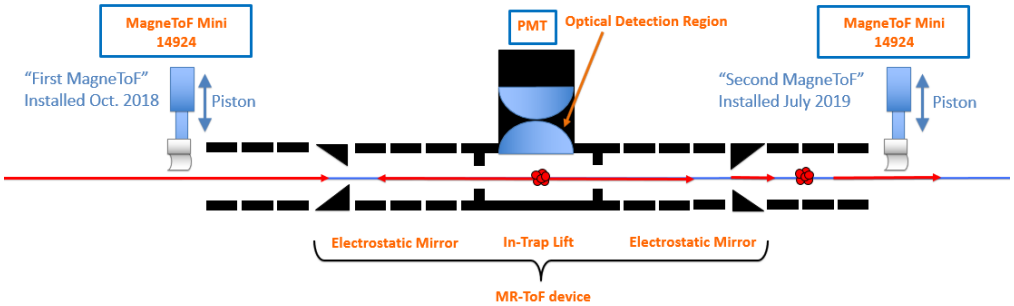

Figure 4.1: *Location of the two MagneToF detectors used for the measurements in this thesis.*

In section 4.1, the characteristics of the first MagneToF detector at low ion beam intensities are measured and it is checked whether or not the MagneToF detector complies with the information given on the data sheet. Assuming that there is a linear relation between the number of ions N impinging on the detector and the area of the detector's response signal A_{signal}, the number of ions can be calculated if the mean peak area of a single ion A_{1ion} is known. Hence, an important part of the characterization procedure will be to measure A_{1ion}.

For the investigation of space charge effects described in later chapters, the number of ions

going into, as well as the number of ions coming out of the MR-ToF device has to be measured. Section 4.2 describes how the characterization procedures found in section 4.1 are applied to both MagneTOF detectors and gives an outlook on the practical use of the MagneToF detectors for future measurements.

Section 4.3 shows how the first MagneToF detector responds to high ion intensities. The aim of this section is to check whether the detector still gives a linear response in signal area for high ion numbers typically used at MIRACLS or whether there are any saturation effects that limit its operation.

4.1 Characterization of the First MagneToF Detector with Ca^+ ions

The initial characterization measurements of the first MagneToF detector have been conducted while the calcium ion source was installed at the proof-of-principle setup (see section 3.2). The objectives were not only to analyze the response of this particular detector, but also to develop a procedure that can be applied to characterize further MagneToF detectors.

4.1.1 Finding the Correct Operation Voltage

A suitable operation voltage for a MagneToF detector can be found by selecting a threshold voltage for ion detection and count the number of ions in a certain time window for different operation voltages [35]. The result should look as seen in figure 4.2 and is often called "plateau curve" due to the flat part in the middle. The following considerations have to be taken into account:

- The gain of the detector is dependent on the operation voltage. As can be seen in region I in the plateau curve, too low operation voltages will lead to signal heights that are too small to detect.
- Too high operation voltages on the other hand will lead to accelerated aging of the detector and can cause other unwanted effects like double-counting and ion-feedback as shown in region IV.

As a compromise between detecting as many ions as possible and slow aging, the ideal operation voltage is right above the knee of the plot, between region II and III, where small variations in the operation voltage have little effect on the number of ions counted.

Operation Voltage for the First MagneToF Detector

In figure 4.3, one can see the plateau curve that was recorded with the first MagneToF detector. The Paul trap loading time was chosen so that pile-up events are negligible. This means that the ion beam intensity is so low that it is unlikely that two ions arrive at the same time and are counted as one event. For all further measurements with this detector in this thesis, an operation voltage of 2.45 kV has been chosen.

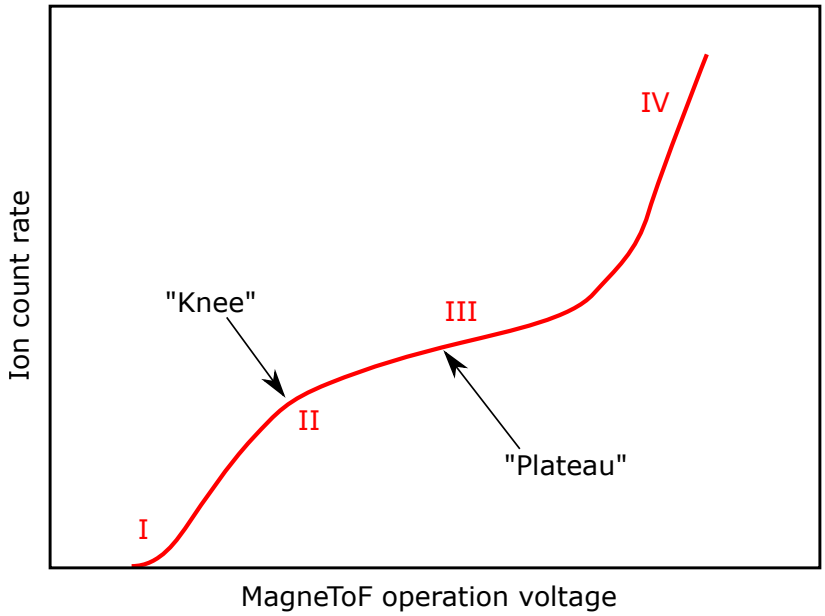

Figure 4.2: *Schematic diagram of the plateau curve that helps choosing the correct operation voltage. The operation voltage should be chosen right above the "knee" in the plot. See text for details.*

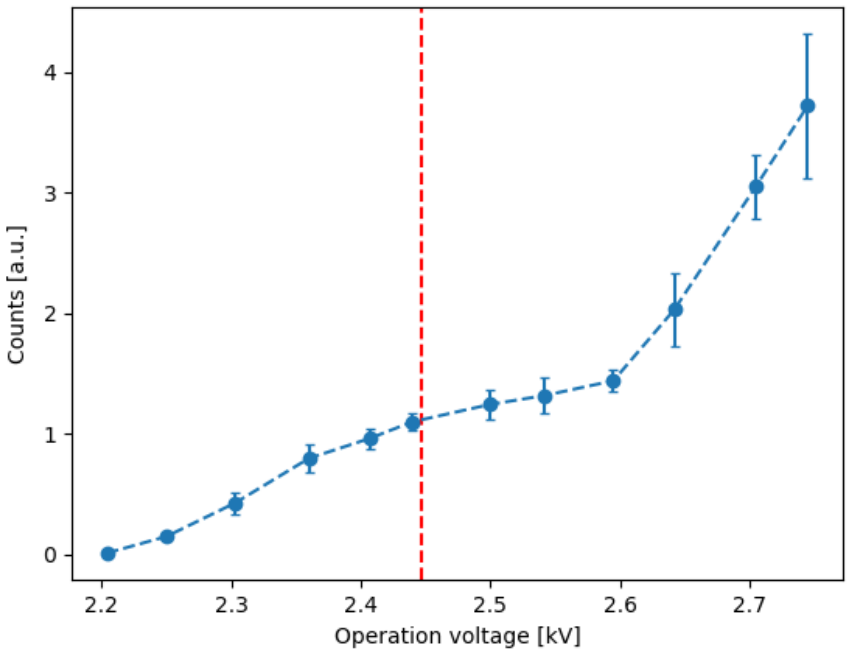

Figure 4.3: *Plateau curve of the first MagneToF with Ca^+ ions. The selected operation voltage is marked with a red line.*

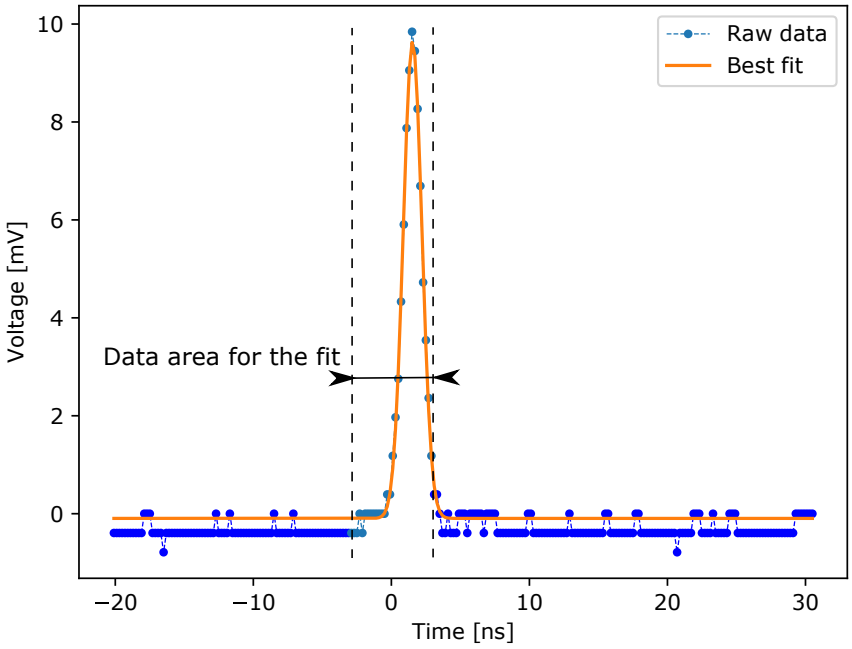

Figure 4.4: *Example of a peak from an ion measured on the first MagneToF detector. The fit of the peak is plotted in orange. The black dashed lines show the input data area for the fit. Note that the signal is shown inverted: the MagneToF detector delivers negative output voltages.*

4.1.2 Single Ion Peak Measurements

The first approach for analyzing the peak shapes of single ions measured on the MagneToF detector was to record peaks with an oscilloscope and fit the peak shape with a Gaussian. A typical peak shape with the corresponding fit can be seen in figure 4.4.

A *PicoScope 6402D* oscilloscope was used for these measurements. The procedure followed the steps below:

1. The ion beam intensity controlled with the Paul trap loading time was chosen so that at maximum one ion hits the detector during the recording time of 50 ns.
2. The oscilloscope was configured to trigger directly on the peaks produced by ions on the MagneToF detector. A trigger level of −0.6 mV was selected. A trigger voltage closer to 0 would trigger on remaining electric noise.
3. Between 2 000 and 10 000 triggers were recorded for each measurement.
4. Each recorded signal was then fitted with a Gaussian curve.
5. The extracted peak height, width and area were then used for further analysis.

For each measurement, the quality of the fits was reviewed in a visual inspection. Additionally, fits with a reduced chi square above a previously defined maximum are not used for the final analysis.

Eliminating Coupling and Noise

To ensure that only ion events are recorded and analyzed, a background measurement with no ions impinging on the MagneToF has been performed. This was achieved by closing the valve between the Paul trap and the MagneToF detector and putting the measurement and control cycle of the entire MR-ToF setup on hold.

When turning the measurement cycle back on with the valve still closed, noise originating from the HV switching of the Paul trap injection electrode and from the in-trap lift was observed. The amplitude of these noise peaks was high enough to trigger the oscilloscope and cause a record event.

To address this issue, the system cycle of the PoP setup has been changed during the single ion peak measurements:

- The in-trap lift could be switched off without influencing the measurement, as the first MagneToF detector is located before the MR-ToF device.
- The injection electrode of the Paul trap had to be switched off for the whole measurement. Therefore, the Paul trap was open all the time and the effective loading time was the overall cycle period.

Characterizing the Dark Counts and Background

With the changes described above applied to the setup, the counts caused by coupling and noise were eliminated as far as possible. To get the number of dark counts remaining and their influence on the overall measurement, the single ion peak characterization measurement has been repeated with an operation voltage of 2.45 kV.

First, 10 000 shots on the scope have been recorded as in the previous single ion peak measurements. Then, the valve in front of the MagneToF has been closed and another 10 000 shots have been recorded. All peaks detected in this second series have to be dark counts or noise as no ions form the ion source were able reach the detector during this measurement.

For both series, the count rate has been measured with a stop watch. The count rates of both series are shown in table 4.1. The dark count rate on the MagneToF detector is significantly lower than the number of ion events during the measurement.

Table 4.1: *Count rates of single ion measurements with ions hitting the MagneToF detector in series 1 and the valve closed in series 2.*

Series	**Count rate (Counts/min)**
Series 1 (ions)	80.9 ± 0.2
Series 2 (background, dark counts)	1.5 ± 0.5

In figure 4.5, the peak area distributions for both measurements is plotted. The amplitudes of the histograms have been scaled to the respective count rates. One can see that dark counts are negligible for the overall measurement result.

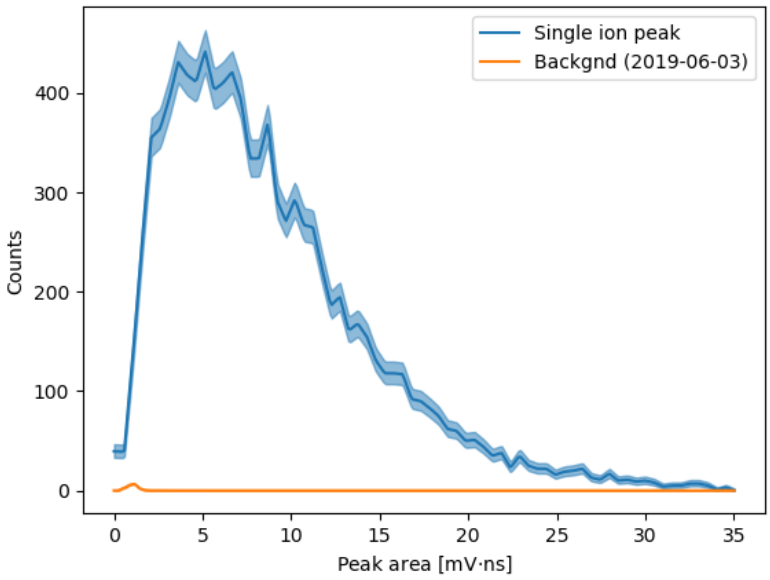

Figure 4.5: *Single ion peak measurement (triggered on the peaks) with the first MagneToF and Ca^+ ions. Both histograms are normalized to the respective count rate. The background signals consist only of dark counts.*

Findings: Peak Characteristics for Different Operation Voltages.

Measurement results for peak amplitudes (in absolute values) are shown in figure 4.6a, in which the trigger level of −0.6 mV on the oscilloscope is marked in red. This measurement has been done with different operation voltages in order to compare the previously chosen operation voltage of 2.45 kV with a lower value. One can see that with an operation voltage of 2.35 kV, the gain of the MagneToF detector would be so low that a significant amount of the signal peaks would be below the trigger threshold (red line in the plot) which is not the case for the selected operation voltage of 2.45 kV.

Figure 4.6b shows the distribution of the peak width measured on the MagneToF. According to the data sheet of the MagneToF Mini 14924 (see appendix A), the FWHM of an ion pulse should be less or equal to 1.5 ns. This is confirmed by the measurement: the weighted mean of the peak FWHMs is 1.48(1) ns.

4.1.3 Integration Over Multiple Peaks

While setting the trigger of the oscilloscope directly on the peaks from the MagneToF makes the fitting of single peaks easier as their position in the recorded signal is known, the drawback is that one can not be sure when exactly the signal was recorded in relation to the timing of the system (e.g. Paul trap release).

During the measurements, it has turned out that the dead time of the oscilloscope is larger than the ion bunch width. Therefore, the oscilloscope triggers only on the first ion of each shot. While the main ion bunch consists of $^{40}Ca^+$, the faster ions ahead of it could be the lighter $^{39}K^+$, which occurs as unavoidable impurity, or other contaminants with even lower masses. This means that the trigger events recorded in the measurements above could be

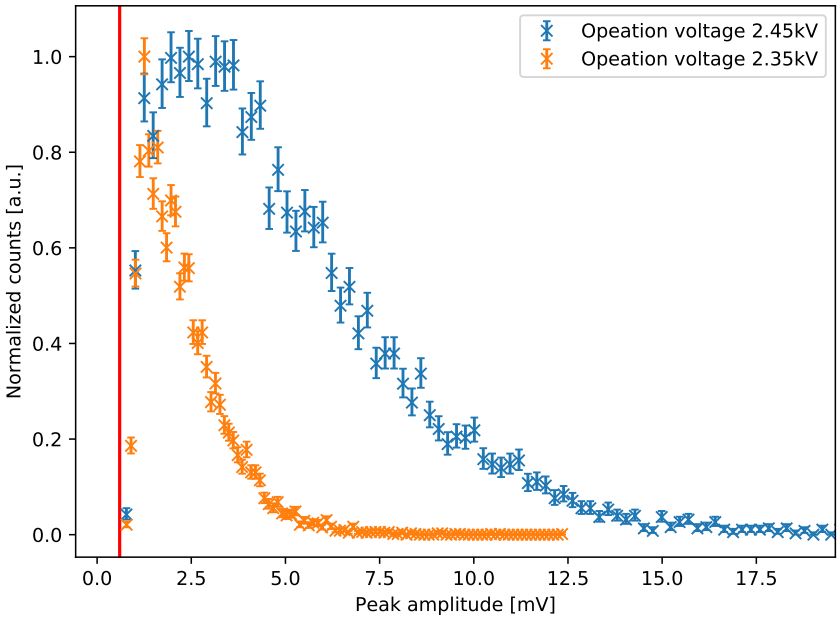

(a) Peak amplitude distribution of different operation voltages. The trigger level for detecting the peaks is marked with a red line. The histograms are normalized to 1 so that they can be easier compared.

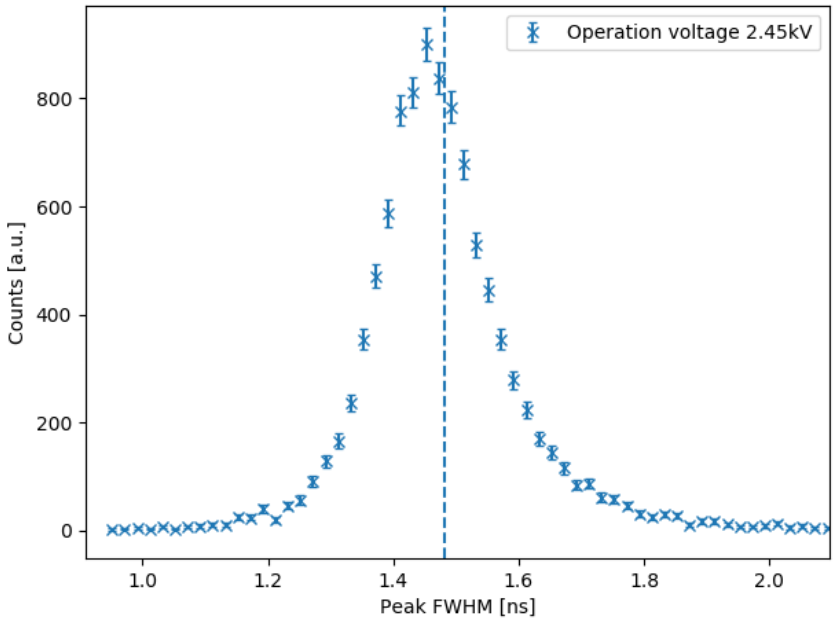

(b) Peak FWHM distribution for an operation voltage of 2.45 kV*. The weighted mean of the distribution is marked with a dashed line.*

Figure 4.6: *Distribution of amplitude and FWHM of single ion peaks measured on the first MagneToF with calcium Ca^+ ions at* 2 keV*.*

ions lighter than calcium. To validate the results achieved so far, a different measurement method is required.

An alternative method of determining the peak area per ion is to trigger on the Paul trap ejection and add a delay to the trigger so that a signal is recorded at the time when the ions of interest arrive at the MagneToF detector. Below, this measurement method will be referenced as "signal integration method" or "peak integration method".

An advantage of the signal integration method is that because the timing relative to the Paul trap is known, the switching of the in-trap lift and the Paul trap injection do not have to be disabled to suppress noise occurring at other cycle times. Moreover, ion species with other mass numbers can be excluded via time-of-flight. The disadvantage is that the temporal position of the ion peaks in the recorded signal varies from ion to ion due to the ions' spread in energy and initial position when extracted from the Paul trap.

This measurement is conducted and analyzed in the following way:

1. record a MagneToF signal triggered by the Paul trap ejection signal,
2. numerically integrate over the entire signal trace,
3. count the number of peaks in the recorded signal trace and
4. divide the total area from step 2 by the number of peaks. This gives the mean peak area for one ion.

The procedure is repeated multiple times for different loading times. The number of peaks is counted using a threshold of $-0.6\,\mathrm{mV}$, the same as the trigger level of the oscilloscope in the previous section, but the difference is that here the threshold is applied by an evaluation software after the measurement. Figure 4.7 shows an example of how the peaks are counted.

Signal Pile-Up

While increasing the ion rate in signal integration measurements increases the sampling rate, it also increases the risk of pile-up, i.e. the risk of two peaks being interpreted as a single one. Figure 4.8 illustrates this situation: The evaluation software that calculates the number of ions essentially counts the peaks and can therefore handle slight overlaps in time. However, if the two ion events occur so close together that they produce a single peak, they are interpreted as one ion event.

During the present work, it has been found that for a time range of 500 ns on the oscilloscope (like in the example shown in figure 4.7) and up to 10 peaks per trigger event, pile-up is negligible.A good visualization of pile-up can be achieved by plotting the integrated signal area from step (2) versus the number of peaks in the signal in step (3), as shown in figure 4.9. One can clearly observe that measurements with lower loading times follow a linear trend, while the measurements with loading times above 100 µs deviate from this behaviour (indicated with a dashed line). For higher loading times, the number of identified peaks is less than the actual number of ions due to pile-up effects and therefore these data points are shifted leftwards which makes the graph appear bend upwards in the plot.

Figure 4.9 is already a first indication that the output signal area of the MagneToF detector

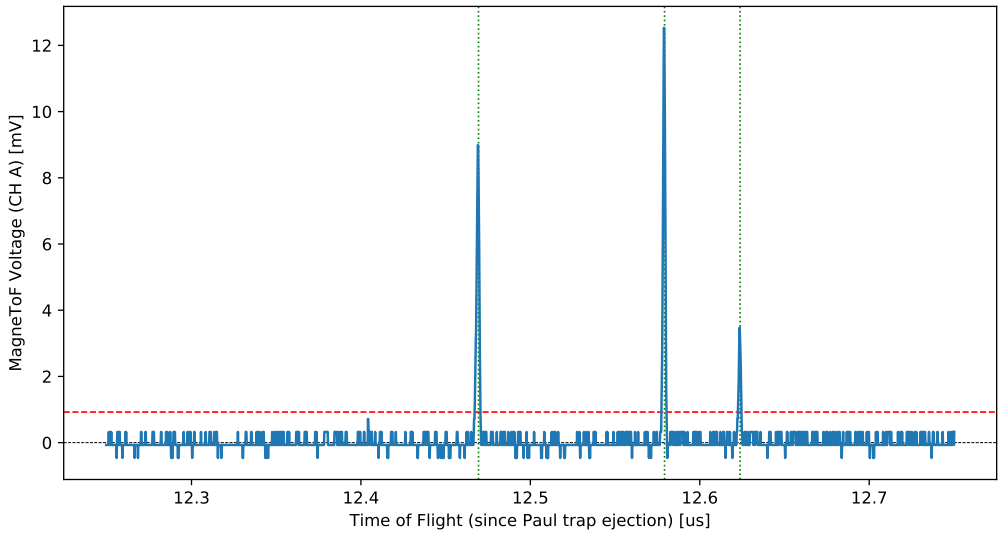

Figure 4.7: *Example of a MagneToF signal recorded with a Paul trap loading time of* 30 µs*. Please note that the y-axis has been inverted. The red dashed line is the threshold to count the number of peaks (which is also the number of ions). The threshold voltage is* 0.6 mV*, but it appears to be higher in the plot because the baseline of the signal has been shifted so that the fluctuations between the peaks do not contribute to the integrated total signal area. The green dashed lines mark all identified peaks each representing individual ion hits.*

follows a linear law with $A_{signal} = N \cdot A_{1ion}$, however, the pile-up effects in this plot make it difficult to draw a final conclusion.

Comparison with Single Ion Peak Measurements

An important outcome of the single ion peak measurements is the distribution of the peak area of single ion events shown in figure 4.5. This distribution is also shown in figure 4.10a, along with distributions obtained with the signal integration method described above. As one can see, the results from these two different methods agree within error bars.

For the signal integration measurements in figure 4.10a, only small loading times resulting in less than two ion peaks per trigger event measured on average on the detector have been used.

Figure 4.10b shows what happens if there are multiple peaks in each trigger event: As there is a higher rate of samples, the distribution gets narrower due to the central limit theorem. A detailed investigation in appendix B.1 shows that measuring multiple peaks in one trigger event is an efficient way to increase the sample size and thus gain better statistics. Results with this increased ion rates are still consistent with single ion peak measurements and with signal integration measurements at less than one ion per shot.

The average number of peaks per trigger event is not equal to the number of ions per shot, as only trigger events with at least one ion are included in the analysis. Hence, especially for small loading times, the number of ions per shot is lower than the average number of peaks per trigger event.

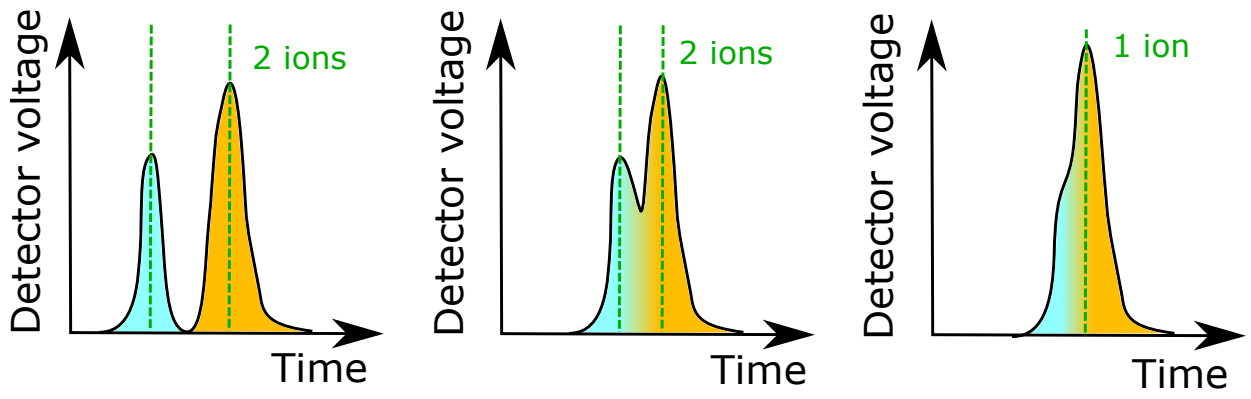

Figure 4.8: *Illustration of pile-up of two ion events on the MagneToF detector. Left: Peaks are next to each other and correctly identified as two separate events. Middle: Peaks are closer together and partially overlap in time, but can still be distinguished. Right: Peaks overlap and are incorrectly interpreted as a single ion hit by the analysis software.*

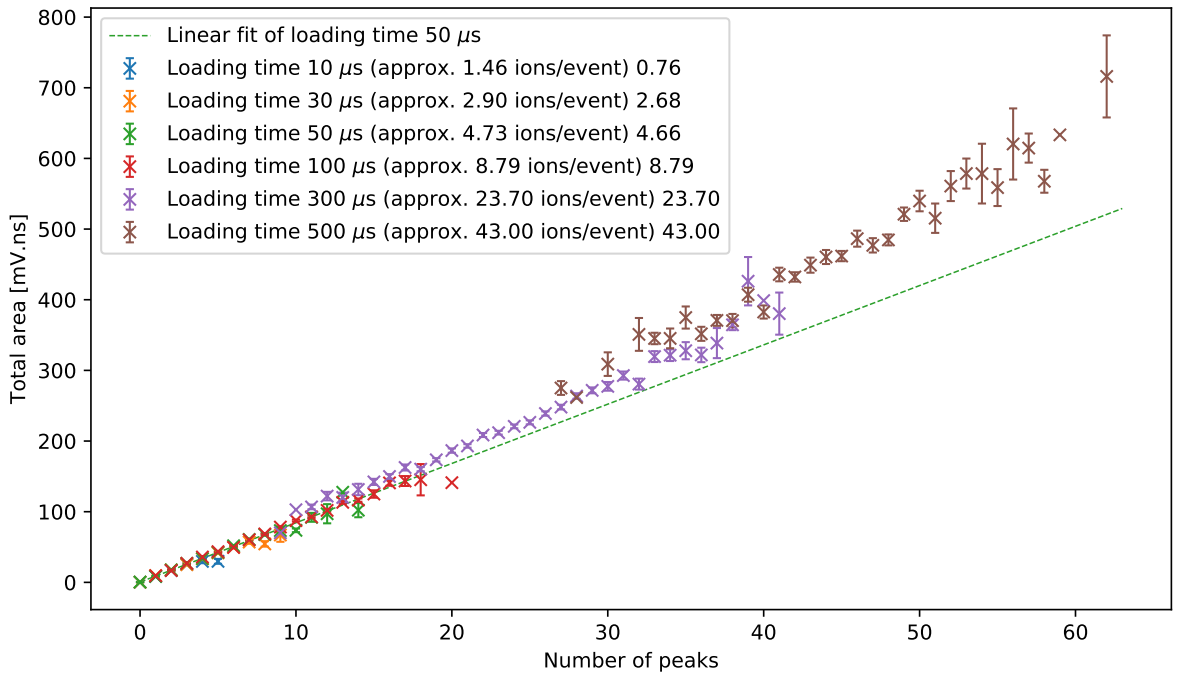

Figure 4.9: *Plot of the total signal area from different signal integration measurements versus the number of peaks counted in the respective measurement. Each color represents one Paul trap loading time. The green dashed line is a linear fit of the measurement with a loading time of* 50 µs.

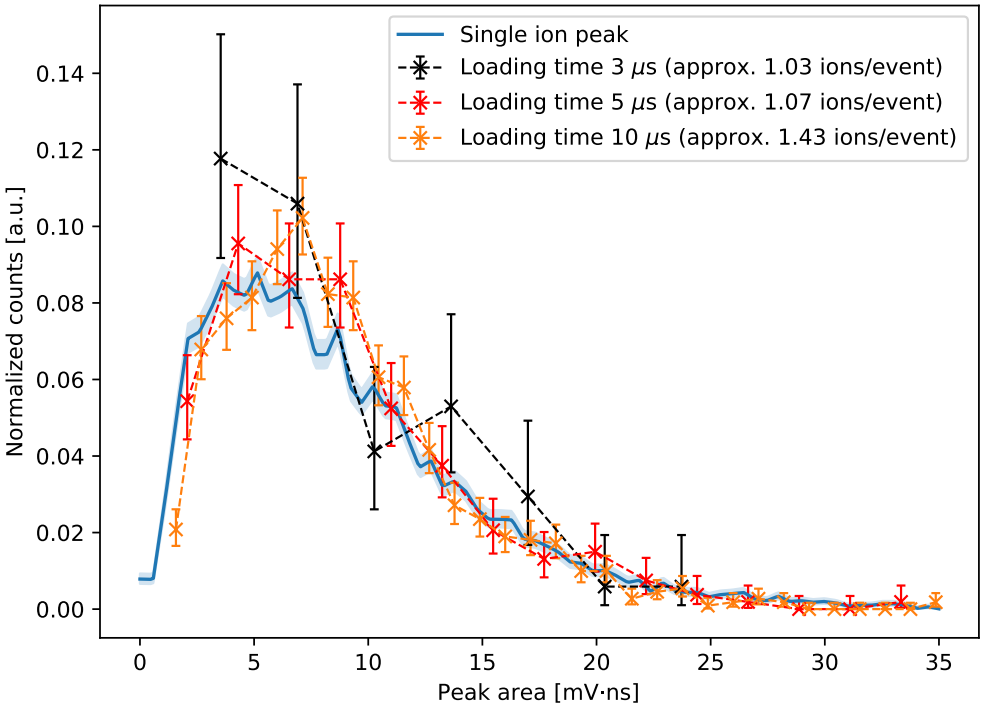

(a) Less than 2 ions per trigger event

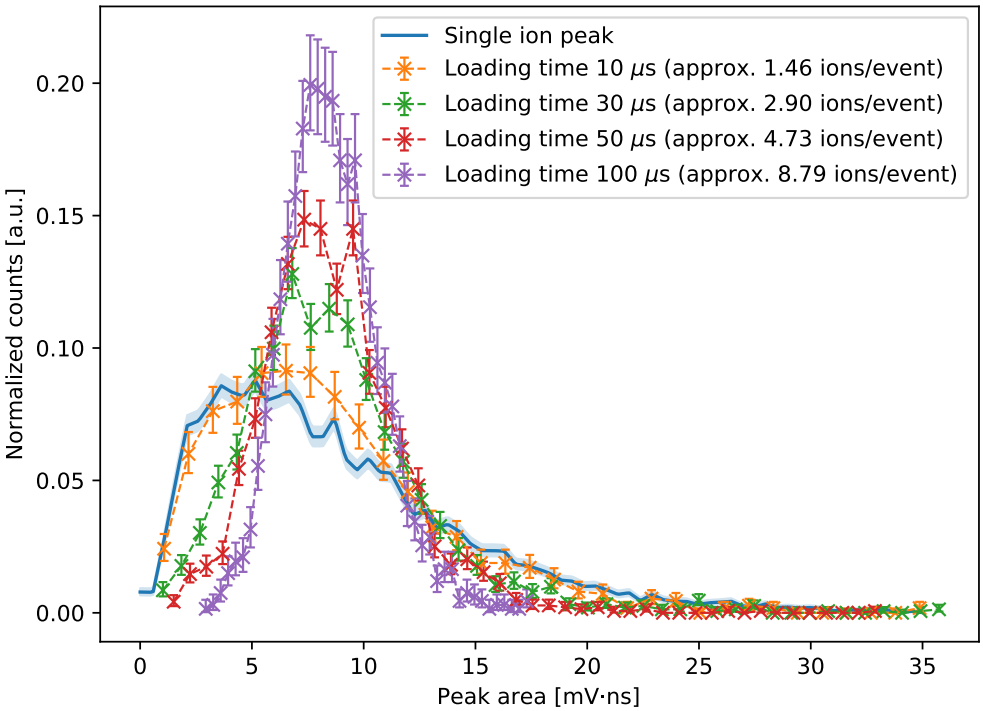

(b) More than 2 ions per trigger event

Figure 4.10: *Peak area distribution for single ions obtained with the peak integration method compared to the distribution obtained with single ion peak measurements (blue plot). The plots are normalized to an area of 1. The number of ions per trigger event is not the average number of ions per shot from the Paul trap. Details see text.*

4.1.4 Comparison of Characterization Methods

To measure the mean area of a single ion response on the MagneToF, two different methods have been used. The section shows that both approaches deliver consistent results. During the measurement and evaluation process, advantages (+) and disadvantages (-) of both methods became apparent:

Single Ion Peak Measurements
Described in section 4.1.2

+ Investigation of peak shape, all peak properties (FWHM, area, amplitude)

− Not sure which ion species are recorded

Signal Integration Method
Described in section 4.1.3

+ Multiple samples acquired in each shot and therefore higher statistics

+ Trigger set to Paul trap

− No information about peak shape

4.1.5 Measuring the Mean Peak Area for one Ion

The essential task in this chapter is to determine the mean area produced by a single ion event on the MagneToF detector. Using the signal integration method for different loading times, different mean peak areas have been found, as shown in figure 4.11. Data points with loading times higher than 100 µs or more than 10 ions per shot are distorted by pile-up events (see previous discussion and figure 4.9). Therefore, their mean peak area is higher (because $A_{1ion} = A_{signal}/N$ and N is estimated too small). Hence, the overall mean peak area for one $^{40}Ca^{+}$ ion can be calculated as the weighted average of the first four points in figure 4.11, where pile-up has been found (in figure 4.9) to be negligible.

$$A_{1ion} = 8.60 \pm 0.04 \text{ mV} \cdot \text{ns}$$

4.2 Characterization Procedures applied to Mg^{+} ions

With the characterization of the first MagneToF detector, a characterization procedure has been developed and it has been shown that the detector's characteristics meet the requirements of MIRACLS. Therefore, the second MagneToF detector has been installed downstream of the MR-ToF apparatus.

At the same time, the offline ion source of MIRACLS' proof-of-principle experiment has been changed from Ca^{+} to Mg^{+} ions. Therefore, *both* detectors have been characterized again.

4.2.1 Characterization procedure

Simplifying the working steps of the previous section, the characterization of a MagneToF detector requires two tasks:

1. Find a suitable operation voltage as described in section 4.1.1.

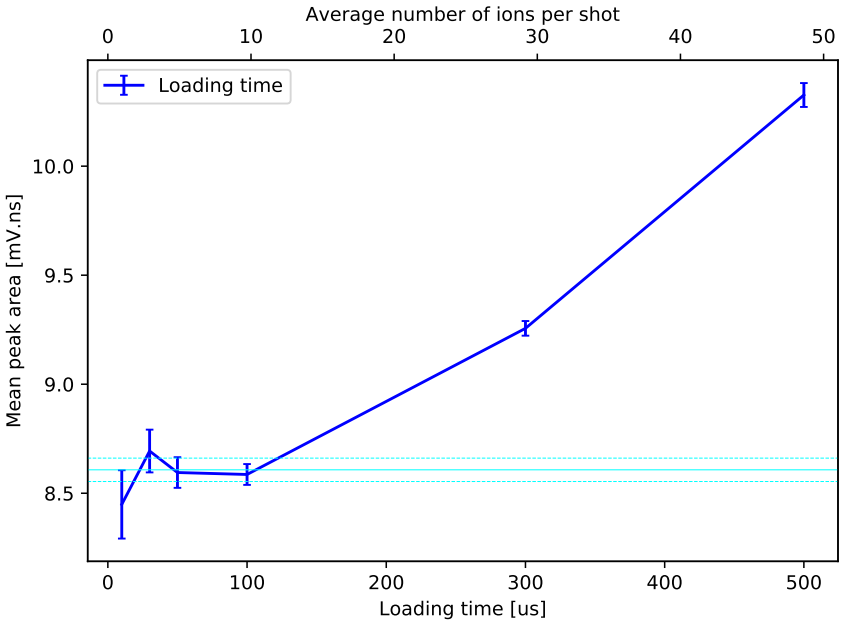

Figure 4.11: *Mean peak area per ion measured with the signal integration method for different loading times. The light blue solid and dashed lines show the weighted average of the first four data points with a loading time of* $\leq 100\mu s$*. The upper x axis shows the average ion number per shot from the Paul trap. The conversation factor between ion number and loading time is specific to this measurement and can not be applied to other measurement results.*

2. Measure the mean peak area per ion A_{1ion} using the signal integration method described in chapter 4.1.3.

A detailed step-by-step procedure can be found in appendix C.1.

4.2.2 Re-Characterization of the First MagneToF with Mg$^+$ ions

Utilizing the same operation voltage of 2.45 kV as previously with the Ca$^+$ ions, the first MagneToF detector has been characterized once more with Mg$^+$ ions. The mean peak area per ion is

$$A_{ion} = 8.80 \pm 0.04 \text{ mV} \cdot \text{ns}$$

Although this value is similar to the single ion peak area of $A_{ion,Ca} = 8.60 \pm 0.04$ mV $\cdot$ ns extracted for Ca$^+$ ions, there is a difference larger than the error bars, suggesting that there might be a small mass dependence on the peak area.

4.2.3 Characterization of the Second MagneToF with Mg$^+$ ions

The second MagneToF detector after the MR-ToF device has not been used before. Therefore, the first step has been to find the right operation voltage as described in section 4.1.1. The result of this plateau curve measurement is shown in figure 4.12. An operation voltage of 2.1 kV has been chosen for all further measurements with this detector.

The selected operation voltage is lower than the operation voltage of the first MagneToF. This could be due to aging effects, as the first MagneToF has already been operating for more than half a year, or simply due to differences in the gain between individual detectors. In the future, it will be necessary to investigate aging effects of the MagneToF detector and to find out how often the characterization procedure has to be repeated. The time available for this thesis was however too short to study long-term effects.

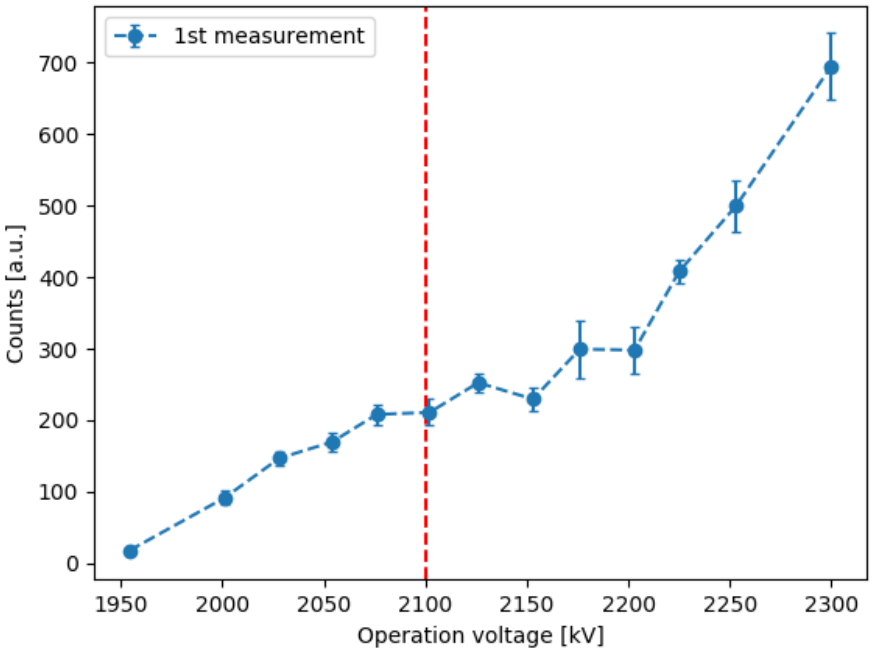

Figure 4.12: *Plateau curve measurement to find the best operation voltage for the second MagneToF detector installed downstream of the MR-ToF apparatus. The selected operation voltage is marked with a red line.*

For the selected operation voltage of 2.1 kV, the mean peak area per ion is

$$A_{ion} = 7.88 \pm 0.05 \text{ mV} \cdot \text{ns}$$

4.2.4 Detector Efficiency

A measurement procedure and evaluation software has been created to determine the number of ions with the MagneToF detector. This procedure can be found in appendix C.2.

After calculating the number of ions, a correction has to be applied: The MagneToF Mini 14924 has a detection efficiency of 92 % (see the data sheet in appendix A), which means that 92 % of the ions hitting the detector contribute to the output signal and 8 % get lost in the input grid of the detector. Therefore, ion number $N_{detected}$ calculated from the signal area has to be corrected using

$$N_{real} = \frac{N_{detected}}{0.92} \tag{4.1}$$

4.3 Linearity of the First MagneToF

For the purpose of CLS and space-charge studies in MIRACLS' proof-of-principle experiment, it is required to extend the characterization of the MagneToF detector from the regime of a few ions per time (i.e. a Paul trap loading time of a few microseconds) as done in the previous section to hundreds or even thousands of ions in an ion bunch (several milliseconds of Paul trap loading).

Figure 4.13 illustrates that for many ions inside the ion bunch, due to pile-up it is impossible to estimate the number of ions by counting individual peaks. Provided that each ion contributes the same charge, the integrated total signal area should follow $A_{signal} = N \cdot A_{1ion}$, where N is the number of ions in the bunch. However, in order to reliably determine N this way, it is necessary to know up to which order in ion number per ion bunch the MagneToF's integrated signal follows this linear scaling law. Beyond this point, the MagneToF detector may show saturation effects which would destroy the simple linear relation between ion number and integrated signal area.

4.3.1 Working Principle of the Linearity Measurements

The area of the MagneToF signal is measured for different Paul trap loading times with ion numbers far beyond the single ion regime. The recorded spectra look similar to the one shown in figure 4.13. Please note that the time scale on the x axis is different to previous example signals shown in section 4.1.

As the rate of ions injected into the Paul trap is fairly constant over a measurement period, the number of ions in the bunch should be proportional to the Paul trap loading time as long as ion losses in the Paul trap are negligible and its space charge limit is not reached. Hence, if the signal area increases linearly with the loading time, this implies that the MagneToF detector behaves linearly for this number of ions.

The measurements are conducted with $^{40}Ca^{+}$ ions at about 2 keV and a MagneToF operation voltage of 2.45 kV. The Helium pressure in the Paul trap is always kept fixed between 4.5×10^{-6} mbar and 5×10^{-6} mbar in order to ensure constant capture and trapping conditions.

4.3.2 First Loading Time Scans

On 21st May and 23rd May, the area of the MagneToF signal has been measured for different loading times up to 90 ms, with a cooling time of 15 ms. The result can be seen in figure 4.14. Although the settings have not been changed, the peak areas were different in both measurements, which is attributed to long term drifts in the ion source yield.

In both loading time scans, there is a kink in the graph at a loading time of about 30 ms. The next step is to investigate whether this kink comes from non-linearities of the MagneToF detector or from another component in the setup, such as losses in the Paul trap.

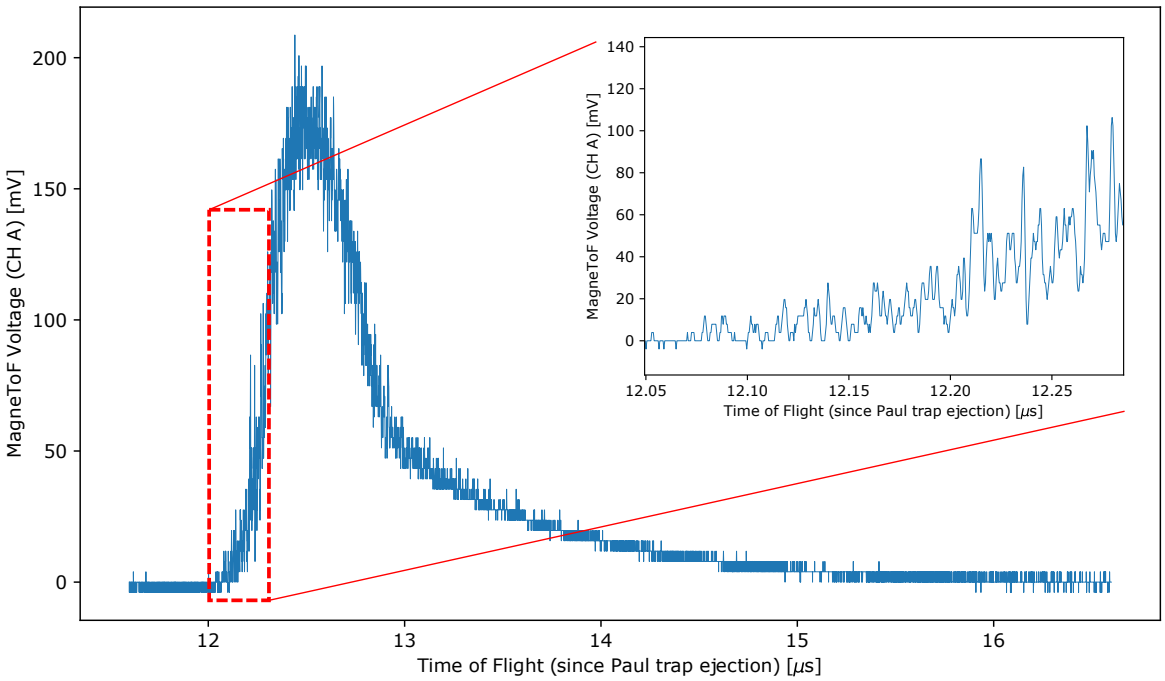

Figure 4.13: *Typical signal recorded during a MagneToF linearity measurement. The inset on the top right corner shows how single ion peaks at the beginning of the ion bunch are starting to pile up. Hence, the number of ions is far too high for single ion counting. This signal has been measured with a Paul trap loading time of* 110 ms. *Note that the y axis has been inverted.*

4.3.3 Cooling Time Scan

Previous work in [36] found that the Paul trap losses in MIRACLS' PoP setup can become important when ions are stored in the Paul trap for more than approximately 5 ms. For longer loading times, ions that arrive earlier in the trap have a longer effective trapping time (which is the time the ions spend in the trap before being released) and therefore they have a higher probability of getting lost. This could lead to the kink in the first loading time scan shown in 4.14.

As the Paul trap's RF field has been optimized after the work done in [36], it is here studied again how ions react to different times they stay in the trap. To this end, the signal area on the MagneToF detector has been measured for different cooling times while keeping the loading time constant. On 21st May, right after doing the loading time scan, different cooling times up to 110 ms have been scanned using a loading time of 1 ms.

For the Paul trap pressure used during these measurements, the number of ions extracted from the Paul trap does not change for different cooling times in the range of 100ms, as one can see in figure 4.15. The maximal effective trapping time in the loading time scans of figure 4.14 is 115 ms, which is the sum of the maximum loading time of 100 ms and the cooling time of 15 ms. This means that the cooling time scan (up to a cooling time of 110 ms) covers the effective trapping time of the loading time scans. Assuming that these results are independent of the actual ion number, it follows that losses in the Paul trap due to differences in storage time are not significant enough to influence the loading time scans. These trap losses are not the reason for the kink observed in the loading time scans.

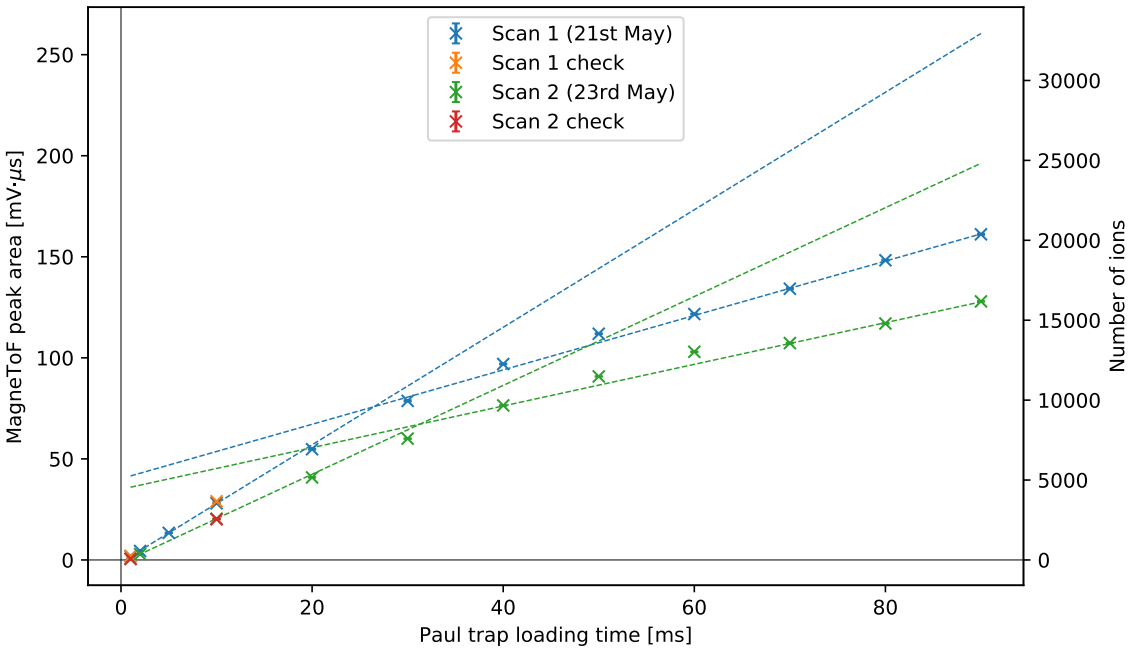

Figure 4.14: *First loading time scan on the MagneToF. The data points labeled "check" have been recorded at the end of the measurement to be able to exclude system drifts over the course of a measurement period. The dashed lines are linear fits of the first and last three points for each measurement series.*

4.3.4 Steer the Ion Beam

A further approach to investigate the kink observed in figure 4.14 is to steer the ion beam at different parts of the setup. Steering means that the beam is deflected away from its ideal direction, decreasing its intensity. This however implies additional difficulties and it was not possible to gain meaningful results in the short time available. The procedure and intermediate results are shown in appendix B.2.

4.3.5 Conclusion

The response of the MagneToF detector in terms of signal area has been studied for increasing numbers of Ca^+ ions in an ion bunch. A strictly linear trend is observed up to an integrated signal area of approximately $70\,\mathrm{mV}\cdot\mu\mathrm{s}$. This establishes a linear relationship $A_{signal} = N \cdot A_{1ion}$ to hold up to around 10 000 ions inside of an ion bunch. Beyond $N > 10000$, non-linearities between the detector's signal area and the Paul trap loading time have been observed in the present study. It has been shown that these losses are not related to the ion storage time in the Paul trap, as it was the case in a previous study.

One should keep in mind that with the means available for the measurements above, it has not been possible to see any non-linear effects that are definitely related to the detector. Thus, the linear response in signal area as a function of ion number may extend much beyond $N \approx 10000$. Future work will be dedicated to investigate this.

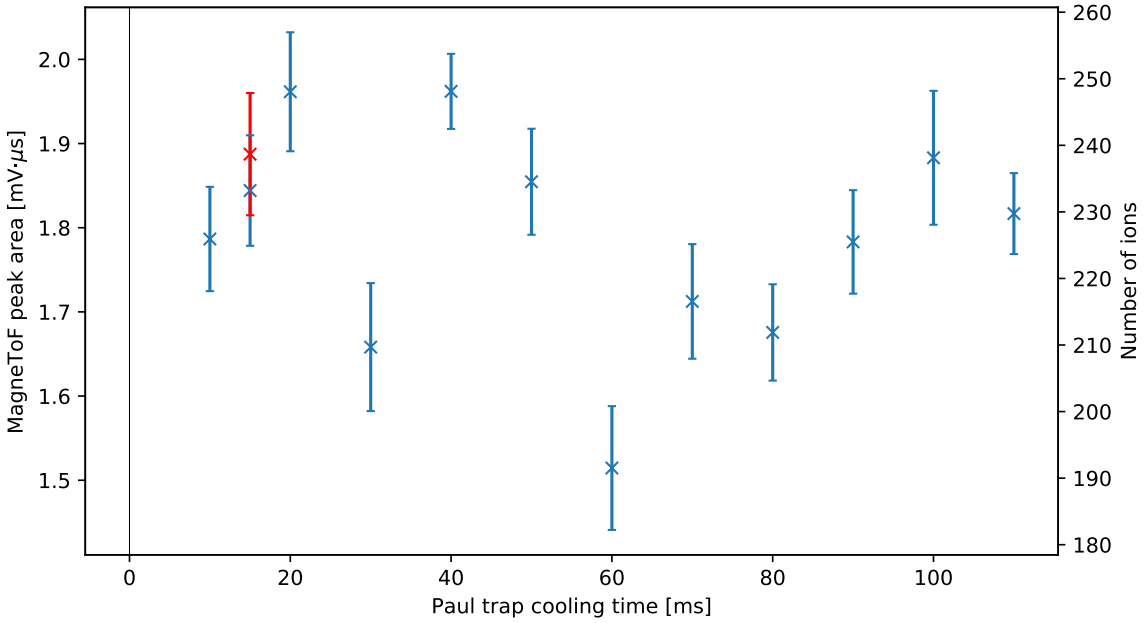

Figure 4.15: *Ion counting on the MagneToF for cooling times up to* 110 ms. *The red data point has been recorded as reference at the end of the measurement to exclude potential system drifts.*

Chapter 5

Simulation of Fluorescence Light Detection in the MR-ToF Device

Simulations of the ion trajectories in the MR-ToF device have proven to be an essential tool for research and development for MIRACLS' experimental setups. However, as far as fluorescence detection (e.g. through collisional excitation, see section 3.3) is concerned, it is currently not possible to directly compare experiment and simulation in terms of temporal ion bunch length. While the output of the simulation is a list of ion positions in the MR-ToF apparatus, the experiment folds ion position and ion bunch size with the spatial response of the optical detection region. Thus, to obtain simulation results for quantitative comparison, the optical detection of fluorescent light has to be included in the simulation process.

This extension of the simulation has been developed as part of this thesis. The enhanced simulation procedure is schematically depicted in figure 5.1. SIMION delivers the positions, time of flight and velocities of the individual ions in the optical detection region inside of the MR-ToF device. Knowing the detection efficiency at the positions along the ions' passage through the optical detection region (ODR), the temporal response of the ODR to the fluorescence emitting ion bunch can be calculated.

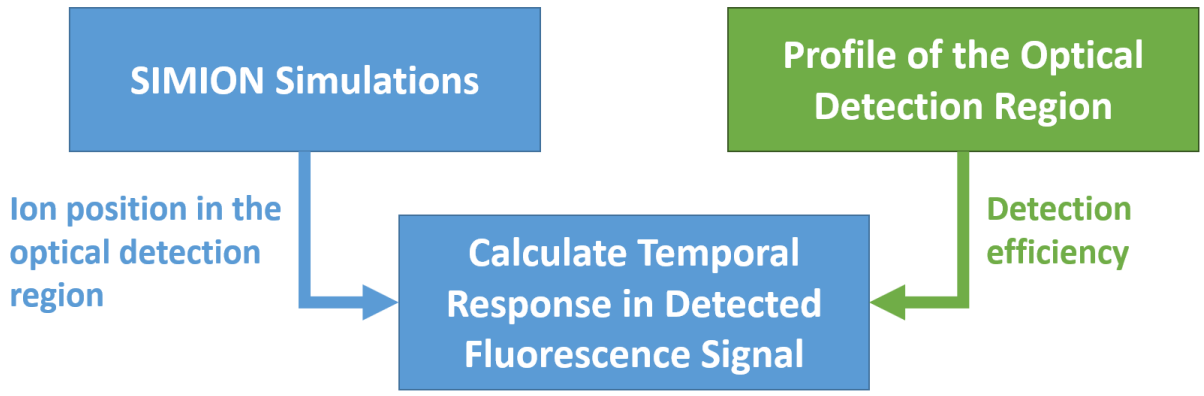

Figure 5.1: *Enhanced simulation procedure to calculate the response of the optical detection region to a fluorescent light emitting ion bunch.*

5.1 Simulations of Photon Traces in the ODR

The optical detection region (ODR) in MIRACLS' PoP experiment (adapted from [37]) consists of two lenses working as focusing optics and a PMT as detector. To reduce background originating from scattered laser light in the setup, there is an aperture with a small slit directly in front of the PMT. The distance between PMT and the lenses can be varied so that light of different wavelengths, having different refractive indices in the lenses, can be focused to pass the slit. Due to the mechanical design of MIRACLS' PoP setup, the minimal distance between lens 2 and PMT is 81.8 mm.

To calculate the optimal distance between PMT and focusing optics in the COLLAPS setup (another laser spectroscopy experiment at ISOLDE), a simulation program had been written by Wouter Gins during his PhD (for its documentation see appendix E.3). As the optical detection regions in MIRACLS' proof-of-principle setup and COLLAPS' setup have very similar dimensions and use the same components, the program could be modified and repurposed for MIRACLS. Figure 5.2 shows the relevant dimensions of the optical detection region.

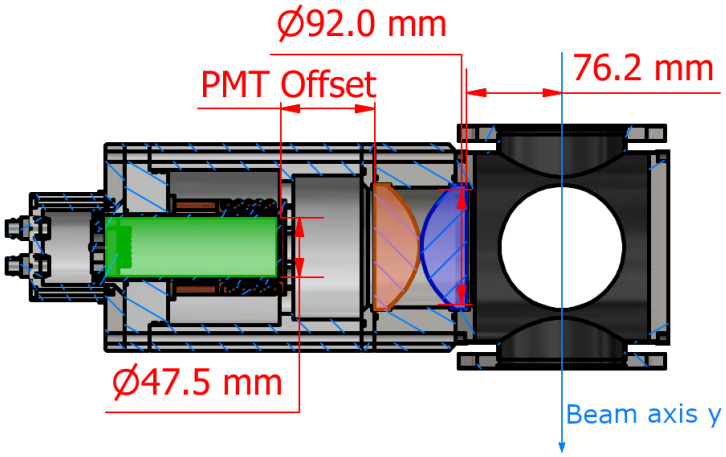

Figure 5.2: *Relevant dimensions of the optical detection region in the COLLAPS setup, which has the same dimensions as MIRACLS' PoP setup. The highlighted components are lens 1 (blue), lens 2 (orange) and the PMT (green). The only difference is that in MIRACLS' PoP setup, the minimal distance between lens 2 and PMT is* 81.8 mm. *Figure adapted from appendix E.3.*

The ODR simulation program generates photons on the ion beam axis and tracks their path through the focusing optics to the PMT. This process is called **ray tracing** and is illustrated in figure 5.3.

5.1.1 Position Dependent Detection Efficiency of the Optical Detection Region

The optical transitions in magnesium Mg^+ ions observed in the MIRACLS proof-of-principle experiment are at wavelengths around 280 nm. The detection efficiency profile of the optical detection region has therefore been calculated for this wavelength and the distance between lens and PMT has been set to the minimum of 81.8 mm so that fluorescence light with a wavelength of 280 nm is focused on the PMT.

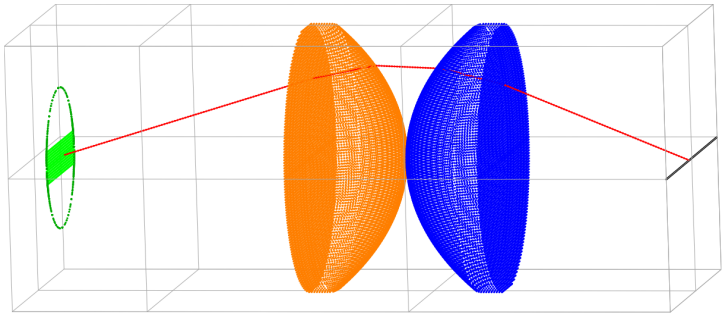

Figure 5.3: *Working principle of the ray tracer. A photon (red line) is generated on the ion beam axis (black) and propagated through lens 1 (blue) and lens 2 (orange) towards the PMT (green). Figure adapted from [38].*

The axial **profile of the optical detection region** is here defined as the detection efficiency for different positions on the ion beam axis. As the optical detection region is symmetric in respect to the central transverse plane, it is sufficient to generate photons only in one half of the ODR. The detection efficiency ϵ_{det} is the ratio between photons reaching the PMT and photons generated on the beam axis.

$$\epsilon_{det} = \frac{N_{PMT}}{N_0} \tag{5.1}$$

The calculation procedure is depicted in figure 5.4. For each axial position along the beam axis (y-axis in figure 5.4), photons are generated at random points in a plane with a radius of 2.5 mm, representing an ion beam diameter of 5 mm (see figure 5.4 on the left). Thus, the entire beam cross section contributes equally to the calculation of the detection efficiency. Photons are emitted isotropically into all directions, as it is assumed to be for fluorescence due to collisional excitation.

Figure 5.5 shows the profile of the axial position dependent detection efficiency for different beam diameters. For ion beam diameters of 2 mm and 5 mm, the detection efficiency is equal within the error bars. For a significantly bigger beam diameter of 12 mm, the absolute value of the detection efficiency is slightly lower. This is because some of the photons generated far from the beam axis hit the aperture in front of the PMT and will not be detected. Note that based on simulations [39], typically 98 to 99 % if the ions passing the optical detection region are within a beam diameter of 5 mm. More importantly the *shape* of the axial profile of the detection efficiency, which has a significant impact on the output of the response simulation, is identical for all studied beam ion diameters. A beam diameter of 5 mm has been used for further simulations. From figure 5.5, the axial width (FWHM) of the optical detection region is determined with 40.9 ± 0.2 mm for a beam diameter of 5 mm.

5.1.2 Other Applications

Apart from the calculation of the axial profile of the detection efficiency, there are two more applications of the ray tracing project at MIRACLS. These are

- An optimization program for the photon wavelength dependent distance between PMT and lens in order to obtain the best signal to background ratio. Note that for CLS

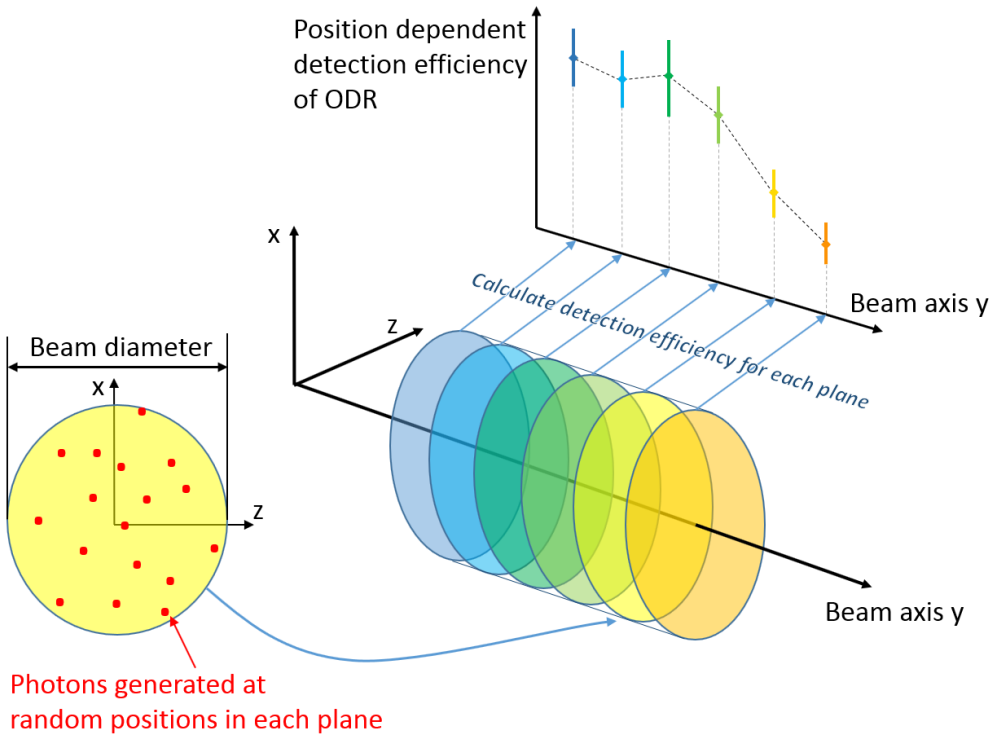

Figure 5.4: *Schematic representation of the detection efficiency calculation. Photons are generated at random points within the coloured planes. For each plane, the detection efficiency is calculated and hence, each plane corresponds to one data point in the detection efficiency diagram.*

studies, the photon emission is not necessarily isotropic and a more accurate description of the emission pattern is required (see appendix E.2).

- Size and position of a second aperture in close proximity to the ion beam which may reduce the laser stray light in CLS studies.

Both are discussed in detail in appendix E.

5.2 SIMION Simulations of Ion Trajectories in the MR-ToF Device

The trajectories of ions stored in the MR-ToF apparatus are simulated using SIMION [40]. The present simulations follow closely the procedures described in previous work [29] [39]. This section limits its explanation to a few concepts of the simulation that are used in the next section.

The simulation procedure includes three subsequent steps: First, the ions are injected into the Paul trap where they are thermalized. Using the ion distribution injected from the Paul trap, the second simulation step propagates the ions through MIRACLS' proof-of-principle setup from the Paul trap to the MR-ToF device. The storage of the ions in the MR-ToF device is again simulated separately. This third step uses the cylindrical symmetry of the MR-ToF device to simplify the simulation and gain optimal accuracy.

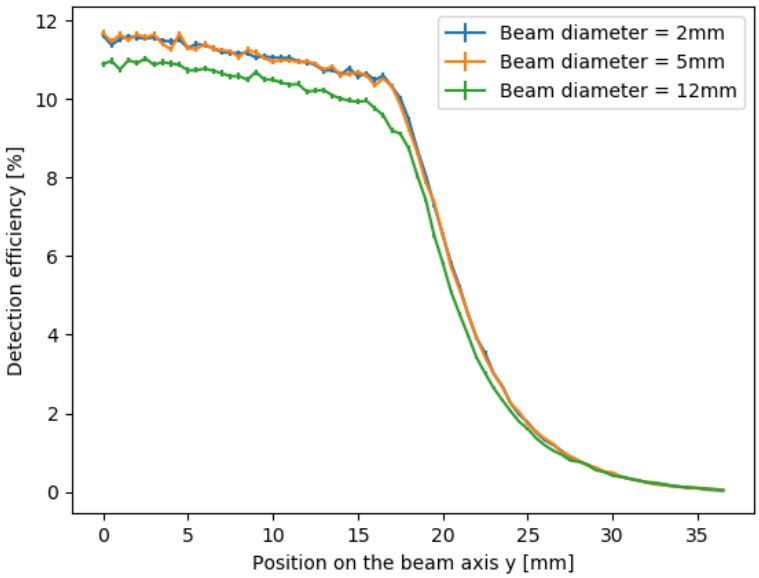

Figure 5.5: *Simulated photon detection efficiency pattern of the optical detection region for a wavelength of* 280 nm *and different ion beam diameters. The position* $y = 0$ *is the center of the optical detection region and the detection efficiency profile is symmetric in both* y *directions.*

5.2.1 Simulation of Space Charge Effects

In SIMION, the simulation can be run with and without Coulomb interaction between the ions. Without interaction, the ions are propagated through the setup one after another. As the ions are completely independent from one another, simulations without interaction have linear complexity, i.e. twice as many ions require twice as much calculation time.

For low Paul trap loading times and therefore small numbers of ions in the MR-ToF device, Coulomb interactions between the ions are assumed to be negligible. For these cases, simulations without interaction between the ions are suitable.

If the simulation includes interactions between the ions, all ions have to be simulated at once and their respective Coulomb interaction has to be considered. As all the ions interact with one another, the complexity of this simulation method is $N!$. For practical reasons, not more than 100 ions in the MR-ToF device were simulated with this method.

To approximate the ion dynamics with higher ion numbers, a **repulsion factor** [41] can be introduced without increasing the computational costs. The repulsion factor defines how many particles are represented by one ion in the simulation. For example, a simulation with 100 ions and a repulsion factor of 40 represents 4000 ions in the MR-ToF apparatus.

5.2.2 Output of the SIMION Simulations

The SIMION simulations are configured so that they **record** an ion every time it passes a certain **plane** in the simulation area. The record planes can be defined by the user. The output of a SIMION simulation is a list of ion positions, velocities, masses, energies and time of flight at the moment that they passed one of the record planes.

5.2.3 Residual Gas in the MR-ToF Device

The simulation process does **not** include any considerations about the gas in the MR-ToF device that is leaked in during collisional excitation. Thus, when comparing the simulation results to collisional excitation experiments, there are two things to keep in mind:

- Losses of ions due to collision with the gas are not included in the simulation. This means that experimental data at the used residual gas pressures always has higher losses than the corresponding simulation.
- As the excitation mechanism itself is not considered directly in the SIMION simulation, a constant excitation rate is assumed when calculating the temporal response. Therefore, the photon counts gained by the simulations are given in arbitrary scales and are adjusted in height to the experimental data.

5.3 Simulating the Time Profile of Fluorescence Emitting Ions Passing the ODR

The last step of the simulation is to calculate the histogram over time of photon counts from collisional excitation while an ion bunch passes through the ODR. In the calculation, there is a constant excitation rate and photons are emitted instantaneously. Considering a lifetime of a few nanoseconds of its first excited states, this assumption is justified at least for Mg^+ ions since during 1 ns, $^{24}Mg^+$ ions travel approximately 114 µm at 1.6 keV. The calculation of the time profile combines the ion positions obtained from SIMION simulations and the detection efficiency profile of the optical detection region.

5.3.1 Calculation of Ion Positions in the Optical Detection Region

The drift tube is made of a metal mesh that allows photons to pass through to the optical detection setup and on the other hand keeps the electric potential inside of the drift tube constant [39]. This implies that the ions propagate in a field free region such that the velocity of the ions should stay constant within the optical detection region. Hence, it should be possible to calculate the position of an ion by just knowing its velocity and time of flight when it passes the center of the drift tube.

To confirm this assumption, additional transverse record planes have been added to the SIMION simulations at ±30 mm from the central plane. Using the time when an ion arrives at a record plane and the velocity that it has at this point, one can calculate when the ion would arrive at the next record plane 30 mm further. This prediction has been compared with the time when the ion arrives at this next record plane in the drift tube. For space charge simulations up to a repulsion factor of 100 (i.e. representing 10 000 ions) as well as for simulations without Coulomb interaction, the relative precision of this prediction is at least 10^{-5}.

For further calculations, it is therefore always assumed that the velocity of the ions does not change inside of the optical detection region.

5.3.2 Simulation of the Optical Detection of Fluorescence Light

The histogram of photon counts versus time is calculated as follows:

1. A range and bin width for the time axis is chosen and the time axis is generated which is an array of points in time.
2. For each of these time steps, the SIMION data is used to calculate the position of each ion in the MR-ToF apparatus. This is done based on the ions' velocity and the times when they are at position 0 (in the center of the detection region).
3. The resulting detection probabilities for photons emitted from all individual ions are added up for each time step. The detection efficiency profile of the optical detection region has been calculated for steps of 0.5 mm. Between these points, the detection probability is interpolated linearly.

This procedure is schematically depicted in figure 5.6. The result is a signal with the ion time of flight on the x axis and photon counts (arbitrary units) on the y axis, as depicted on the right side of figure 5.6. The result is finally scaled in height to experimental data from collisional excitation which allows the comparison between experiment and simulation.

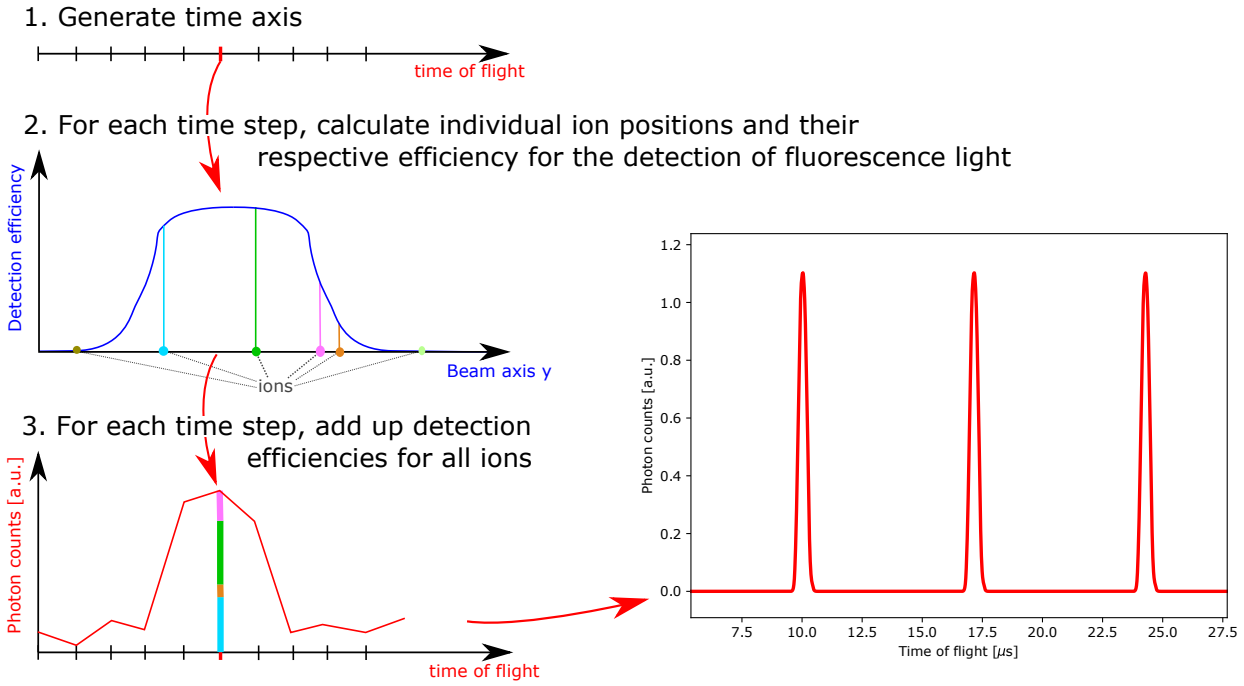

Figure 5.6: *Calculation of the histogram of photon counts versus time. The result can be seen on the right side. For details see text.*

5.3.3 Comparison of Ion Bunch Width and Fluorescence Signal Width

As a first benchmark, the width of the peaks in the photon count histogram and of the corresponding ion bunch from the same simulation are compared.

The ion bunch time spread can be calculated directly from SIMION simulations. As already explained earlier, ions are recorded every time they pass the center of the MR-ToF device which is also the center of the ODR. A drawback of this method is that the SIMION record plane is an infinitely thin detection region. For the PMT signal on the other hand, the ion positions have been convoluted with the detection region profile shown in figure 5.5, which has a finite width.

Figure 5.7 reveals that the optical detection region profile makes a difference:

- If the ion bunch width is in the same order of magnitude as the length of the ODR, there is a significant gap between the time spread of the ion bunch and the signal detected with the PMT of the ODR.
- For ion bunches wider than two times the length of the ODR (or a time spread of more than 0.72 µs for $^{24}Mg^{+}$ ions at 1.6 keV), the ion bunch time spread is essentially identical to the time profile observed in the ODR since its axial length becomes more and more negligible in comparison to the ion bunch. This is however far longer than what is aimed for in practical applications in MIRACLS' PoP setup.

By delivering peak widths that can be compared to experimental results measured with collisional excitation, the present characterization of the optical detection region brings an indispensable benefit to the simulation process which is illustrated in the next chapter.

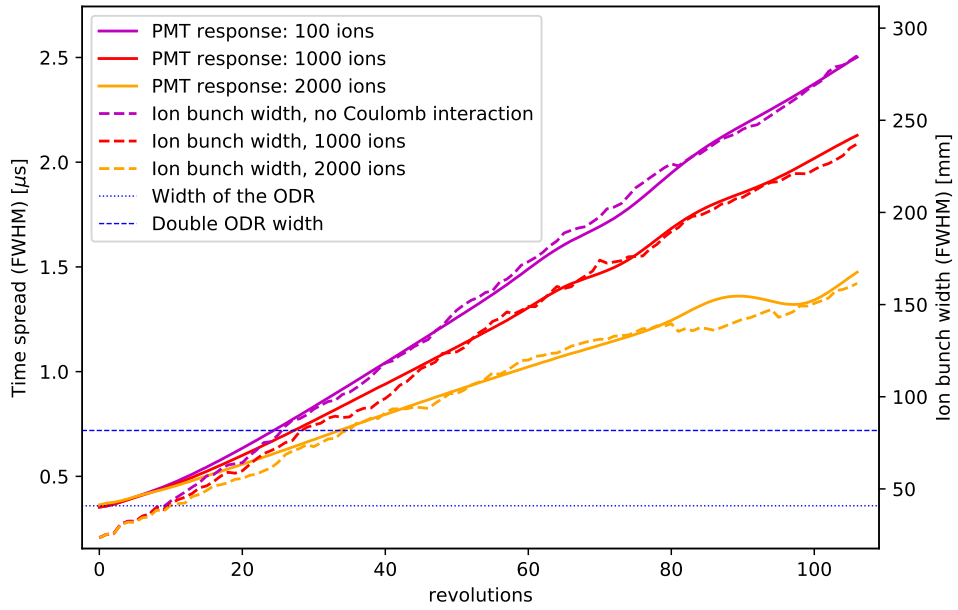

(a) Full plot range

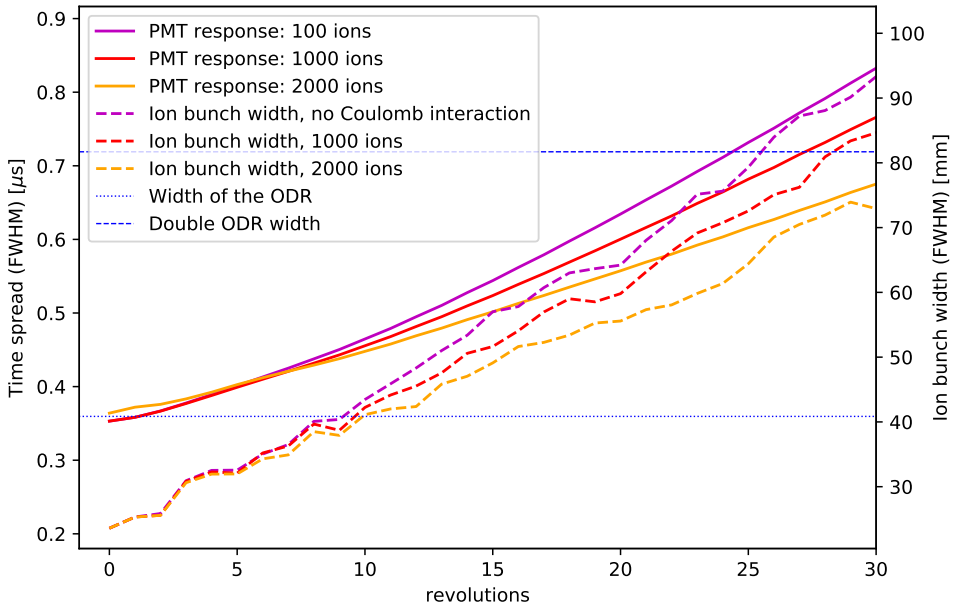

(b) First 30 revolutions

Figure 5.7: *Time spread and spatial width (both FWHM) of a $^{24}Mg^{+}$ ion bunch and the corresponding response of the ODR. The right y-axis shows the spatial ion bunch width (only applied to dashed lines) calculated from the ion velocity. The length of the ODR (≈40 mm) and the twice the length of the ODR (≈80 mm) are indicated with blue dashed lines. Simulated for 106 revolutions, a in-trap lift voltage of 700 V and different repulsion factors.*

Chapter 6

Study of Ion Bunch Properties in the MR-ToF Device

With the improved simulations described in the previous chapter, it is now possible to compare the simulated photon count histogram to actual measurement results from collisional excitation.

A first benchmark of the simulations is done in section 6.2 using easy accessible observables of the photon count histogram, such as the peak shape and the ions' revolution period, which can be extracted from the periodically re-occurring fluorescence signal. This first comparison will be done for low numbers of stored ions in which space-charge effects are not important.

Once the validity and its potential limitations of the simulation approach are established, the discussion will extend to larger ion samples confined in the MR-ToF device. The comparison of simulation and data from collisional excitation will investigate to which extend the approximation of a simple repulsion factor (see section 5.2.1) in the simulation results in an accurate description of the ion dynamics when many ions are simultaneously stored in the MR-ToF device. As self-bunching and other space charge related effects have a strong impact on the width of the ion bunches, the peak width measured with fluorescence detection is one of the most interesting figures obtained from collisional excitation measurements. To get these parameters from a collisional excitation measurement result (which is a photon count histogram versus time of flight), a dedicated peak fitting tool has been created. A guide on how to use this tool can be found in appendix F.

6.1 Collisional Excitation Measurements

All collisional excitation measurements have been done with an offline magnesium source, which produces ions of the three stable magnesium isotopes ^{24}Mg, ^{25}Mg and ^{26}Mg according to their natural abundances. As one can see in table 6.1, ^{24}Mg is about eight times more abundant than ^{25}Mg and ^{26}Mg. Therefore, the ^{24}Mg peaks are more intense than those of the other isotopes. Nevertheless, the peaks of ^{25}Mg and ^{26}Mg have to be included in the fit models to obtain reasonable results. Just fitting peaks of ^{24}Mg would lead to higher peak amplitudes and areas every time the peaks of different masses overlap.

Figure 6.1 shows an example of a collisional excitation measurement with natural magnesium

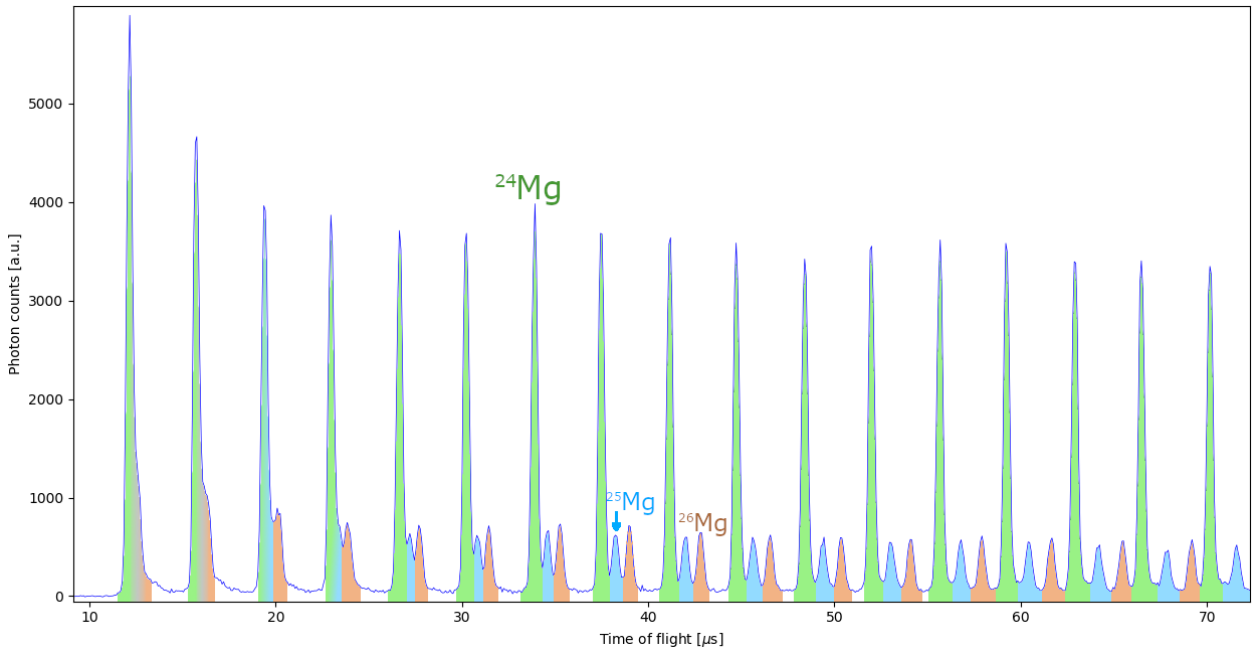

Figure 6.1: *Collisional excitation measurement of magnesium ions in the MR-ToF device. The high spikes are ^{24}Mg (highlighted in green), the smaller peaks are ^{25}Mg (blue) and ^{26}Mg (brown). In the first revolutions, the peaks are overlapping so that it is not possible to distinguish the different masses. This measurement has been conducted in March 2019, using a loading time of* 800 µs *and an in-trap lift voltage of* 700 V.

for the first few revolutions in the MR-ToF apparatus. It is clear that the different magnesium masses are overlapping in time for the first few revolutions and that they gradually get separated with longer flight times (i.e. with more revolutions in the MR-ToF device).

Table 6.1: *Abundances of stable magnesium isotopes. Data taken from [42].*

Magnesium isotope	**Abundance**
^{24}Mg	78.99 %
^{25}Mg	10.00 %
^{26}Mg	11.01 %

First collisional excitation measurements have been done in March 2019, before the work on this thesis had been started. These first measurements used in-trap lift voltages of 700 V and 995 V and have been used in an earlier publication [3].

After both MagneToF detectors had been installed and characterized as described in chapter 4, another set of collisional excitation measurements has been conducted in July 2019. These measurements have been done with in-trap lift voltages of 700 V and 850 V. As explained in section 3.4.2, operating the MR-ToF device with an in-trap lift voltage of 700 V is especially interesting because this is the regime where self-bunching can occur. The in-trap lift voltage of 850 V has been chosen because it is in the isochronous operation area of the MR-ToF apparatus. An overview of all measurements done in the second campaign is can be found in appendix D.

6.2 First Benchmark of Simulations with Small Numbers of Stored Ions

As a first benchmark of the simulation, figure 6.2 shows the experimentally measured and the simulated shapes of peaks for different revolution numbers. This data has been taken from [3], where it has been found that Coulomb interactions between the ions are negligible for a Paul trap loading time of 25 µs. Therefore, the simulation has been done without interaction between the ions.

One can see that the *peak shapes* agree very well between experiment and simulation. This supports the validity of the simulation approach in this first example. The *ions' revolution period* on the other hand do not agree between experiment and simulation. Therefore, the x-axes of the plots in figure 6.2 had to be shifted in time to the peak center.

The different revolution periods in experiment and simulation require further investigations. The blue plot in figure 6.3 shows the simulation of the revolution times in the MR-ToF apparatus for different ion energies, that has already been discussed in section 3.4. The orange lines are revolution times extracted from laser spectroscopy measurements that have been performed in 2018. Revolution times gained from the first collisional excitation campaign are marked in green. One can see that the revolution times of the laser spectroscopy measurements and the first collisional excitation campaign agree very well, but they do not agree with the simulation. Based on the respective isochronous mode of the simulated blue curve and the experimental orange curve, there is an energy difference of $\Delta E = 57$ eV and a difference in revolution period of $\Delta T = 19.6$ ns. For completeness, it is remarked that the revolution period of an ion bunch in the MR-ToF has been found to be independent of the number of ions in the bunch. Therefore, the following discussion applies to measurements with higher charge densities as well.

6.2.1 Possible Reasons for the Disagreements

Before starting the second collisional excitation campaign in July 2019, different possible reasons for the mismatch in revolution times have been investigated.

SIMION Simulations

The following issues in the SIMION simulations have been investigated. However, none of them was found to be the reason for the disagreement in revolution times with the experiment:

- Previously, the approximate mass of 24 amu was used for ^{24}Mg rather than the exact atomic mass. Some simulations have been done again for an in-trap lift voltage of 700 V and the exact atomic mass, but the revolution times did not change significantly.
- All potentials used in the simulation have been compared to the voltages in the setup. There was a slight disagreement in one of the mirror potentials, but it was less than 1 % and did not affect the outcome of the simulation.

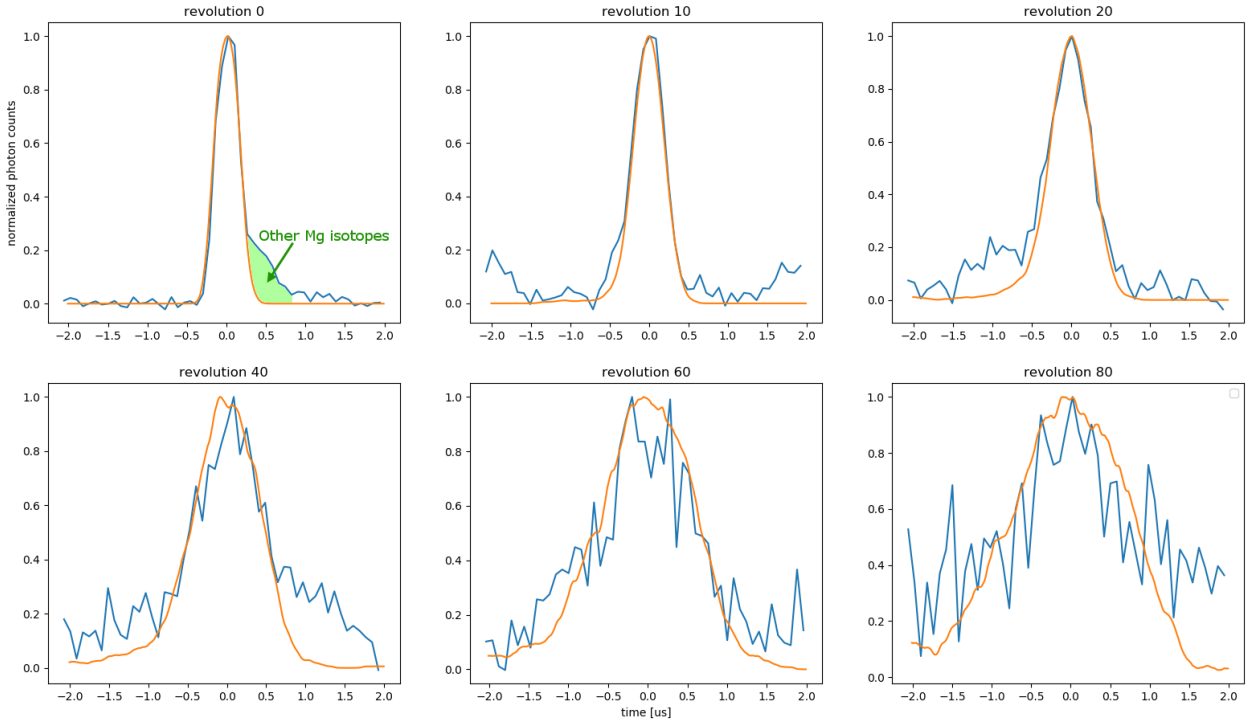

(a) $U_{Lift} = 700V$

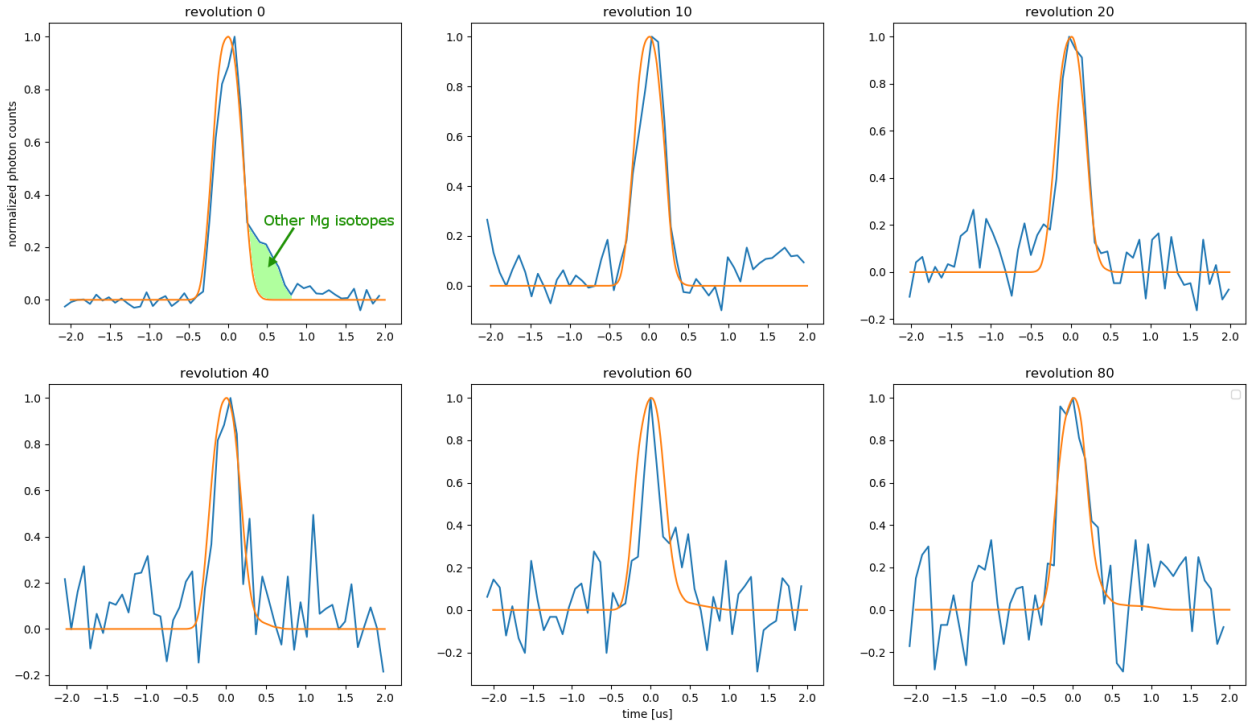

(b) $U_{Lift} = 995V$

Figure 6.2: *Peak shapes of the fluorescence-light intensity associated with selected revolutions of* $^{24}Mg^{+}$ *in the MR-ToF device for different in-trap lift voltages. The orange line is the simulated signal of the PMT (without interaction between the ions), the blue line is experimental data (recorded with a Paul Trap loading time of* $25\,\mu s$*). The peak amplitudes have been normalized to enable comparison of the peak shapes. Peaks that are possibly produced by other Magnesium isotopes are highlighted in green.*

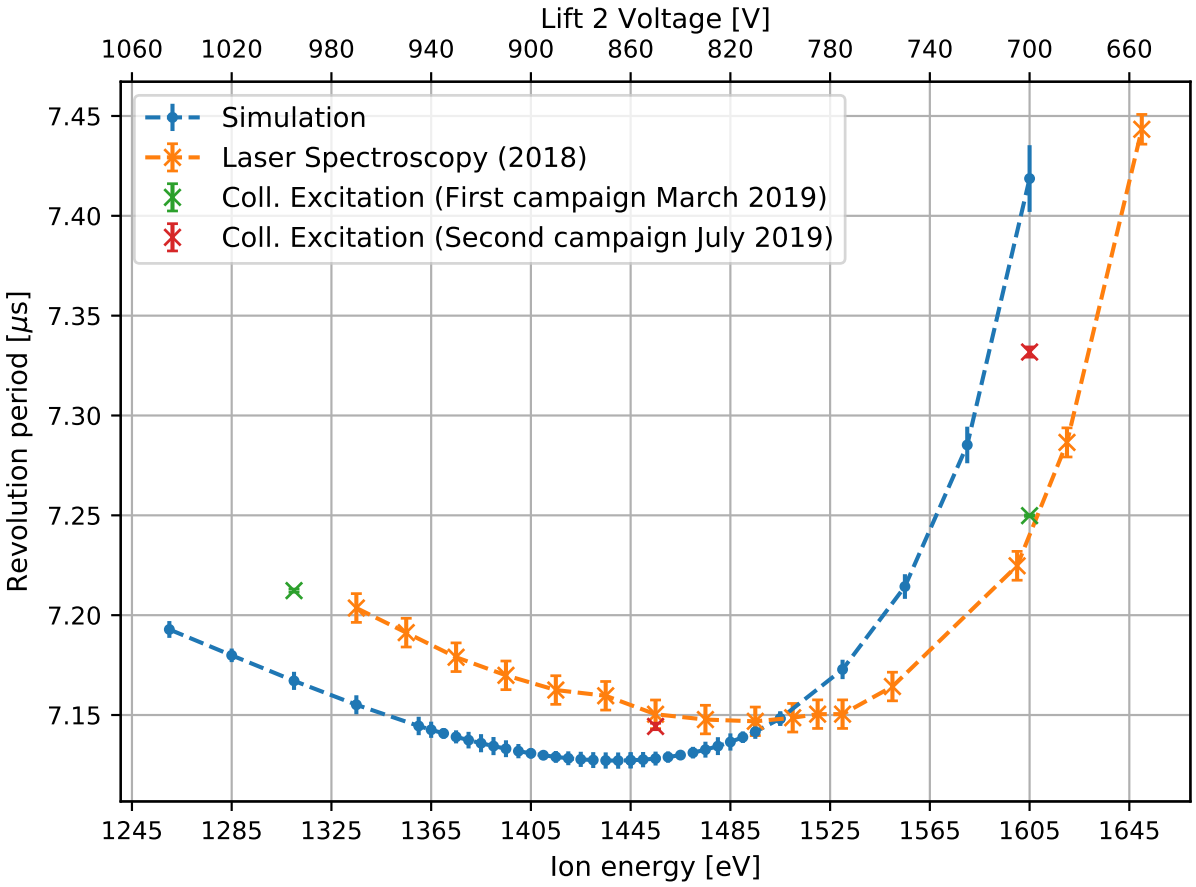

Figure 6.3: *Revolution period of ^{24}Mg in the MR-ToF device. The blue plot is the simulation data that has already been shown in figure 3.4. The other plots and data points are values found in different experiments.*

Moreover, the spatial dimensions of the MR-ToF devices are consistent between simulation and the constructional drawings of the MR-ToF apparatus. However, due to tolerances it is possible that the exact length of the MR-ToF device is not exactly the same as in the drawings. Using the difference in revolution period ΔT and the ions' typical velocities, the difference in revolution period at the isochronous mode could be explained if the central drift tube is around 2.1 mm (or 1.2 %) longer than in the drawings. Unfortunately, this can only be verified by opening the beamline and physically checking the length of the MR-ToF device. Moreover, it does not explain why there is an energy shift between experiment and simulation.

Switching of the Lift Potentials in the PoP Setup

When setting up the proof-of-principle experiment, it had been checked that the high voltage switches attached to lift 1 and the in-trap lift switch to the right voltage level. These tests did however not consider the switching time and it would therefore be possible that the switches do not toggle to the right voltage fast enough.

This has been investigated in advance of the second collisional excitation campaign. As there was no suitable high voltage probe for the oscilloscope available, the switches were tested with voltages between 100 V and 200 V rather than the 2 kV of lift 1.

It has been found that the in-trap lift switches to its target voltage within 250 ns, which is fast enough considering that one revolution in the MR-ToF apparatus takes more than 7 µs. However, when switching lift 1 from −100 V to ground, the voltage it did not go to 0 V within the 250 ns switching time, but stopped at approximately −6 V. The voltage would then slowly decline from this level to ground within a few tens of microseconds. This behaviour is shown in figure 6.4.

When lift 1 does not switch to ground but instead to a small voltage below ground, the consequence could be that the ions get less energy compared to what they would have when lift 1 switches properly. This could explain the different revolution times in experiment and simulation.

To check on this hypothesis, the high voltage switch for lift 1 has been exchanged for a new device. The switching characteristics of this new device have been inspected with the oscilloscope as well and are shown in figure 6.5. With the new high voltage switch, lift 1 now toggles from −100 V to −1.88 V within 250 ns, which is an improvement by a factor of more than 3.

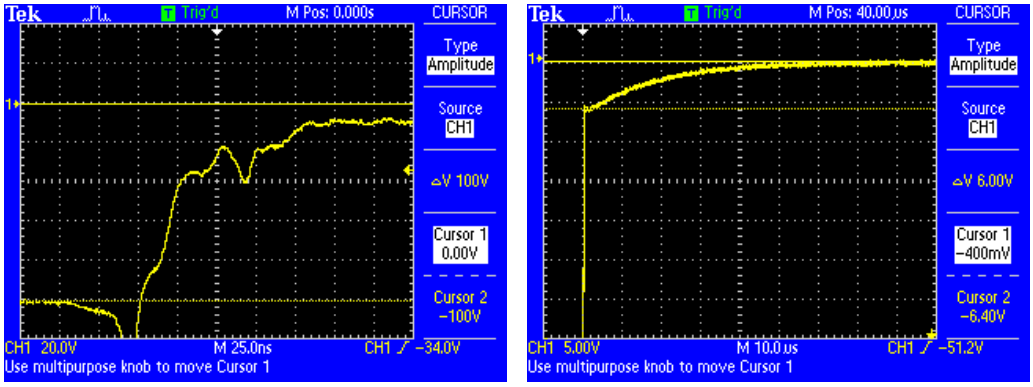

(a) Rising edge *(b) Detailed view of decay to ground*

Figure 6.4: *Lift 1 switching from* −100 V *(dotted line) to ground (solid line). The left figure shows the main rising edge. The voltage does not go to ground instantly. It stops at approximately* −6 V *and decays to ground within a few tens of microseconds, as shown in the right figure.*

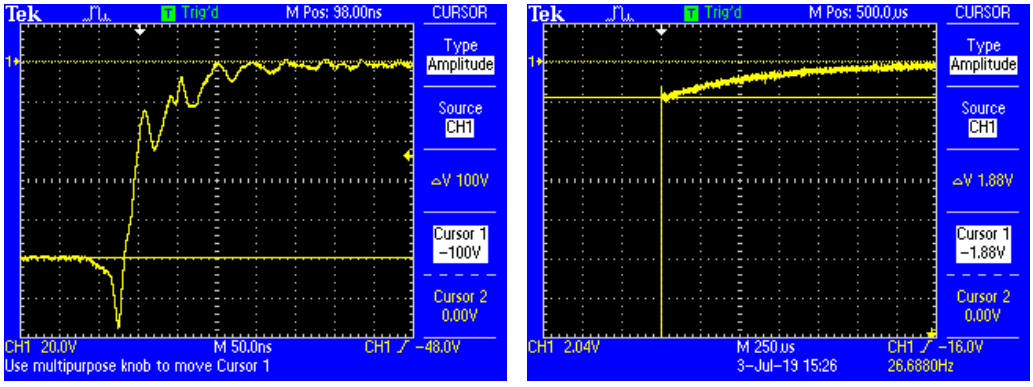

(a) Rising edge *(b) Detailed view of decay to ground*

Figure 6.5: *New HV switch installed at lift 1, switching from* −100 V *(dotted line) to ground (solid line). Lift 1 now switches to* −1.88 V *within* 250 ns *which is far less than with the old switch.*

6.2.2 Findings in the Second Collisional Excitation Campaign

In figure 6.3, one can also see the revolution times obtained from the second collisional excitation campaign in July 2019, after the new switch for lift 1 has been installed. For an in-trap lift voltage of 700 V, the revolution period has moved towards the simulation results. However, for an in-trap lift voltage of 850 V, the new revolution period is still so close to the old laser spectroscopy data that it is difficult to tell the impact of the new lift 1 switch on this operation mode.

Although it cannot be excluded entirely that the differences observed are due to other changes in the setup that have been introduced in the last months or simply due to the tuning (i.e. voltages of the ion optics inside the setup), this suggests that new switch has actually changed the behaviour of the setup and the revolution periods are now closer to the simulated values.

To be able to tell more about the impact of the new switch on the revolution time, more data is required. Especially measurements in the non-isochronous areas would be helpful, because there the differences between simulation and experiment are more significant. However, performing these measurements was outside of the scope of the present work.

6.2.3 Impact on Further Measurements and Simulations

The disagreement in the revolution time plot in figure 6.3 shows that for a selected in-trap lift voltage, the MR-ToF device in the simulation might operate in a slightly different mode compared to the actual proof-of-principle setup. While the difference in revolution time between experiment and simulation ΔT can be explained with possible differences in the spatial dimensions of the MR-ToF device, the energy shift ΔE between the isochronous mode of experiment and simulation can lead to completely different operation points of the MR-ToF device. The important figure for the development of the ion bunch width in the MR-ToF device and thus also for the peak width measured on the PMT is the slope dT/dE of the revolution time curve.

For the first collisional excitation measurements recorded in March 2019, the revolution time curve is most likely identical to the laser spectroscopy curve in figure 6.3. The slope of the revolution time curves for simulation and experiment at an in-trap lift voltage of 995 V is almost identical. One can therefore expect that experiment and simulation agree in this case. For an in-trap lift voltage of 700 V on the other hand, the slope of both curves is significantly different. This is why, that measurement was not used in the final evaluation.

As the revolution time curve for the second collisional excitation measurement is not known, the difference in operating points of the MR-ToF device between experiment and simulation is unknown as well. However, for an in-trap lift voltage of 700 V, the revolution time is closer to the simulated curve than in the first collisional excitation measurements, and we assumed that this means the operation points are better comparable.

6.3 Space Charge Effects Predicted by the Simulation

Before a detailed examination of space charge effects observed in collisional excitation is done, it is worth discussing what results are expected. Figure 6.7a shows the revolution time of an ion bunch for different ion energies in the MR-ToF apparatus, which has already been discussed in section 3.4.1.

Three specific cases, which will also be investigated experimentally, are highlighted in red and are schematically depicted in figure 6.6. For these cases, the peak width of fluorescence signals as it would be measured on the PMT detection during collisional excitation, is shown in figures 6.7b to 6.7d.

The ion bunches injected into the MR-ToF apparatus always have a small initial spread in kinetic energy. The three modes of MR-ToF operation can easily be understood by looking at how these small differences in energy affect the time spread of ion bunches, i.e. how strongly revolution time T of an ion depends on its energy E.

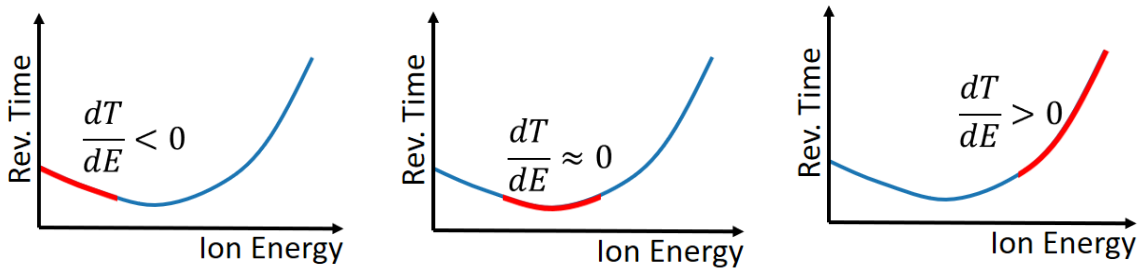

(a) Left Non-isochronous area *(b) Isochronous area* *(c) Self-bunching area*

Figure 6.6: *Schematic representation of the three MR-ToF operation areas. Details see text.*

6.3.1 Isochronous Area

For an in-trap lift voltage of 850 V (figure 6.7d), the MR-ToF device is operating in or very close to the isochronous mode, where – within a certain window – the revolution period does not depend on the ions' energies, i.e. $dT/dE \approx 0$. In this regime, small energy spreads inside of the ion bunch do not lead to a significant time spread and as a consequence, the FWHM of the peaks stays almost constant for all revolution numbers, regardless of the number of ions.

6.3.2 Non-Isochronous, Self-Bunching Area

For an in-trap lift voltage of 700 V (figure 6.7b), the MR-ToF device is operating in the non-isochronous area with $dT/dE > 0$. In this case, the more energetic ions experience a shorter revolution time in the MR-ToF apparatus than the less energetic ions. In absence of space charge effects, i.e. for low ion numbers, the small initial energy spread of the beam will result in peaks which get broader with increasing revolution number, as shown in purple in figure 6.7b.

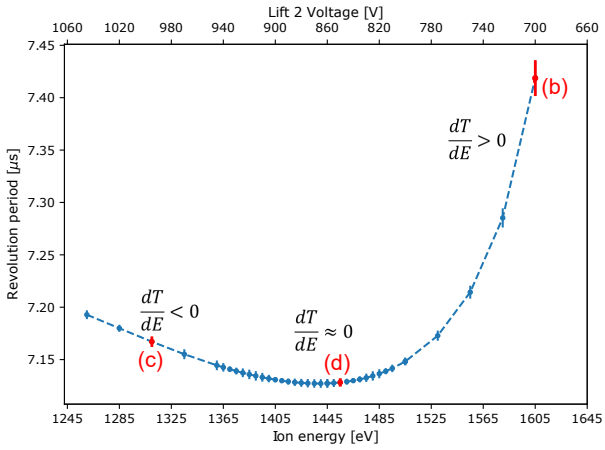

(a) Overview

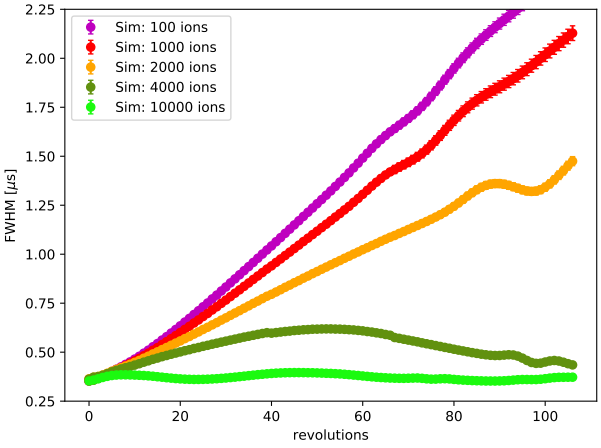

(b) In-trap lift = 700 V, Self-bunching region

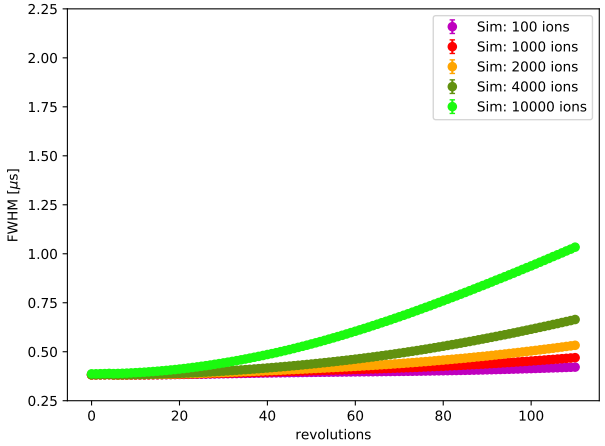

(c) In-trap lift = 995 V

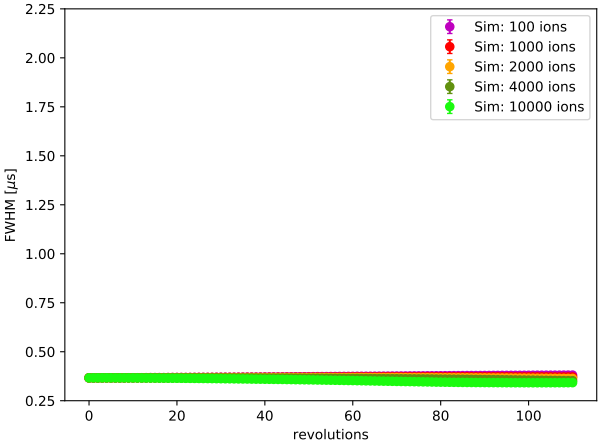

(d) In-trap lift = 850 V, Isochronous mode

Figure 6.7: *Simulations of peak widths in the MR-ToF device for different in-trap lift voltages. Figure (a) shows an overview of the simulated revolution times for different ion energies. Figures (b) to (d) show the the development of the peak width simulated including the optical detection for three different cases highlighted in figure (a).*

However, when large numbers of ions are present, the peak width remains constant even for high revolution numbers, as shown in light green in figure 6.7b. This is due to the self-bunching effect that has already been explained in section 3.4.2.

6.3.3 Left Non-Isochronous Area

For an in-trap lift voltage of 995 V (figure 6.7c), the MR-ToF apparatus is operating in an non-isochronous area as well, but with $dT/dE < 0$. This means that the less energetic ions have a shorter revolution period than the higher energetic ions. In this regime, the opposite of self-bunching occurs: the more ions there are in the MR-ToF device, the quicker the peak width increases. This means that it is generally not desirable to operate an MR-ToF apparatus in this area.

6.4 Space Charge Effects Observed Experimentally

6.4.1 Comparison Between Experiment and Simulation

During the experimental collisional excitation measurements, buffer gas is introduced into the set-up to enhance the signal. However, collisions of the ions with the buffer gas also result in losses, which is seen as a decreasing number of particles over time. These collisions are so far not included in the simulations which have a nearly stable number of particles, as mentioned in section 5.2.3. To compare the evolution of peak width over revolution number of experiment and simulation, the number of ions is a key quantity. Since this number is not stable experimentally, the results are compared to simulations performed with different number of ions, corresponding to the experimental number of ions in the beginning, middle and end, as seen in figure 6.8a.

Figure 6.8 shows how suitable simulations for a collisional excitation measurement are chosen: The left plot shows the peak areas of an experiment and different simulations normalized to the number of ions in the MR-ToF device. These simulations cover different ion numbers in the experiment for different revolutions, which means that their peak width can be compared to the experimentally measured peak widths, as depicted on the right side.

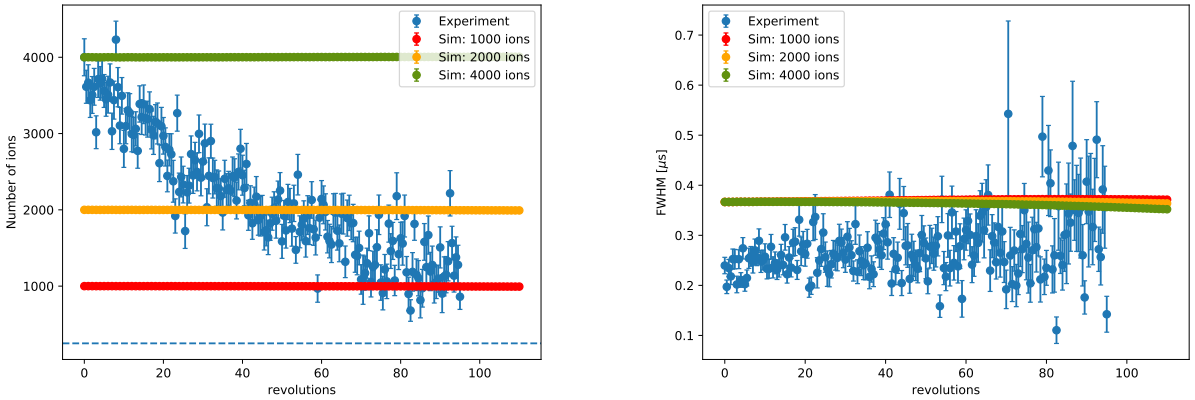

(a) *Peak area, normalized to the number of ions*

(b) *FWHM*

Figure 6.8: *Measurement result for an in-trap lift voltage of* 850 V *and a loading time of* 100 µs *compared to simulations with similar ion numbers.*
(a) The peak areas of experiment and simulation have been normalized to the number of ions injected into the MR-ToF apparatus (≈ 4000). The dashed line is the number of ions ejected from the MR-ToF device after 124 revolutions (≈ 250).
(b) Peak widths over increasing revolution number.

6.4.2 Isochronous Area

For an in-trap lift voltage of 850 V, the MR-ToF device should be operating in the isochronous mode, which means that the peaks do not disperse and the number of ions only has a very small effect on the behaviour of the ion bunches. Figure 6.10 shows the FWHM of the peaks from in collisional excitation measurements compared to different simulations. Although the peak widths of the experiments seem to be smaller than the simulated peak width, the overall trend of a nearly constant FWHM over revolution number is similar.

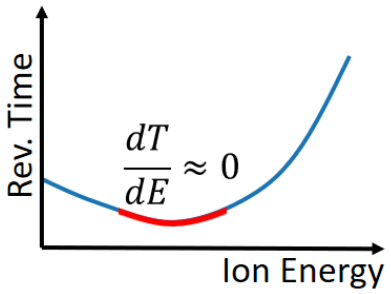

Figure 6.9: *Isochronous mode*

However, while the FWHM of the simulated peaks stays constant, the experimentally measured peaks get broader over time, especially for larger numbers of stores ions. This is an indication that the proof-of-principle MR-ToF apparatus might not be operating in a perfectly isochronous mode. As previously seen in figure 6.3, the operation modes seem to be slightly shifted between simulation and experiment and the isochronous mode of the proof-of-principle MR-ToF device seems to be rather at in-trap lift voltages of around 800 V rather than 850 V. Additionally, operating exactly in isochronous mode is hard to achieve, as mentioned in section 3.4.1.

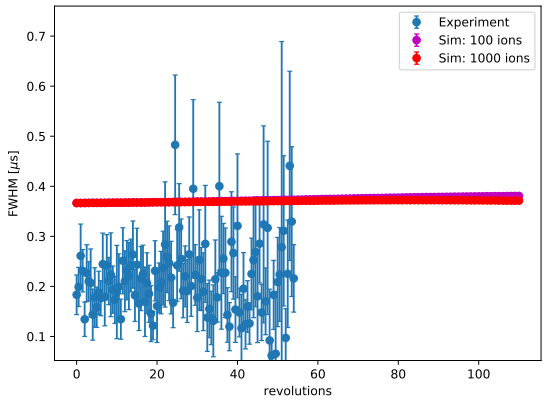

(a) *Loading time* 25 µs, ≈ 850 *ions injected /* ≈ 35 *ions ejected after 124 revs.*

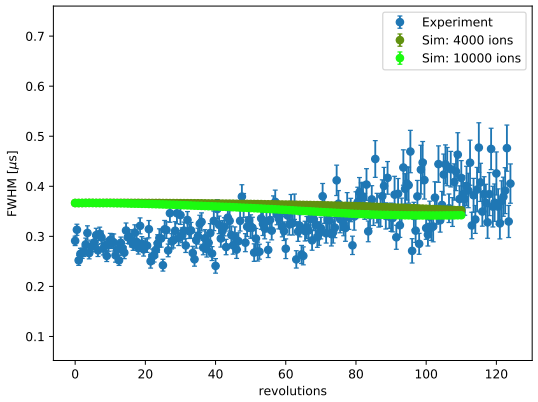

(b) *Loading time* 800 µs, ≈ 23500 *ions injected /* ≈ 3000 *ions ejected after 124 revs.*

Figure 6.10: *Isochronous mode: Peak width from collisional excitation measurements compared to different simulations with similar ion numbers. The data for a Paul trap loading time of* 25 µs *in figure 6.10a has been taken between the* 10^{th} *and the* 12^{th} *of July (combination of file004, file007 and file008, see table D.1). The collisional excitation data for a loading time of* 800 µs *shown in figure 6.10b has been taken on the* 17^{th} *of July (file096 in table D.1).*

It is important to note that while the deviation in FWHM between experiment and simulation looks very significant (in terms of error bars) in figure 6.10, it is not a very prominent effect if the peak shapes are directly compared. Figure 6.11 shows a the peak shapes of the simulation and experimental data from figure 6.10b. This figure illustrates that the simulation is still in very good agreement with the experimental results despite the seemingly huge deviations in peak width.

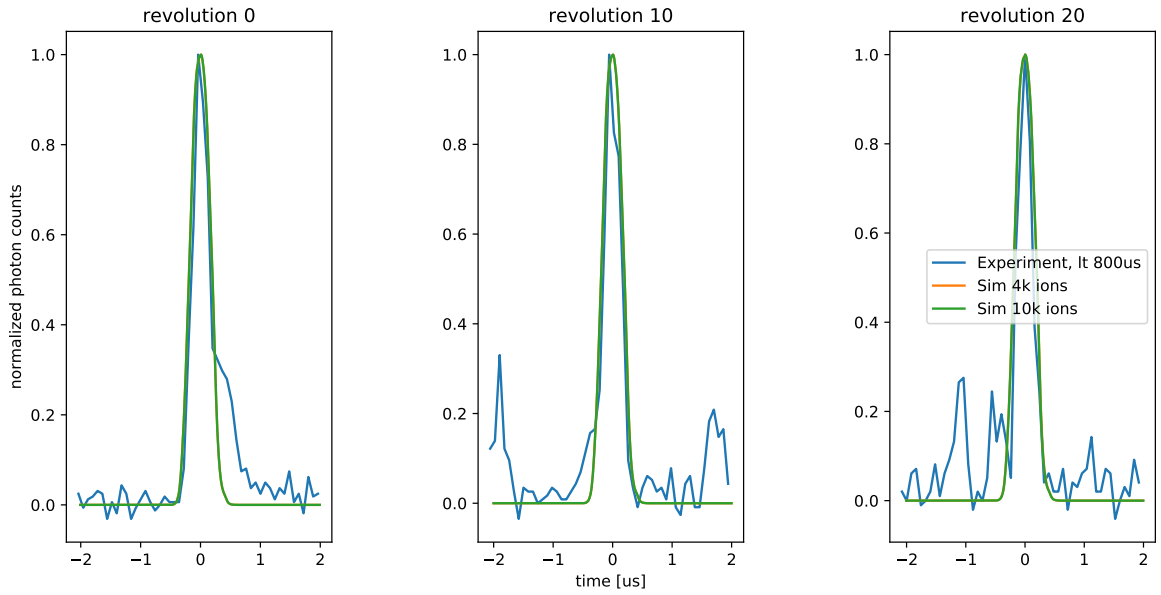

Figure 6.11: *Peak shapes of the fluorescence-light intensity associated with selected revolutions of $^{24}Mg^{+}$ in the MR-ToF device for different an in-trap lift voltage of* 850 V *and a Paul trap loading time of* 800 µs*. The orange and the green lines are simulated signals and the blue line is experimental data. All three data sets are equivalent to the data shown in figure 6.10a. The peak amplitudes have been normalized to enable comparison of the peak shapes.*

6.4.3 Non-Isochronous, Self-Bunching Area

For ion energies above the isochronous area, in this case for an in-trap lift voltage of 700 V, the ion bunches disperse quickly in the MR-ToF apparatus. Self-bunching can however keep the ion bunches together if the charge density is high enough. This behaviour can be seen in figure 6.13, which shows the fit results for the run from 2019-07-12 (file108, see table D.1) for Paul trap loading times of 100 µs and 800 µs.

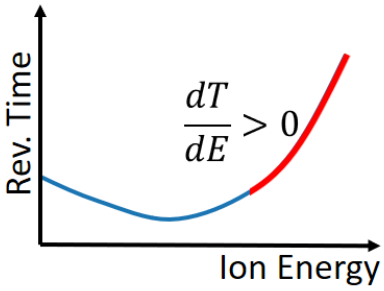

Figure 6.12: *Self-bunching area*

As discussed appendix D.1, due to unexplained changes in the setup, only some of the measurements with an in-trap lift voltage of 700 V are usable. Therefore, the statistics for these measurements are quite low and measurement data with the lowest loading times of 25 µs and 50 µs could not be fitted because of the low signal to noise ratio.

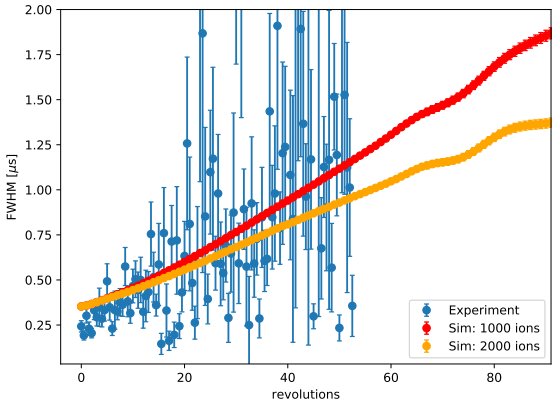

(a) Loading time 100 µs, ≈ 4000 *ions injected /* ≈ 300 *ions ejected after 124 revs.*

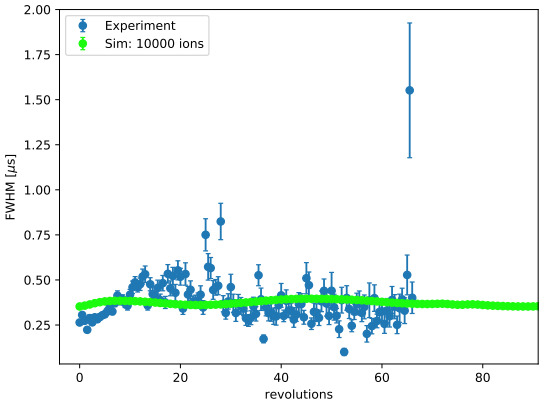

(b) Loading time 800 µs, ≈ 19000 *ions injected /* ≈ 3000 *ions ejected after 124 revs.*

Figure 6.13: *Non-isochronous mode, self-bunching area: Peak width from collisional excitation measurements compared to different simulations with similar ion numbers.*

6.4.4 Left Non-Isochronous Area

For an in-trap lift voltage of 995 V, the MR-ToF device operates at ion energies lower than the isochronous area. In this regime, self-bunching is not possible and instead the ion bunches disperse for too high numbers of ions.

The measurements depicted in figure 6.15 have been conducted in the first collisional excitation campaign in March 2019. At this time, the MagneToF detector had not yet not characterized and therefore the number of ions in these measurements is not known. Instead, the number of ions for the simulations has been chosen so that the progression of the FWHM plots matches with the experimental data. One can see that the agreement between simulation and experiment is very good in both cases shown.

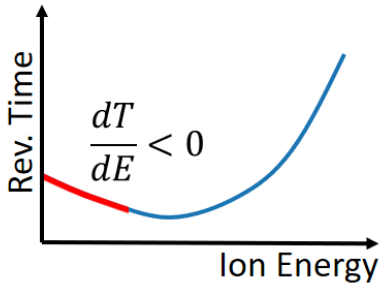

Figure 6.14: *Non-isochronous mode, low energies*

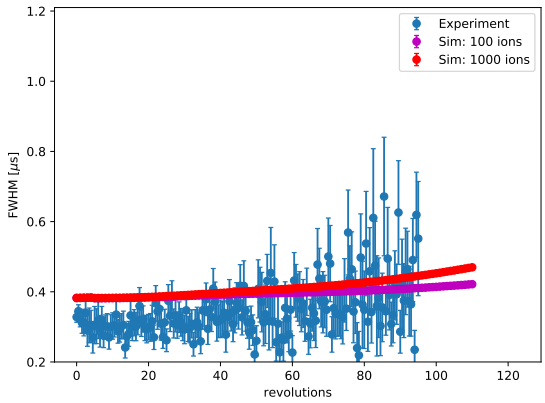

(a) Loading time 25 µs

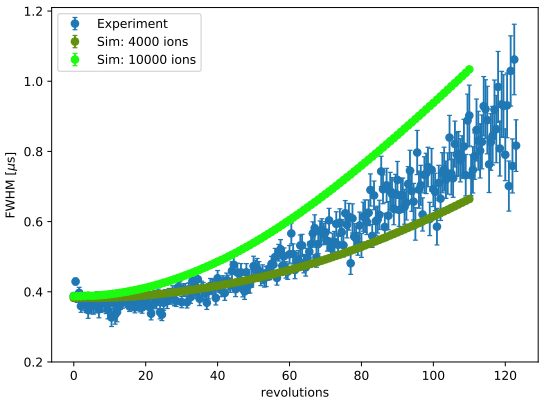

(b) Loading time 250 µs

Figure 6.15: *Right non-isochronous mode: Peak width from collisional excitation measurements compared to different simulations with similar ion numbers.*

6.4.5 Disagreements Between Experiment and Simulations

During the comparison of simulated and experimentally measured peak widths in this section, two disagreements have been found:

Experiment has Narrower Bunch Width than Simulation

In data obtained during the second campaign, the FWHM of the peaks measured with collisional excitation is in many cases smaller than the FWHM of the simulation. This can be seen very well in the isochronous mode shown in figure 6.10.

This could indicate that the ion bunch width in the second collisional excitation campaign was smaller than what was assumed in the simulation, which can be investigated experimentally using the MagneToF detectors. However, obtaining the ion bunch width at the detector position instead of the central plane of the MR-ToF requires a modification of the simulation code, which has not been implemented so far.

It is also interesting to note that the disagreements in FWHM are in the order of the experimental bin width. Hence, another Collisional Excitation Campaign with a smaller bin width might deliver more accurate results. These measurements would however take even more time to collect sufficient statistics and therefore this task is left for future works.

Unexpected Behaviour of Simulations with High Repulsion Factors

In some of the simulations, the peak width decreases which is rather unexpected.

- The FWHM simulated for an in-trap lift voltage of 700 V with 4000 ions shown in figure 6.7b decreases after 50 revolutions.
- In the isochronous mode, the peak widths should stay constant but instead, the simulated FWHM is decreasing slightly for high repulsion factors as shown in figure 6.10.

These observations are not necessarily simulation errors, as the ion dynamics in an MR-ToF apparatus are rather hard to predict and the experiments do not directly contradict with the simulations. However, SIMION's charge repulsion calculations might not be fully accurate [41], especially be for high repulsion factors. For further work with SIMION, one should therefore keep in mind that the simulations might be less reliable for these high repulsion factors.

6.5 Conclusion

This chapter has demonstrated that the improved simulation of fluorescence detection in MIRACLS' proof-of-principle MR-ToF device presented in chapter 5 has opened new possibilities for the investigation of trapped ion dynamics. Note that in many of the examples shown throughout this chapter, the peaks' FWHMs are around or less than 0.72 µs (the width of the ODR). As discussed in section 5.3.3, in this regime the correct folding of the ODR is essential to obtain the correct description of the fluorescence light's time profile in addition

to the ion bunch properties. Hence, this direct comparison of peak shapes has previously not been possible without the simulation of the optical detection region.

All in all, the agreement between simulation and experiment is very good and different space charge effects could be observed in experiment as well as in simulation consistently. The remaining disagreements seem to be present already starting from the 0^{th} revolution, hence, they are not a consequence of the space-charge.

Chapter 7

Summary and Conclusion

Recently, the experimental study of exotic, short-lived radionuclides has enormously benefited from the advent of so-called Multi Reflection Time of flight (MR-ToF) devices in which an ion beam is confined in-between two electrostatic mirrors. Today, these powerful instruments are utilized at the world's leading radioactive ion beam (RIB) facilities as fast mass separators or mass spectrometers. However, when many ions are simultaneously stored inside an MR-ToF device a too high charge density can degrade its otherwise superb mass resolving power. These so-called space charge effects are also expected to play a role in the Multi Ion Reflection Apparatus for Collinear Laser Spectroscopy (MIRACLS). This is a novel approach to high-resolution laser spectroscopy of fast radioactive ion beams which takes advantage of the unique capabilities of MR-ToF devices. As the ions are bouncing back and forth between the electrostatic mirrors, the trapped ion bunch interacts with the spectroscopy laser during each revolution in MIRACLS, compared to only once in conventional collinear laser spectroscopy (CLS). This increased laser-ion interaction time translates into an improved sensitivity and allows radionuclides to be probed experimentally at MIRACLS which are outside of reach for today's methods.

The focus of the present thesis the study of space charge effects in MIRACLS' proof-of-principle MR-ToF apparatus. As already shown in previous work, a potential tool for the investigation of ion bunch dynamics inside of an MR-ToF device is the detection of fluorescence photons induced by collisions of trapped ions with residual gas. These so-called collisional excitation measurements deliver a histogram of photons counts over time of flight with peaks each time the ion bunch passes the optical detection region located in the center of the MR-ToF device. The observables relevant for space charge effect are especially the peak width which correspond to the ion bunch width, but also the revolution period of the ion bunch as well as other parameters related to the peak shape. However, in order to perform quantitative studies, knowledge about the absolute ion number within an ion bunch is required. Additionally, the (axial) ion position dependent detection efficiency of the ODR has to be folded with the length of the ion bunch in order to directly compare the experimental data from the fluorescence detection to simulations of ion trajectories inside the MR-ToF device. Both has been achieved in the present work.

To determine the number of ions, two MagneToF ion detectors (MagneToF Mini 14924) have been installed, one in front as well as one downstream of the MR-ToF device. A calibration and characterization procedure for the MagneToF detectors has been developed, which can be applied to future detectors as well. It has been found that the integrated signal from the

MagneToF detectors A_{signal} depends linearly on the number of ions N with $A_{signal} = N \cdot A_{1ion}$. The average peak area for one ion A_{1ion} is specific to each detector and potentially also to each ion species or mass. The linear law could be validated up to 10 000 ions within an ion bunch (with a typically width of a several 100 ns) impinging on the detector, which is sufficient for most applications presented in this thesis. It may hold valid much beyond this ion number but observed non-linearites could not be unambiguously associated with the MagneToF detector or other components of the measurement setup.

Existing simulations of ion trajectories inside of the MR-ToF device have been extended with a model of the fluorescence detection and the optical detection region located in the center of the MR-ToF apparatus. It has been found that the optical detection region has a finite width of approximately 41 mm (FWHM) along the beam axis and that the axial profile of the optical detection efficiency is independent of the radial ion bunch size (within typical dimensions of the ion bunch). This delivers a better understanding of the optical-detection characteristics which can be applied in many different ways, e.g. in the design of a new aperture sets to reduce laser stray light in CLS studies at MIRACLS. Most importantly, the characterization of the optical detection region has shown to be an indispensable enhancement to the simulation process, that enables the direct comparison of simulation results and collisional excitation measurements.

Both previously described advances have successfully been employed in studies utilising collisional excitation. First benchmarks of the simulation with measurement results at low charge densities have shown an excellent agreement in the signal shape and width. It has however been found that the operation mode of the proof-of-principle MR-ToF device deviates from the simulation in both revolution period and energy. While the shift in revolution period could be possibly attributed to machine tolerances of the MR-ToF device, the reason for the energy shift is more difficult to identify and has a higher impact on MR-ToF operation. A new high voltage switch has possibly solved this problem as well, but further investigation is required to be certain.

In a second step, these comparisons where extended to many simultaneously trapped ions (in the order of several 1 000). Different space charge effects have successfully been observed experimentally and are showing consistency with the predictions by the simulations. For the theoretical study of space charge effects, charge repulsion factors had to be introduced to the simulation in order to reduce the computation time to an acceptable limit. Numerical deviations in the signal widths up to the 35 % level are likely not related to space charge effects. Instead, they rather seem to be attributed to systematic factors, such as the beam preparation in the Paul Trap or the experimentally used time resolution.

In case an even higher simulation accuracy is required exceeding the level at which the present benchmark has identified shortcomings, future work could concentrate on the following. The ion bunch width could be measured in the proof-of-principle setup using the MagneToF detectors. While this does not provide in-site information about ions stored inside the MR-ToF device itself, it provides an additional benchmark of the simulation process that is independent of the fluorescence detection process. Moreover, collisions of the ions with the gas in the MR-ToF device could be implemented into the simulation, among others to consider the dominant ion-loss mechanism due to collisions in the simulation. The observed energy difference in the MR-ToF operation between experiment and simulation should also be further investigated. This mainly requires more measurements of the revolution period for different ion energies, but also examination of MIRACLS' proof-of-principle by ensuring

the proper HV switching in the definition of the ions' kinetic energy and by a cross check in the axial dimensions in the experimental MR-ToF apparatus, in particular the less rigid central drift tube. Finally, losses in the simulation accuracy are expected for higher repulsion factors in the Coulomb interaction.

In summary, the simulations of ion trajectories in the MR-ToF device including the characteristics of the optical detection region now provide a good forecast for the actual measurement results. Hence, this work opens the path to more systematic investigations and to predict the influence of space charge effects on experiments in MR-ToF devices. This could help to advance MR-ToF based mass separators to higher ion flux and is of particular importance for laser spectroscopy of exotic radionuclides at MIRACLS.

Appendix A

MagneToF Mini 14924 Datasheet

ETP ion detect

ETP Preliminary Datasheet – Subject to Change
Revised 29 May 2017

14924 MagneTOF™ Mini Preliminary Datasheet

Specifications

Model Number	14924
Multiple-ion pulse width (FWHM)	≤1.5 ns
Input aperture size (nominal)	25 X 17 mm
Mechanical envelope size (nominal)	59 X 55.5 X 45 mm
Pulse linearity (typical)	500 mV into 50 Ω
Maximum sustained linear output current (typical)	5 µA
Maximum dark counts at 2600 V	50 per minute
Maximum dark current at 2600 V	1 pA
Maximum operating pressure	10^{-4} Torr
Long/short term storage requirements	Protect from dust and humidity
Low mass ion detection efficiency (nominal)	92%
Maximum supply current	300 µA
Typical gain at 2000 V (new detector)	1E6
Operating voltage range*	~1900 V (initial) to 3500 V (aged)

*Note: Operating a new detector at end-of-life (maximum) voltage may result in damage to the detector.

Typical Gain Curve

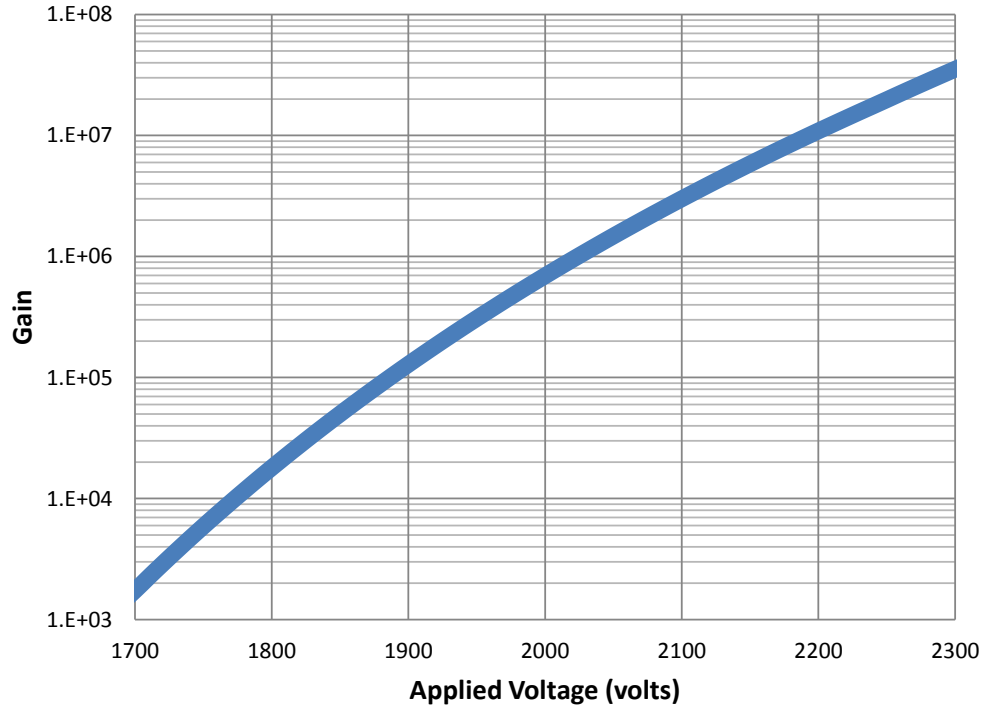

ETP ion detect

Mechanical Specification

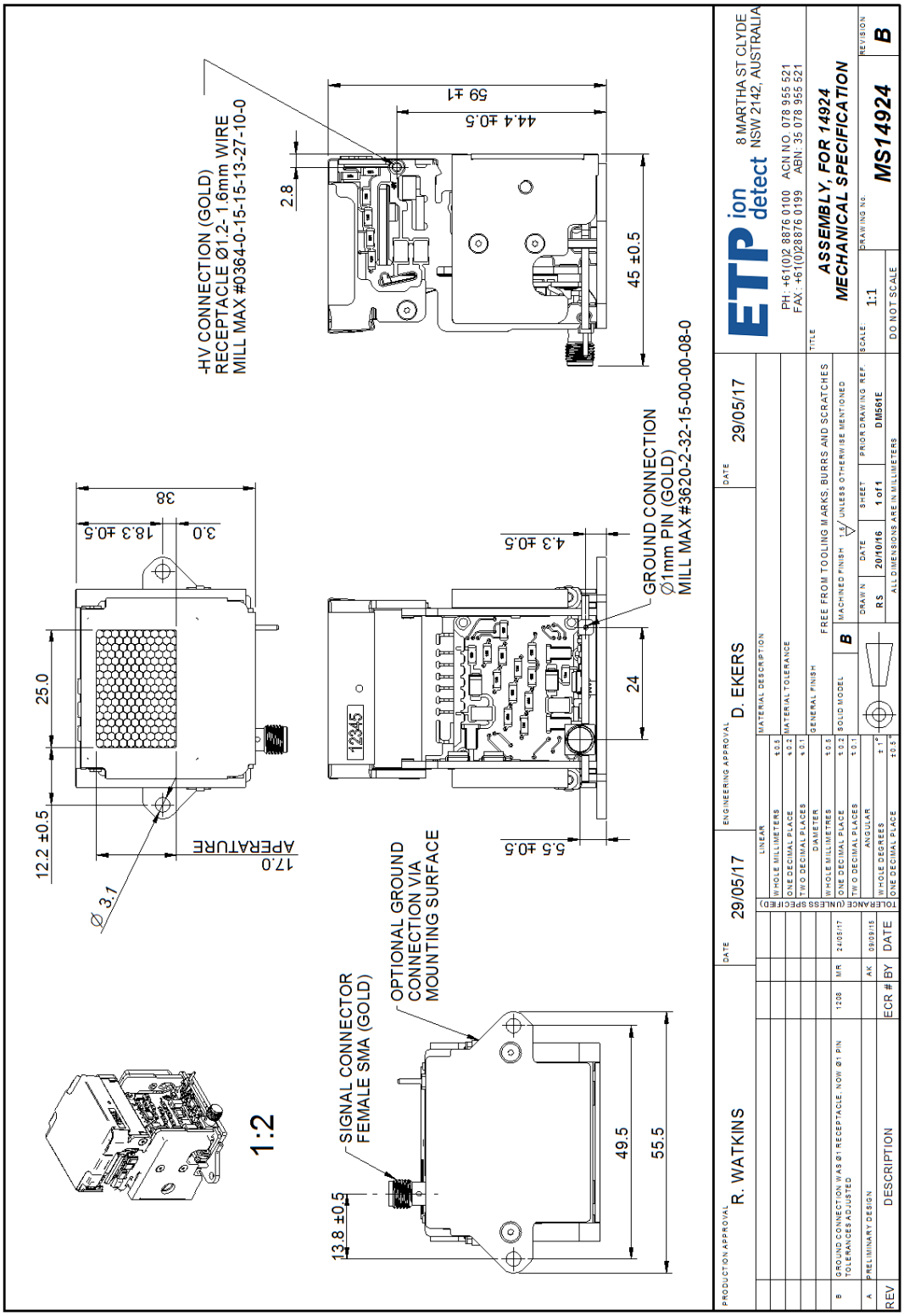

Appendix B

Further Analysis of MagneToF Measurements

B.1 Further Comparison Between Characterization Methods

In this chapter, the two different MagneToF characterization methods described in chapter 4.1 are further discussed and compared. These two methods are:

- The **Single Ion Peak** method describes in section 4.1.2, where the oscilloscope triggers directly onto ion events from the MagneToF detector and
- The **Signal Integration** method described in section 4.1.3, where the oscilloscope triggers on the Paul trap release and therefore there can be multiple ion peaks in one measurement.

Figure 4.10 showed already a comparison between the peak area distributions obtained with these different methods. In these plots, the distributions from the signal integration measurements agree with the single ion peak analysis if there is only a low number of ions in each event. For higher ion beam intensities however, the peak area histograms obtained with the signal integration method are considerably narrower than the peak area distribution from the single ion peak analysis.

Hence, the question arises whether the agreement peak area distributions for low ion intensities is just coincidence and the two characterization methods are not consistent, or there is a connection between these methods even if they partly seem to disagree at the first glance. To this end, a program has been developed that simulates signal integration measurements based on the peak area distribution obtained form the single ion peak analysis.

This algorithm works as follows:

1. Choose a number of ions per shot n.
2. For each number of ions per shot, 10000 shots (each representing one trigger event on the oscilloscope) are simulated and for each shot the actual number of ions is distributed around n with a Gaussian probability distribution.

3. The area of each ion peak in a shot is generated according to the distribution obtained in the single ion measurements shown in figure 4.5.
4. The sum of all peak areas and the number of peaks is saved in the same format as the signal integration measurements. Therefore, a comparison between simulation and measurement is straightforward.

Figure B.1 compares the single ion peak area distributions obtained from different signal integration measurements with simulation results. Note that this simulation works in a very simple way. There are no considerations about the actual peak shapes, nor pile-up of ion peaks included in the simulation. Yet, it delivers qualitatively good results.

Experimentally measured distributions are compared to simulations with similar numbers of ions per shot (not per trigger event, see explanation in 4.1.3). Table B.1 shows the estimated number of ions per shot for each sub-plot in figure B.1.

Table B.1: *Average number of ions per shot for measurement data shown in figure B.1 and selected average number of ions for the respective simulations. For loading times of* 300 µs *and* 500 µs*, the ion numbers could only be estimated because the measurement is distorted with pile-up for these loading times.*

Loading Time [μs]	**Exp.: Avg. #ions / shot**	**Sim.: Avg. #ions / shot**
10	0.76	1
30	2.68	3
50	4.66	5
100	8.79	10
300	29.17 (estimated)	30
500	48.62 (estimated)	50

All in all, the simulation shows that the single ion measurement and signal integration method deliver consistent results. The reason why they agree can be found in the **central limit theorem**. It can be assumed that different ions result in different peak areas on the MagneToF *independently* of each other and in the simulation, the peak areas are independent random variables by definition. Therefore, the central limit theorem can be applied to the distribution of the peak area.

In the signal integration method, higher loading times correspond to a higher number of samples. The central limit theorem states that for an increasing number of samples, the distribution of the distribution of the peak area can be approximated by a Gaussian. This is why the peak area histograms begin to look more symmetric for higher numbers of ions.

Figure B.2 shows the mean peak area per ion obtained from measurements with different loading time. The blue plot has already been shown in figure 4.11 and the red plot is the result of the simulation. As already mentioned above, the simulation does not consider pile-up events, and hence the simulated mean peak areas stay constant while the experimentally obtained values increase for a loading time of more than 100 µs.

A weakness of the simulation is its input data. As the peak area distribution for single ion measurements shown in figure 4.5 has high uncertainties, the simulation has high uncertainties as well because it uses this distribution. This is why the error bars on the simulation in figure B.2 are so big.

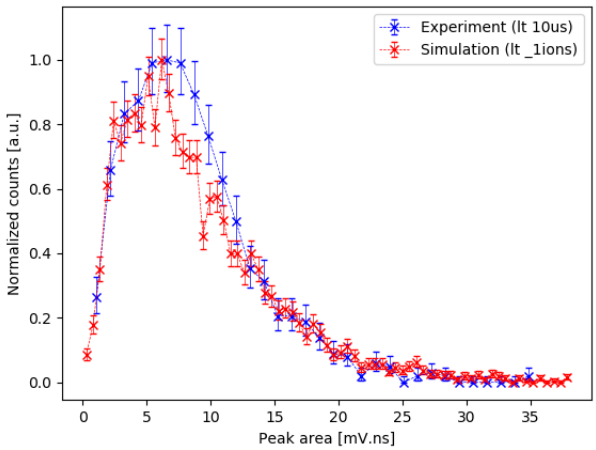

(a) approx. 1 ion per shot, loading time 10µs

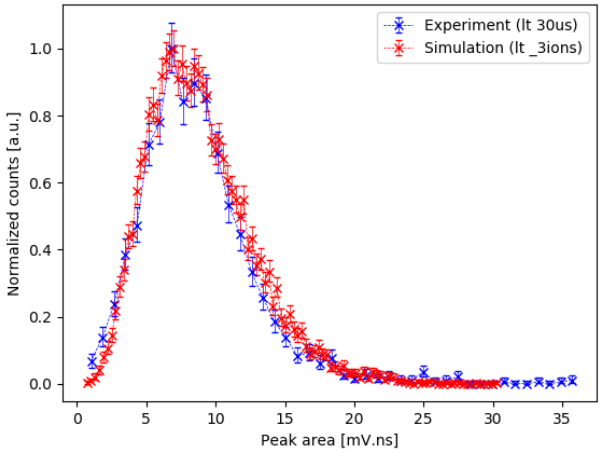

(b) approx. 3 ions per shot, loading time 30 µs

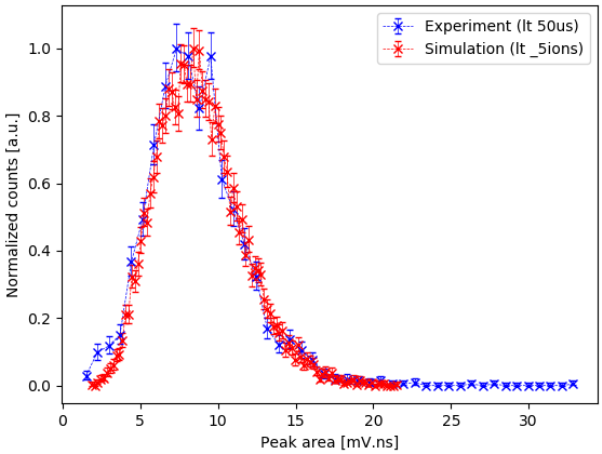

(c) approx. 5 ions per shot, loading time 50 µs

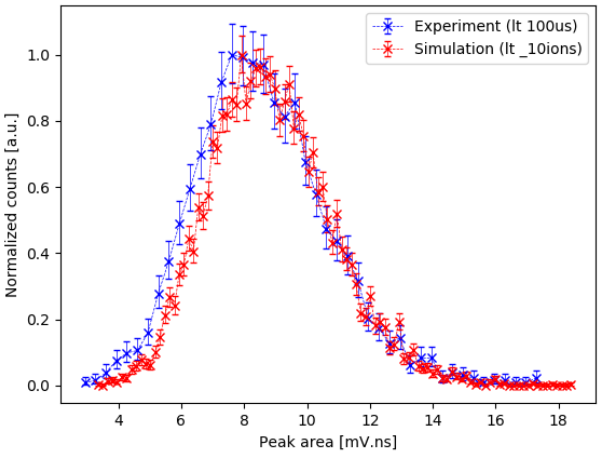

(d) approx. 10 ions per shot, loading time 100 µs

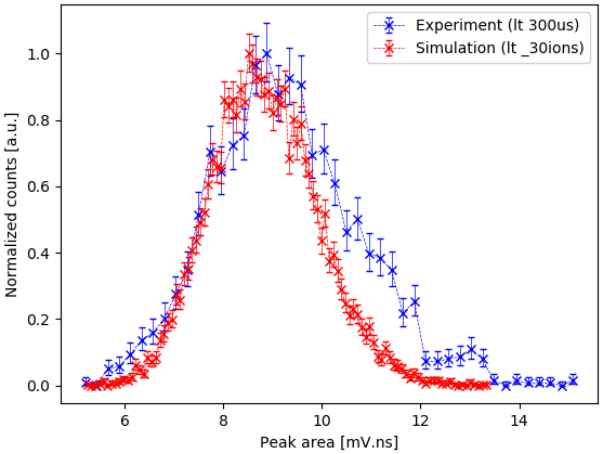

(e) approx. 30 ions per shot, loading time 300 µs

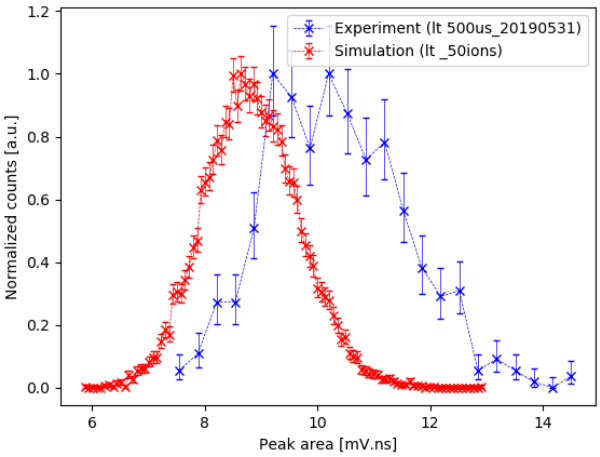

(f) approx. 50 ions per shot, loading time 500 µs

Figure B.1: *Peak area distributions for multi ion measurement simulation and experiment with the first MagneToF. As pile-up is not considered in the simulations, the distributions for experiment and simulations disagree for more than 10 ions per shot.*

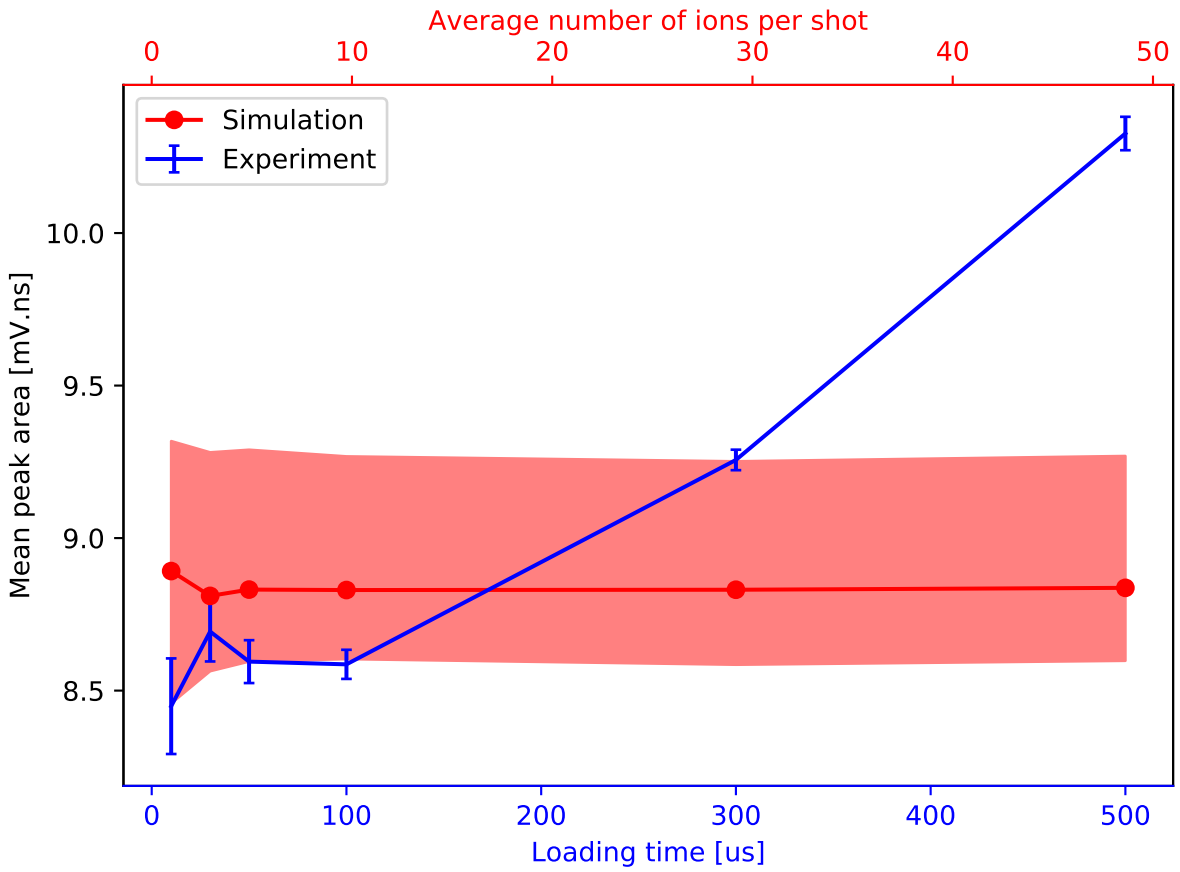

Figure B.2: *Mean peak area of a single ion for simulation and experimental data. These values are the means of the histograms shown in figure B.1. Please note that the conversation factor between numbers of ions and loading time is chosen so that the simulation matches with this experimental data. The same factor can not be applied to other measurements.*

B.2 Investigation of Non-Linearities: Steering the Ion Beam

To determine which part of the setup causes the kink in the first loading time scans in figure 4.14, the ion beam is steered at two different parts in the setup. Steering means that the beam is deflected away from its ideal direction, decreasing its intensity. Therefore, it is an alternative way to change the ion number without changing the Paul trap parameters. To disentangle the effects on the number of ions on the detector, two different measurements were performed:

- Figure B.3 shows loading time scans with different steering before the injection of the Paul trap. For the same loading time, different numbers of ions are injected into the Paul trap in different scans.
- Figure B.4 shows the results of loading time scans with different levels of steering before the MagneToF detector. Hence, for the same loading time, the same numbers of ions are injected into the Paul trap but different numbers of ions reach the MagneToF. The steering into the Paul trap is again set to its optimal value that has already been used in figure 4.14.

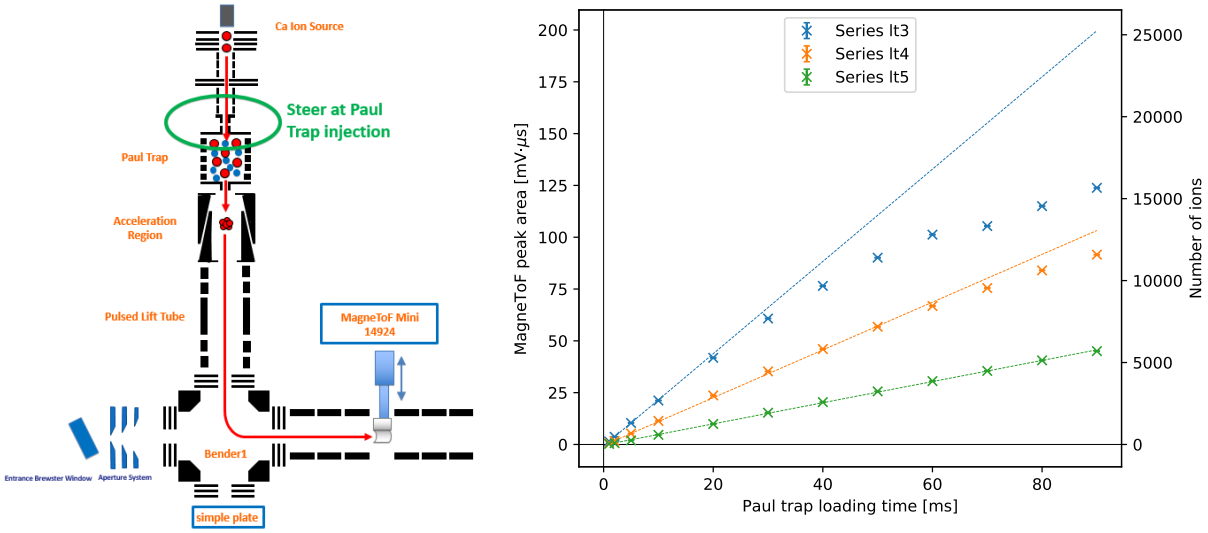

(a) Setup outline. Figure adapted from [29].

(b) Loading time scan results.

Figure B.3: *Result of loading time scans with steering the ion beam away from the Paul trap injection. The series "lt3" has been done without steering, for "lt4" slight steering has been applied and the scan "lt5" has been recorded with the strongest level of steering. Dashed lines are linear fits of the first 3 data points.*

In figure B.3, one can see that the kink vanishes when less ions are injected into the Paul trap, while changing the ion beam intensity on the MagneToF detector as shown in figure B.4 does not influence the kink. This could mean that the kink in figure 4.14 is linked to the number of ions in the Paul trap, rather than the number of ions impinging on the MagneToF detector.

A potential problem when performing these measurements is that steering is a very sensitive process and it is difficult to find a steering voltage that deflects the ion beam far enough so

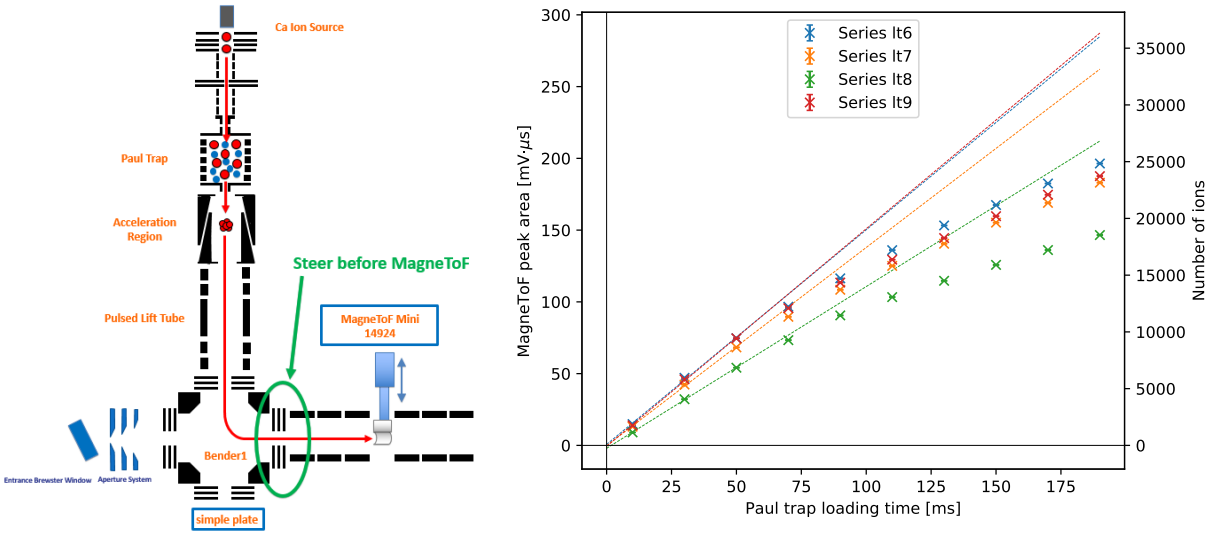

(a) *Setup outline. Figure adapted from [29].*

(b) *Loading time scan results*

Figure B.4: *Result of loading time scans with steering the ion beam right before the MagneToF detector. The series "lt6" and "lt9" have been done without steering, for "lt7" slight steering has been applied and the scan "lt8" has been recorded with the strongest level of steering. Dashed lines are linear fits of the first 3 data points.*

that there are significantly less ions, but on the other hand not too few ions.

Therefore, it was difficult to find appropriate levels of steering for the measurements presented above. While in figure B.3 there are around 3 times more ions in the measurement series without steering than in the measurement series with steering, the difference in ion number in figure B.4 between the measurement series is not more than 25 %. This makes the results by far less meaningful, as the ion numbers between the measurement series with different levels of steering are not comparable. To obtain significant results, the measurements presented above have to be repeated carefully and potentially also with more data points.

Appendix C

MagneToF Procedures

This appendix is a collection of step-by-step instructions for characterization and measurements with the MagneToF detectors.

C.1 Characterization of a New MagneToF Detector

This section explains how to characterize a new MagneToF sensor. From time to time, this procedure should be repeated in order to compensate for ageing effects.

Find the correct operation voltage

1. Choose a threshold level for the trigger

2. Choose a Paul trap loading time that allows single ion counting. Check the MagneToF signal on the scope.

3. Scan different operation voltages and count the number of shots per time window. Refer to the data sheet of the detector for a suitable operation voltage range.

4. Plot the results with the count ate on the y axis and the operation voltage on the x axis. Choose the operation voltage right above the knee of the curve.

Measure the mean peak area per ion

For the measurement process that we used, refer to the lablog entry Recording multi ion shots at 5GS/s.

For the evaluation, see 20190617 Final result: Peak area of one ion.

This procedure uses a PicoScope 6402D oscilloscope.

1. Attach the MagneToF to CH A of the PicoScope, the switching signal of the Paul trap is attached to the EXT trigger of the PicoScope. Set the trigger to EXT.

2. Switch off all Channels except for CH A, make sure that the sampling rate is 5GS/s (displayed on the right side of the screen). Make sure that interpolation is switched off.

3. Set a loading time that allows you to see big ion bunches (i.e. 10-50 ms loading time) and set the delay between trigger event and recording time frame so that you catch the center of the bunch.

4. Time settings of the PicoScope approx. 50 ns/div, voltage resolution **has to be the lowest possible** (i.e. 50 mV/div on the PicoScope 6402D).

5. Cross check that you do not count ions when the Paul trap is switched off or when the valves in front of the MagneToF are closed.

6. Record 2 000 shots each for different loading times that allow single ion counting. In our first measurements, this was in a range up to 100 µs. As a cross check, also take at least one measurement with higher loading times.

7. Analyze the result with the scripts in the MagneToF characterization project:
https://gitlab.cern.ch/MIRACLS/magnetof-characterization

- To calculate the signal area and count the number of ions for each shot, use the script `miAnalyzer.py`.
- To create a plot as shown in the evaluation example, use the script `miPlot.py` on the newly generated files.
- From the plot, choose all data points where pile-up is not yet present (i.e. all data points that have about the same mean peak area per ion).
- Calculate the weighted average of these data points. That is the mean peak area per ion.

C.2 Measuring the Number of Ions in an Ion Bunch

This procedure describes how the MagneToF detector – once it is characterized – can be used to measure the ion number of an ion bunch.

Preconditions

1. Make sure you have Python installed on your computer
2. Clone the **MagneToF Characterization** Git Repository:
https://gitlab.cern.ch/MIRACLS/magnetof-characterization
or alternatively, just download the script `nIonsInteractive.py`:
https://gitlab.cern.ch/MIRACLS/magnetof-characterization/blob/master/nIonsInteractive.py

Get the number of ions from a measurement

1. Save the PicoScope measurement result as CSV files:
2. Copy the folder with the CSV files to your local computer
3. **Before** running the script `nIonsInteractive.py`, adjust the following variables in lines 50 and below. This is just for the output, the program will ask you for the CSV files when you run it.

```
46  # ------------------------------------------------------------
47  #  ADJUST THESE SETTINGS BEFORE RUNNING
48  # ------------------------------------------------------------
49  ##############################################################
50  date = '20190717'
51  voltage = 850
52  loading_time = 25
53  det = detector_properties[('14924', 'CRIS', 'Mg')]
54  rev = 124
55  collisional = False
56  ##############################################################
```

The number of ions calculated after running the script will be saved with these attributes attached to them. It you are not planning to save the calculation result, you can leave these values unchanged. The meaning of these variables are:

- **Date:** Date of the measurement.
- **Voltage:** lift 2 voltage.
- **Loading_time** in μs.
- **Det:** detector used in your measurement.
- **Rev:** Number of revolutions that the ions have been trapped in the MR-ToF. If you did not trap the ions or the measurement has been done before the MR-ToF, set this variable to 0.

- **Collisional:** `True` if the measurement has been done during a collisional excitation run, `False` otherwise.

4. The detector properties are defined in lines 30 and below. If you add a new detector or re-characterize an old one, add it here:

```
30  # ------------------------------------------------------------------------
31  #  MagneToF detector settings
32  # ------------------------------------------------------------------------
33  detector_properties = {
34      ('14924', 'MIRACLS', 'Mg'): {'posid': 1, 'area': ufloat(8.80078694263287, 0.03594060527482725), 'label': 'First MagneToF'},
35      ('14924', 'CRIS', 'Mg'): {'posid': 2, 'area': ufloat(7.876935165226389, 0.04908501962218994), 'label': 'Second MagneToF'}
36  }
```

5. Run the script

6. A folder selection dialog opens. Select the folder with your measurements:

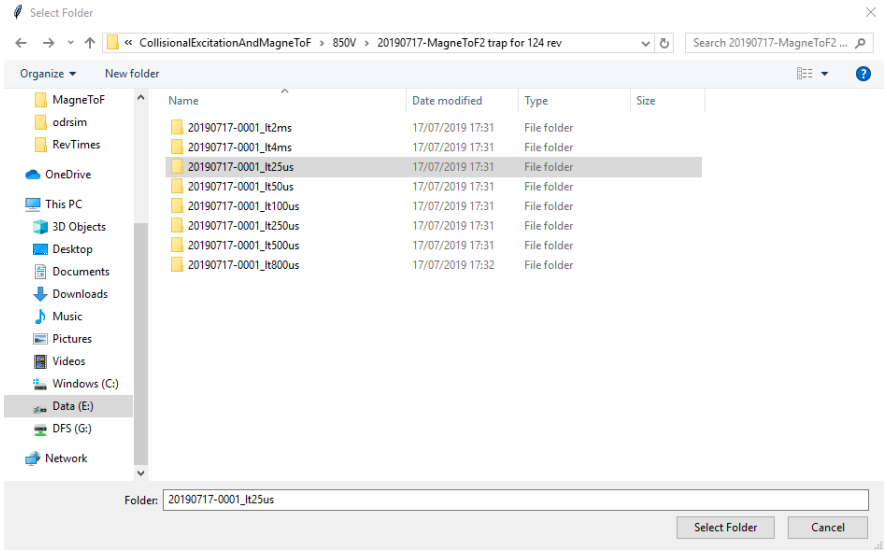

7. You will see a plot of the number of ions for each measurement in the folder (i.e. each CSV file). The red lines are the weighted arithmetic mean and its standard deviation, the green lines are the unweighted arithmetic mean and its standard deviations. To proceed, just close this window:

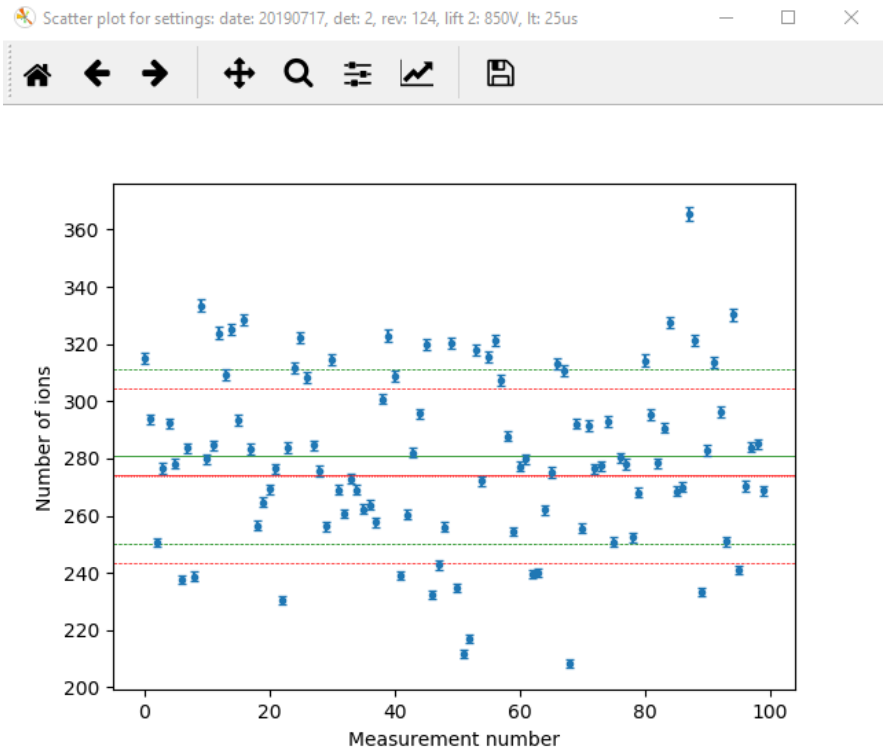

8. A dialog with the calculated ion number and the settings that you chose in step (3) appears. The ion number displayed here is the weighted mean:

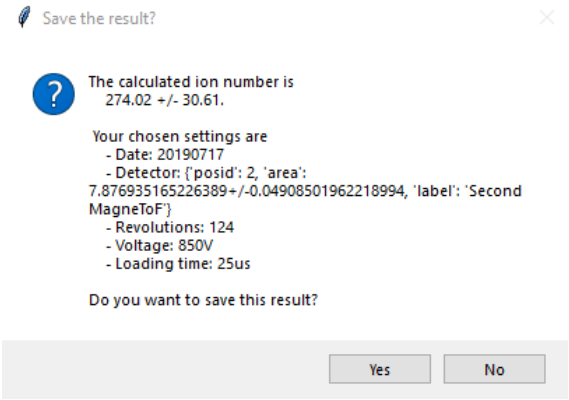

If you click yes, the ion number will be prepended to the output file, which is defined in line 42:

```
42  # Result file
43  ion_count_result_file = 'e:\\ion_count_results.csv'
```

9. The output file is a table with all ion numbers that you have evaluated with this program. This should make it easy to plot the result. For each measurement, the weighed arithmetic mean and the unweighted arithmetic mean with their respective sigmas are saved.

Appendix D

Second Collisional Excitation Campaign

This appendix provides an overview of all individual measurements done in the second campaign. Table D.1 shows a list of dates, file numbers and operation parameters. Measurements with lower loading times have been repeated more often in order to collect sufficient statistics.

In a collisional excitation measurement, a small amount of residual gas is leaked into the MR-ToF device, which increases the possibility of collisions between ions and residual gas. The fluorescence light emitted after a collision is used to characterize the ion bunch dynamics inside of the MR-ToF device, as described in section 3.3 and chapter 6. As the residual gas also increases the loss of stored ions, only low gas pressures can be used and the number of fluorescence photons detected from one ion bunch is very low. Typically, one measurement run lasts for 24 hours and ion bunches are repeatedly injected into the setup. The photon counts are added up in time bins representing different times of flight (since ejection from the Paul trap). Measurement runs with the same numbers of ions injected into the MR-ToF device can be combined together in order to collect more statistics. Data consisting of multiple measurements has a better signal-to-noise ratio than each data set evaluated separately.

D.1 Ion Numbers in Collisional Excitation Measurements

Before leaking nitrogen into the MR-ToF device (which is the buffer gas used for the collisional excitation), the number of ions at different positions in the setup has been measured:

- The number of ions injected into the MR-ToF apparatus has been measured with the first MagneToF.
- The number of ions passing through the MR-ToF device *without trapping* has been measured with the second MagneToF.
- The number of ions ejected from the MR-ToF device after *trapping for 124 revolutions* has been measured with the second MagneToF as well.

Table D.1: *Collisional excitation measurement runs of the second measurement campaign in July 2019.*

Date	In-trap lift voltage [V]	Loading time [µs]	File number
2019-07-10	850	25, 50, 100, 250, 800	file004
2019-07-11	850	25, 50, 100, 250, 800	file007
2019-07-12	850	25, 50, 100, 250, 800	file008
2019-07-12	850	4000	file009
2019-07-12	700	25, 50, 100, 250, 800	file108
2019-07-13	700	25, 50, 100, 250, 800	file111
2019-07-14	700	25, 50, 100, 250, 800	file112
2019-07-15	700	4000	file113
2019-07-17	850	100, 250, 800, 2000, 4000	file096

During the collisional excitation runs, only the second MagneToF detector was used to monitor the ions coming out of the MR-ToF device. The first MagneToF could not be used as it would block the beam from going into the MR-ToF apparatus.

Figure D.1 shows the number of ions measured during the collisional excitation measurements with an in-trap lift voltage of 850 V. One can see that the numbers of ions are almost the same for all measurements. This means that the individual measurements done between 10^{th} and 12^{th} July can be combined in order to gain higher statistics. The measurement from 17^{th} July (file096) can however not be combined with these earlier measurements, as some of the settings have been changed between these runs. However, the runs from 17^{th} July have been done done with higher loading times so that it was possible to collect enough statistics anyway.

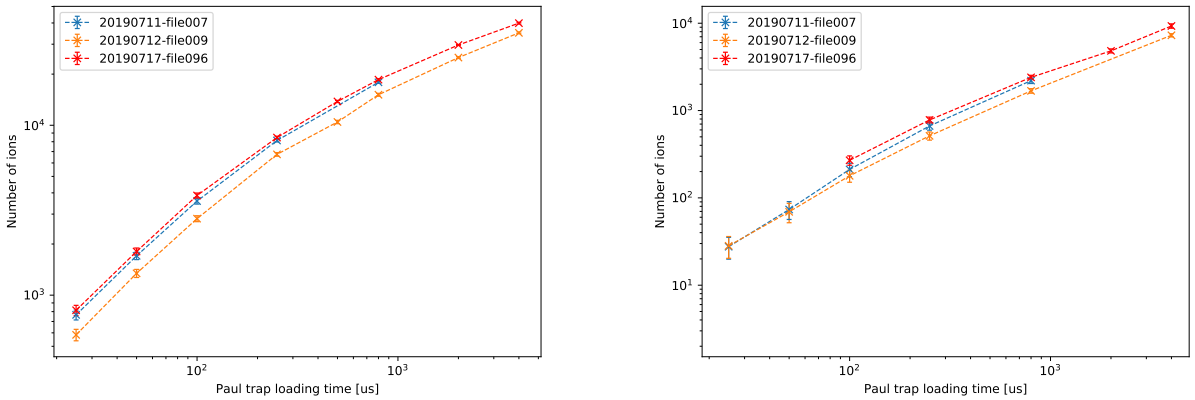

(a) *Injection into the MR-ToF device* ***(b)*** *Ions ejected after collisional excitation*

Figure D.1: *Number of ions injected into the MR-ToF device and ejected from the MR-ToF device during collisional excitation measurements of the second campaign with an in-trap lift voltage of* 850 V.

For an in-trap lift voltage of 700 V on the other hand, there have been significant drifts in the MR-ToF operation during the measurements. Figure D.2 shows that the number of ions ejected from the MR-ToF apparatus changed significantly between the individual

measurement runs while the number of ions injected into the MR-ToF apparatus stayed constant. Combining the data from these different runs leads to results worse than each individual data set because of the different operation parameters. As it is unknown what happened in the MR-ToF device during the later measurements, only the first one (file108 from 2019-07-12) will be used in further evaluations.

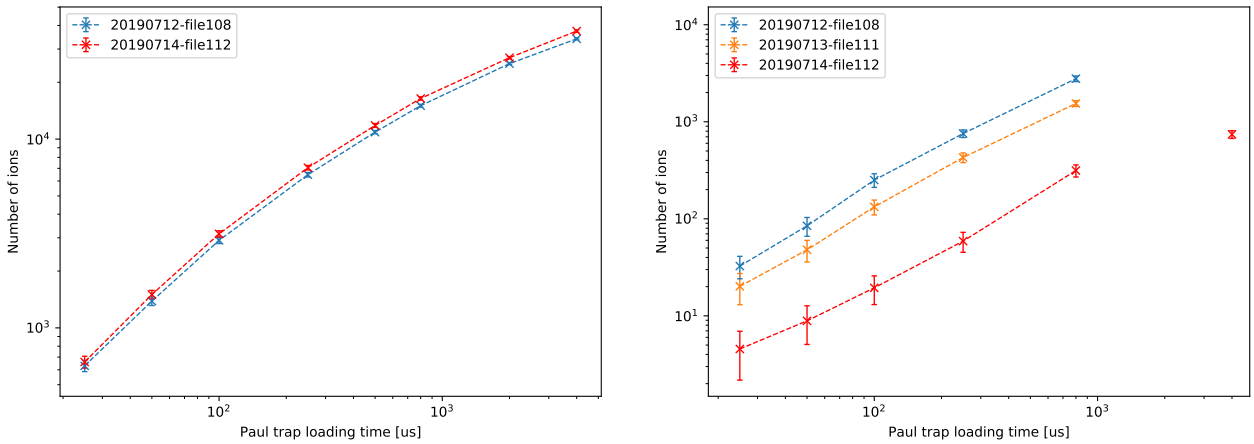

(a) Injection into the MR-ToF device

(b) Ions ejected after collisional excitation

Figure D.2: *Number of ions injected into the MR-ToF device and ejected from the MR-ToF device during collisional excitation measurements of the second campaign with an in-trap lift voltage of* 700 V.

D.2 Trapping Efficiency of the MR-ToF Device

From the numbers of ions determined before each collisional excitation measurement, the transmission efficiency and the trapping efficiency of the MR-ToF apparatus have been calculated for the particular settings used.

- The **transmission efficiency** is the number of ions passing through the MR-ToF apparatus without trapping divided by the number of ions injected into the MR-ToF device.
- The **trapping efficiency** is the number of ions ejected after trapping divided by the number of ions injected into the MR-ToF apparatus. Of course, the trapping efficiency depends on the number of revolutions that the ion bunch is travelling in the trap.

Figure D.3 shows the transmission and trapping efficiencies for both of the in-trap lift voltages that have been used in the second collisional excitation campaign. The transmission efficiencies seem to depend on the Paul trap loading time (and thus on the number of ions injected) and are between 60 % and 90 % for both in-trap lift voltages. These values are relatively consistent for all measurements.

For an in-trap lift voltage of 850 V, the trapping efficiencies have been between 40 % and 60 % and are consistent for both data sets that have been taken.

However, for an in-trap lift voltage of 700 V, the trapping efficiencies ave been different for each measurement. In figure D.3b one can see that on 12$^{\text{th}}$ July, a trapping efficiency

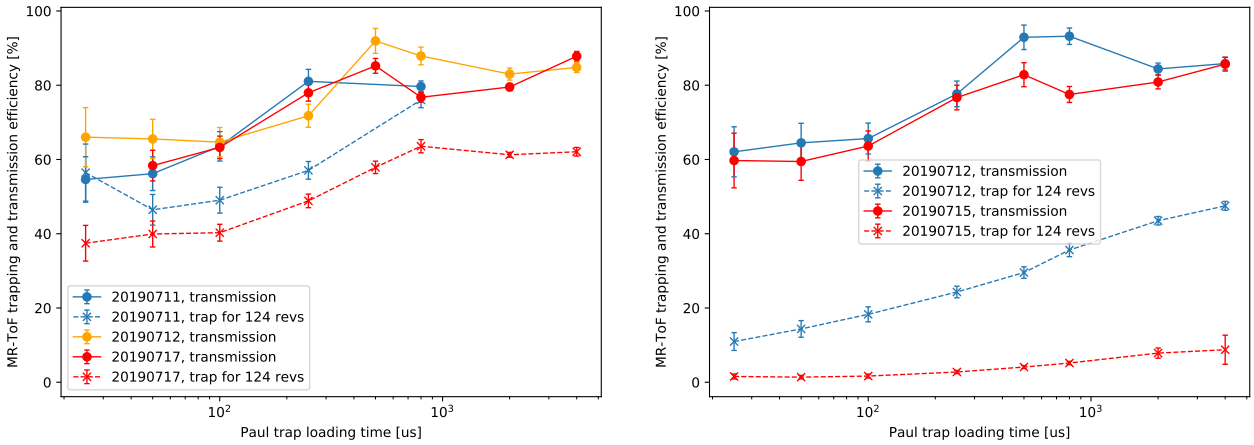

(a) *In-trap lift* = 850 V

(b) *In-trap lift* = 700 V

Figure D.3: *Transmission efficiency (solid line) and trapping efficiency (dashed line) of the MR-ToF device without buffer gas. The trapping efficiency has been measured for 124 revolutions in the MR-ToF device.*

between 10 % and 40 % has been measured while in a later measurement on 15$^{\text{th}}$ July, the trapping efficiency has almost fallen down to 0 %. This indicates again that there have been unexplained changes in the MR-ToF operation during the later measurements with an in-trap lift voltage of 700 V.

Appendix E

Additional Information on the Ray Tracer

This appendix supplies additional information on the ray tracing program which has been used to characterize the optical detection region.

E.1 Other Applications of the Ray Tracer

Apart from calculating the axial position dependent detection efficiency of the ODR, which is used for the simulations described in chapter 5, there are two more uses of the ray tracer at MIRACLS.

E.1.1 Finding the Optimal Distance Between PMT and Lens 2

The original use of this project was to calculate the optimal distance between the focusing optics and the PMT, depending on the wavelength used. It is hard to completely automate this process as it requires understanding of how the focusing works in order to choose the correct distance.

During the work on this thesis, a step-by-step manual for this process has been created so that any user can do it without much background knowledge. The procedure is designed to find the best signal to noise ratio, not the highest signal efficiency.

Downloading and Running the Script

This procedure has been created for version 1.0.1 of the optical detection region simulation. The source code can be found in
https://gitlab.cern.ch/MIRACLS/pmt-detection-region-simulation/-/tags/v1.0.1.

Open the file `optimal_distance_interactive.py`. Here, you can enter the wavelength in nm and the desired material of the lenses:

```
15
16  wavelength = 280
17
18  result = raytracer(wavelength=wavelength, material="corning7960", positions=pos, rays=10000, laserbeamsize=0)
19  ray_pmt_to_lens = PlotRaytracer(result, spacerthickness=150, pmt_diameter=2 * 26.275, mask_diameter=2 * 26.275)
20  ray_pmt_to_lens.plot(mask_photons=False, hexbin_radius=40, mark_positions=pos, slider_bounds=20)
```

Figure E.1: *First lines of the file* `optimal_distance_interactive.py`.

Finding the Optimal Spacer Distance

When you run the script, a window with some graphs appears:

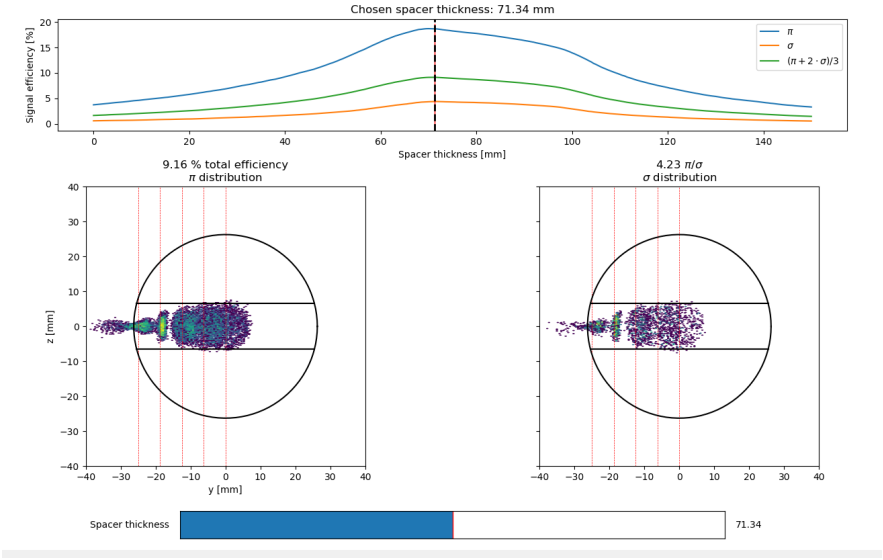

Figure E.2: *Overview of the GUI to find the optimal spacer distance. The spacer distance can be adjusted with the blue progress bar.*

The upper plot shows the signal efficiency. The distance for maximum efficiency is highlighted. However, this is not the optimal distance, as mentioned above. To find the optimal distance, change the slider at the bottom and optimize the two graphs in the middle according to the following criteria:

1. Focus point should be a little bit inside of the PMT.
2. Central spot should not be clipped. There should be a little distance between the spot and the slit.

E.1.2 Aperture in Front of Lens 1

An approach to reduce laser stray light in the detection region might be to add an aperture in front of lens 1. Such an aperture had been designed based on simple geometrical considerations and had already been installed in 2018. Design drawings of this aperture can be seen in figure E.4.

With the new knowledge that the ray tracing project made accessible, it has been investigated whether this aperture could be designed smaller without loosing signal photons emitted by the ions.

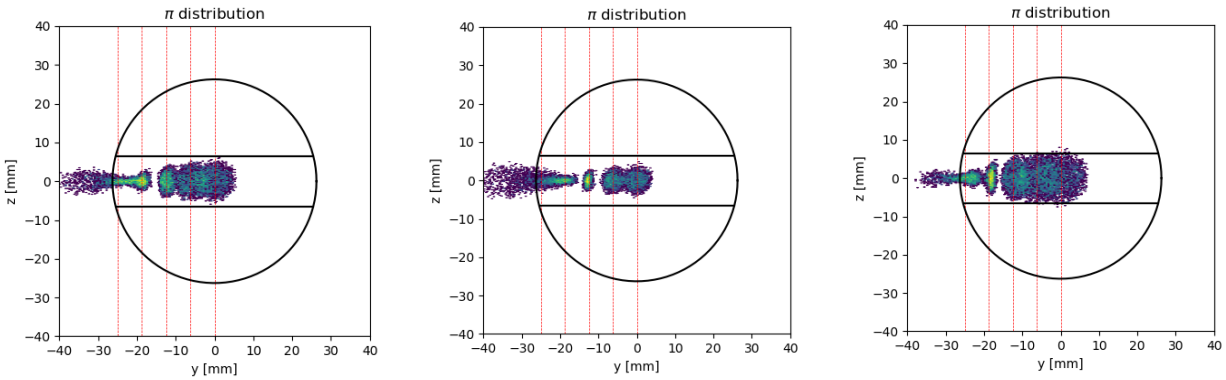

(a) Correct

(b) Wrong: Focus too far inside, central spot too focused

(c) Wrong: Focus on edge of PMT, central spot touching the slit

Figure E.3: *Correct and wrong settings for the spacer distance*

For this task, the ray tracer has been modified so that photons that actually hit the PMT can be tracked *back* from the PMT to the aperture plane. With these changes, it was possible to design a new aperture with only half the opening area and without significant efficiency losses. The aperture has been designed for a wavelength (see section 3.2) of 280 nm (magnesium), but it also works without significant losses for a wavelength of 397 mn (calcium). The calculation results can be seen in table E.1 and figure E.5.

Whether a reduction of the aperture opening area by a factor of 2, also leads to a reduction of the stray light background by a factor of 2 is difficult to estimate. The way that stray light gets into the setup and is scattered or reflected on surfaces is not straightforward. It therefore remains for future work to investigate the improvement with such a new aperture experimentally.

Table E.1: *Properties of the installed (old) and the newly designed aperture. The detection efficiencies shown here are the average of different positions on the ion beam axis and are therefore not directly comparable to values in figure 5.5. The chosen distance between lens 2 and PMT is not necessarily the ideal distance, as the minimal distance is* 81.8 mm *for mechanical design reasons.*

	Current aperture	**New aperture**
Length (y)	100.2 mm	60 mm
Width (z)	55 mm	45 mm
Area	5511 mm^2	2700 mm^2
Detection efficiency ($\lambda = 280$ nm)	4.666 % ± 0.024 %	4.664 % ± 0.024 %
Distance PMT – Lens 2: 81.8 mm		
Detection efficiency ($\lambda = 397$ nm)	4.519 % ± 0.024 %	4.495 % ± 0.024 %
Distance PMT – Lens 2: 83 mm		

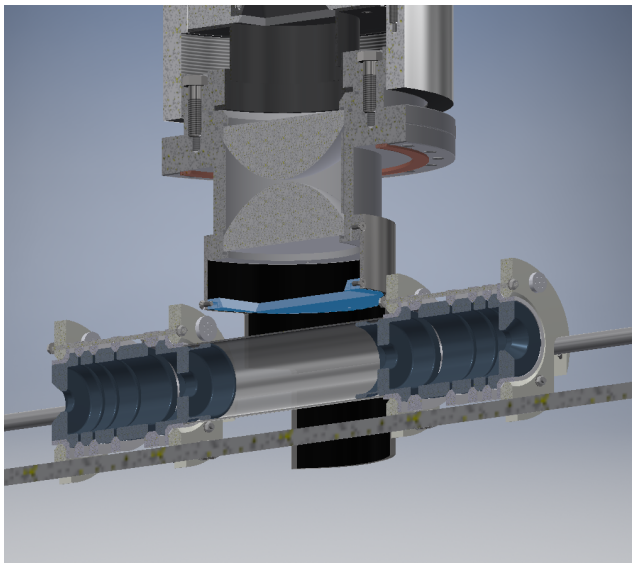

(a) Overview of the optical detection region. The additional aperture is highlighted in blue.

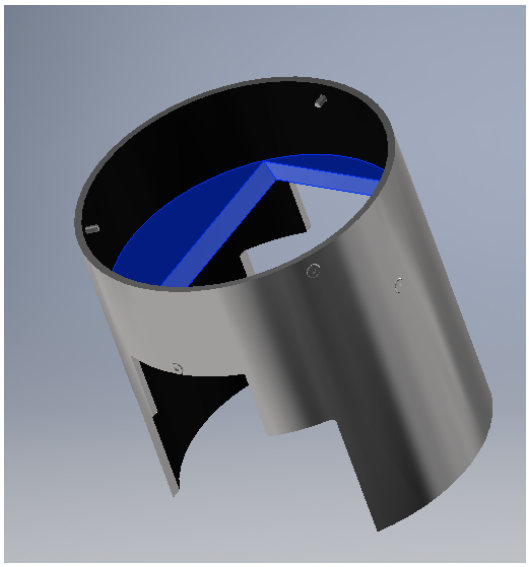

(b) Detailed view of the stray light shield with the aperture.

Figure E.4: *Construction drawings of the additional aperture and its installation in the optical detection region of MIRACLS' PoP setup.*

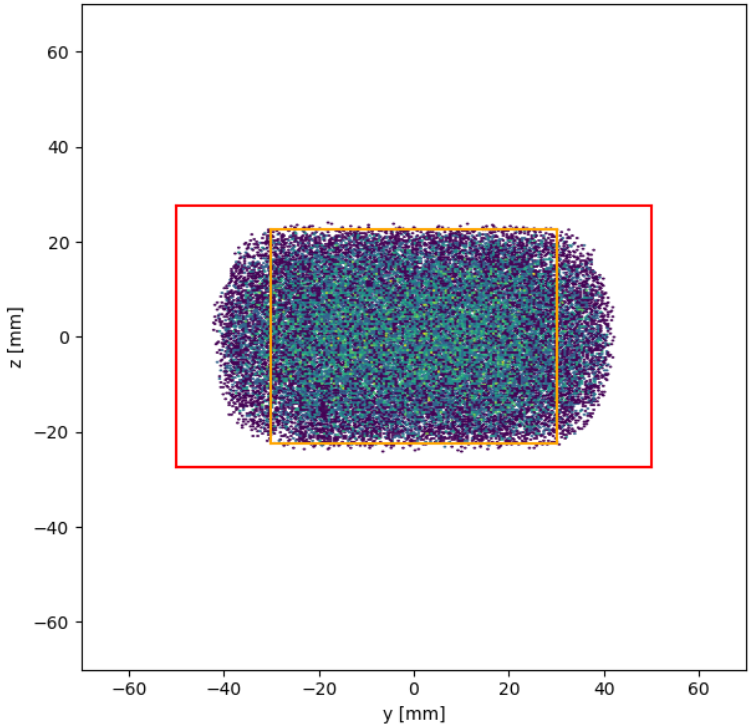

Figure E.5: *Plot of the aperture plane only with photons that will actually reach the PMT. Brighter colors means more photons. Please note that the scaling is logarithmic: there are far more photons in the center than on the edges. The currently installed (old) aperture is drawn in red, the new aperture is drawn in orange.*

E.2 Emission Patterns

The radiation emitted by the an atomic dipole can be non-isotropic. The emission pattern depends on the value of Δm_F of the transition in question. For $\Delta m_F = 0$ and $\Delta m_F = \pm 1$, the emission patterns are [43]

$$\begin{array}{lll} \Delta m_F = 0 & I(\theta) = \sin^2(\theta) & \text{also called } \pi\text{-emission, donut} \\ \Delta m_F = \pm 1 & I(\theta) = 1 + \cos^2(\theta) & \text{also called } \sigma\text{-emission, dumbbell} \end{array}$$

Figure E.6 shows a simulation of π and σ emission patterns as they would appear in the plane of the additional aperture that is described in section E.1.2.

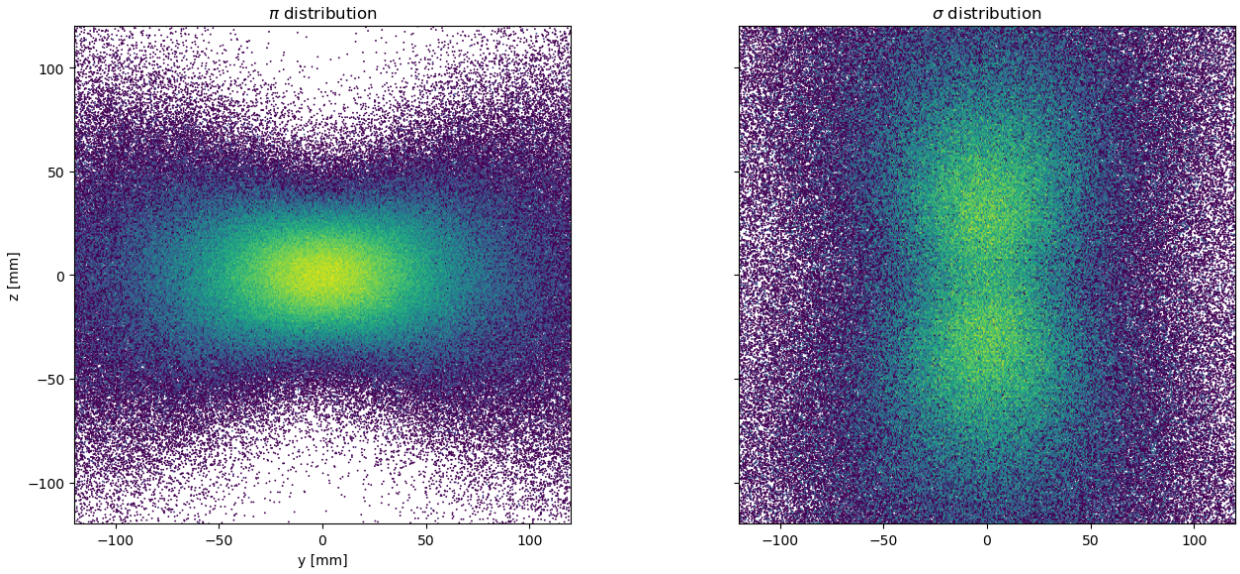

Figure E.6: *Simulation of photons impinging on the plane of the aperture in front of lens 1 (see section E.1.2). The direction of the emitted photons is distributed according to π and σ emission patterns. Details see text.*

In a laser spectroscopy measurement, the emission pattern has to be considered. If the atoms are excited by a polarized laser beam, the dipoles that emit the photons will align to the polarization of the laser beam (see also the document in section E.3). Depending on the transitions that can take place, the emission pattern can be non-isotropic in this case. On the other hand, atoms or ions that are excited by collisions with other particles will always emit isotropic light because they are not arranged in a preferred direction.

Therefore, pi and sigma emission are an important part of the ray tracer. While these different patterns are considered when calculating the optimal distance between PMT and the focusing optics (which is mostly used for laser spectroscopy), an isotropic distribution has been used to calculate the detection efficiency profile (which will simulate collisional excitation measurements) and to improve the aperture in front of lens 1.

E.3 Documentation of the COLLAPS Ray Tracer

This is the software documentation and description of the original ray tracing program written by Wouter Gins for COLLAPS and VITO.

Ray tracing simulations for optical detection region at COLLAPS and VITO

Wouter Gins

October 24, 2018

In the optical setup at both COLLAPS and VITO, fluorescent decay from the excited ionic or atomic beam is detected with PMT's. In order to maximize the detection efficiency, a set of lenses is used to focus the emitted light onto the surface of the PMT's. As the index of refraction of the material of the lenses is wavelength dependent, the optimal point to place the PMT needs to be recalculated each time. The propagation of light through the optical setup is calculated via ray-tracing techniques and the steps taken in the calculation are described here.

1 Lens system

As the ion/atomic beam emits light from every location overlapping with the laser beam, the use of aspherical lenses minimizes the loss of detection efficiency from *spherical aberration*, where the focal point of the beam changes as the light enters the lens off-axis. The aspherical lenses in the VITO setup have been produced by Asphericon GmbH (product number A100-100LPX-S-U), are plano-convex lenses and have a diameter of 100 mm. The curved surface has been designed to have the form [1]

$$z(r) = C\frac{r^2}{1+\sqrt{1-(1+K)C^2}} + A_2 r^2 + A_4 r^4 + A_6 r^6 + \dots \tag{1}$$

where the z-axis is assumed to be the optical axis of the lens. $z(r)$ is the displacement along the z-axis from the surface point on the central axis as a function of distance r. Table 1 gives the parameters for the purchased lenses.

Two such aspherical lenses form the imaging system for each PMT. Figure 1 shows the CAD design of the imaging system. Indicated on this schematic drawing is the distance from the surface of the lens to the center of the beamline (76.2 mm), the aperture of the lenses (92 mm), the diameter of the PMT surface (47.5 mm) and the distance of the PMT to the flat edge of the second lens. This distance can be increased by using a mechanical spacer to maximize the optical detection efficiency. When the wavelength indicates a closer distance is needed, a different mounting system is required.

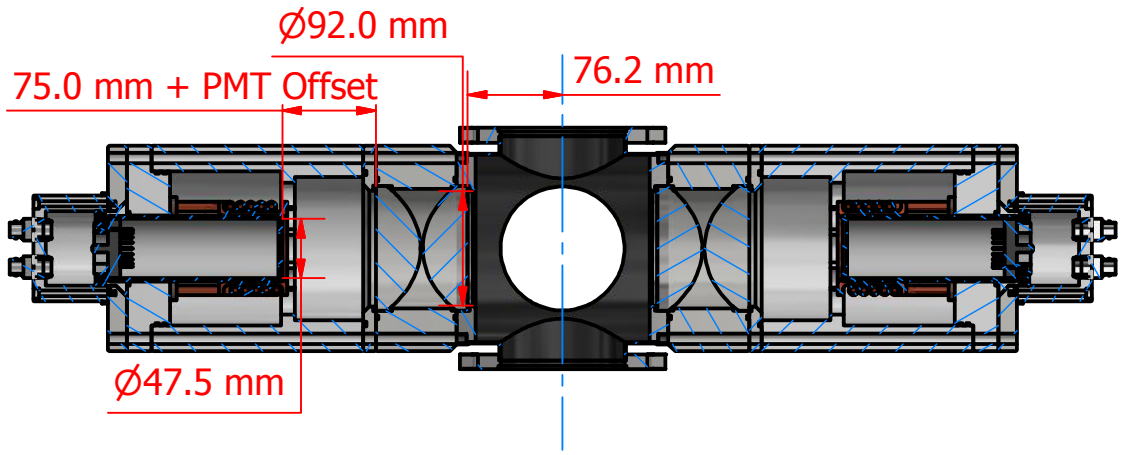

Figure 1: *Optical detection setup with cooled housing as modelled in Inventor. Relevant dimensions have been indicated. Note that the PMT Offset is the spacer thickness and 75 mm is the starting distance (defined further in the text).*

2 Index of refraction

The index of refraction for the lenses can be calculated from the Sellmeier equation or the Cauchy equation, empirical equations relating the wavelength and index of refraction for different glasses. The Sellmeier equation used is

$$n^2(\lambda) = A_0 + A_1\lambda^2 + A_2\lambda^{-2} + A_3\lambda^{-4} + A_4\lambda^{-6} + A_5\lambda^{-8}, \tag{2}$$

while the Cauchy equation is

$$n^2(\lambda) = 1 + \frac{B_1\lambda^2}{\lambda^2 - C_1} + \frac{B_2\lambda^2}{\lambda^2 - C_2} + \frac{B_3\lambda^2}{\lambda^2 - C_3} \tag{3}$$

For BK7 crown glass (also known under the name Schott glass or B270 glass), which is the material

Table 1: *Aspherical surface parameters*

Parameter	Value
C	0.016 767 270 288 4
K	−1.035 958 114 8
A_2	$1.287\,485\,311\,9 \times 10^{-3}\,\mathrm{mm}^{-2}$
A_4	$4.285\,329\,204\,317 \times 10^{-7}\,\mathrm{mm}^{-4}$
A_6	$2.660\,598\,011\,977 \times 10^{-11}\,\mathrm{mm}^{-6}$
A_8	$1.889\,503\,380\,77 \times 10^{-15}\,\mathrm{mm}^{-8}$
A_{10}	$9.063\,010\,624\,48 \times 10^{-21}\,\mathrm{mm}^{-10}$

of the ordered lenses, the Sellmeier equation has been used (see Table 2). For some other materials that can be used to construct lenses, the Cauchy coefficients are also tabulated.

3 Refraction of light

At the interface between two media with different refraction indices, the path of the light has to break according to Snell's law. Snell's law in 3D can be stated as [2]

$$c = -\hat{n} \cdot \hat{i}, \tag{4}$$

$$\hat{e} = \frac{n_1}{n_2}\hat{i} + \left(\frac{n_1}{n_2}c - \sqrt{1 - \left(\frac{n_1}{n_2}\right)^2 (1 - c^2)}\right)\hat{n}, \tag{5}$$

where $\hat{i}$ is the direction of the incident ray, $\hat{n}$ is the normal vector of the curved surface and n_1 and n_2 are the refraction indices of the first and second medium. As the incident ray direction is known and the Sellmeier equation can be used to calculate the refraction index, only the normal vector of the surface still needs to be calculated.

Instead of deriving the formulation of the normal vector analytically, it can also be approximated numerically. The normal vector is calculated by taking the lens surface at the incident point, and calculating the lens surface position when x and y (assuming z is the optical axis) are slightly varied. The vector product of the two vectors connecting the incident point with the two additional points results in the normal vector on the surface in the incident point.

4 Emission pattern

The decay from an excited state to a lower lying level, and subsequent generation of a photon, is described by the dipole operator. The emission pattern can be calculated from quantum mechanics [3, 4], yielding two different angular distributions:

$$I(\theta) \propto \sin^2(\theta) \tag{6}$$

$$I(\theta) \propto 1 + \cos^2(\theta) \tag{7}$$

Table 2: *Sellmeier and Cauchy equation parameters for different glasses.*

Sellmeier coefficients	B270	Cauchy coefficients	Lithosil	Corning 7960
A_0	2.287 782 8	B_1	$6.694\,226 \times 10^{-1}$	$6.852\,562\,45 \times 10^{-1}$
A_1	$-9.314\,872\,3 \times 10^{-3}\,\mu m^{-2}$	B_2	$4.345\,839 \times 10^{-1}$	$4.188\,670\,77 \times 10^{-1}$
A_2	$1.098\,644\,3 \times 10^{-2}\,\mu m^2$	B_3	$8.716\,947 \times 10^{-1}$	$5.111\,042\,39 \times 10^{-1}$
A_3	$4.846\,520\,3 \times 10^{-4}\,\mu m^4$	C_1	$4.480\,112 \times 10^{-3}\,\mu m^2$	$4.619\,907\,90 \times 10^{-3}\,\mu m^2$
A_4	$-3.394\,473\,8 \times 10^{-5}\,\mu m^6$	C_2	$1.328\,470 \times 10^{-2}\,\mu m^2$	$1.340\,584\,57 \times 10^{-2}\,\mu m^2$
A_5	$1.695\,855\,4 \times 10^{-6}\,\mu m^8$	C_3	$9.534\,148 \times 10^{1}\,\mu m^2$	$5.647\,696\,99 \times 10^{1}\,\mu m^2$

for decays with $\Delta m_F = 0$ and $\Delta m_F = \pm 1$ respectively. These waves are respectively the π and σ waves and are separately propagated through the optical setup.

As the distribution is $\sin^2(\theta)$ distributed and θ is the angle between the oscillation direction of the electrical field, it follows that no radiation is emitted along the oscillation path. Assuming that the oscillation path is vertical along the beamline, since the laser light is vertically polarized in the COLLAPS setup, the dipole emission pattern for π-waves indicates most light from the signal will be emitted in the horizontal plane. As the lenses are located perpendicular to the beam direction, the $\sin^2(\theta)$ distribution will have the largest impact on the signal.

The *hit-and-miss* algorithm is used to generate the initial directions for the rays. For each ray, a random direction vector $\vec{d} = (x, y, z)$ is generated within the cube $x, y, z \in [-3, 3]$. If the endpoint of this vector is within the boundary defined by the function $r(\theta) = \sin^2(\theta)$, the direction vector is accepted and normalized. Otherwise, another direction vector is randomly generated.

In the simulation code, only one set of lenses is simulated. The axis sytem assumed in building the setup is that the optical axis is the x-axis and the beamline axis is the y-axis. Therefore, x is restricted to $[0, 1.5]$ to select only the part of the cube that would point in the direction of x.

The emission pattern is combined with the position from which these rays are released. Several options are available in the ray tracer:

1. Specific positions are supplied to the ray tracer along with a number of rays. This will release this amount of rays from each of those specific y-positions, with $y = 0$ corresponding to the symmetry axis of the lens system.

2. When the option to use a distribution is used, the y-position is uniformly random distributed between the minimal and maximal position provided. The number of rays now indicates the total number of rays.

3. The size of the laser spot can also be used, and will distribute the starting x and z position uniformly over a circle with the given diameter. Setting this to 0 or lower will restrict the x and z coordinates to 0.

5 Simulation scripts and output

The python script *COLLAPS_raytracer.py* contains the simulation code for the optical setup as described here. A sequential ray tracer tracks the emitted rays to the next optical element and removes the rays that exit the yz-area corresponding to the aperture of the lenses. It generates a compressed .npz file containing the ray positions and directions of the signal and background rays when the rays have arrived at the flat edge of the second lens, along with the number of rays originally emitted. This script is used from the command line and understands the following arguments:

-**wavelength** Supply the wavelength of the light in nm (default: 811)

-**material** Supply the material of the lenses (b270, corning7960 or lithosil, default: b270)

-**positions** Supply the position offsets from which to release the rays, in mm (default: 0.0 5.0 10.0 15.0 20.0 25.0)

-rays Supply the number of rays to be released from each position (default: 10000)

-laserbeamsize Supply the diameter of the laser beam in mm (default: 5)

–distributed If True, N rays are released from a random released position between the minimum and maximum supplied instead of N rays from each position (default: False)

The script *plot_COLLAPS_raytracer_data.py* will process the data and propagate the rays onto the surface defined by the PMT as in Figure 1. Additionally, the PMT is assumed to be covered except for a horizontal slit. The detection efficiency is calculated by counting the number of rays that are incident on the PMT inside this slit. The script can be called with the following arguments:

filename Filename of the datafile

-startingdistance Distance between the second lens and the PMT without spacer in mm (default: 47)

-pmtsize PMT diameter in mm (default: 47.5)

-masksize Diameter inside which the ray distribution is drawn (default: 47.5)

-spacerthickness Maximal spacer thickness in mm (default: 100)

-slitsize Size of the slit in mm (default: 13)

–interactive If True, the interactive plots are shown before the PDF is saved (default: False)

Of these, only the filename is a required argument.

The resulting pattern of light on the plane will be drawn, along with the calculated light detection efficiency and the σ/π ratio, representing the difference in detection efficiency for the different emission patterns. The optimal spacer thickness for maximal signal efficiency is automatically calculated and set as initial thickness. When the interactive flag is given, a GUI is opened with all plots along with a slider for the spacer thickness. The initial value of the slider is the result of the optimizer. When this window is closed, the final value of the slider is used to generate the figures saved to the PDF. The calculated light distribution for a wavelength of 217 nm with a spacer thickness of 12.5 mm is shown in Figure 2.

Note that the signal efficiency is calculated as the amount of π-rays incident on the PMT divided by the number of π-rays originally released. As only rays propagating along the positive x-axis are generated, this efficiency is for the total system of 2 PMT's across from each other. The detection efficiency of a single PMT is half of this number. The ratio of detected π-rays to σ-rays is also calculated and displayed.

References

[1] Christof Pruss et al. "Testing Aspheres." In: *Opt. Photon. News* 19.4 (Apr. 2008), pp. 24–29. DOI: 10.1364/OPN.19.4.000024. URL: http://www.osa-opn.org/abstract.cfm?URI=opn-19-4-24 (cit. on p. 1).

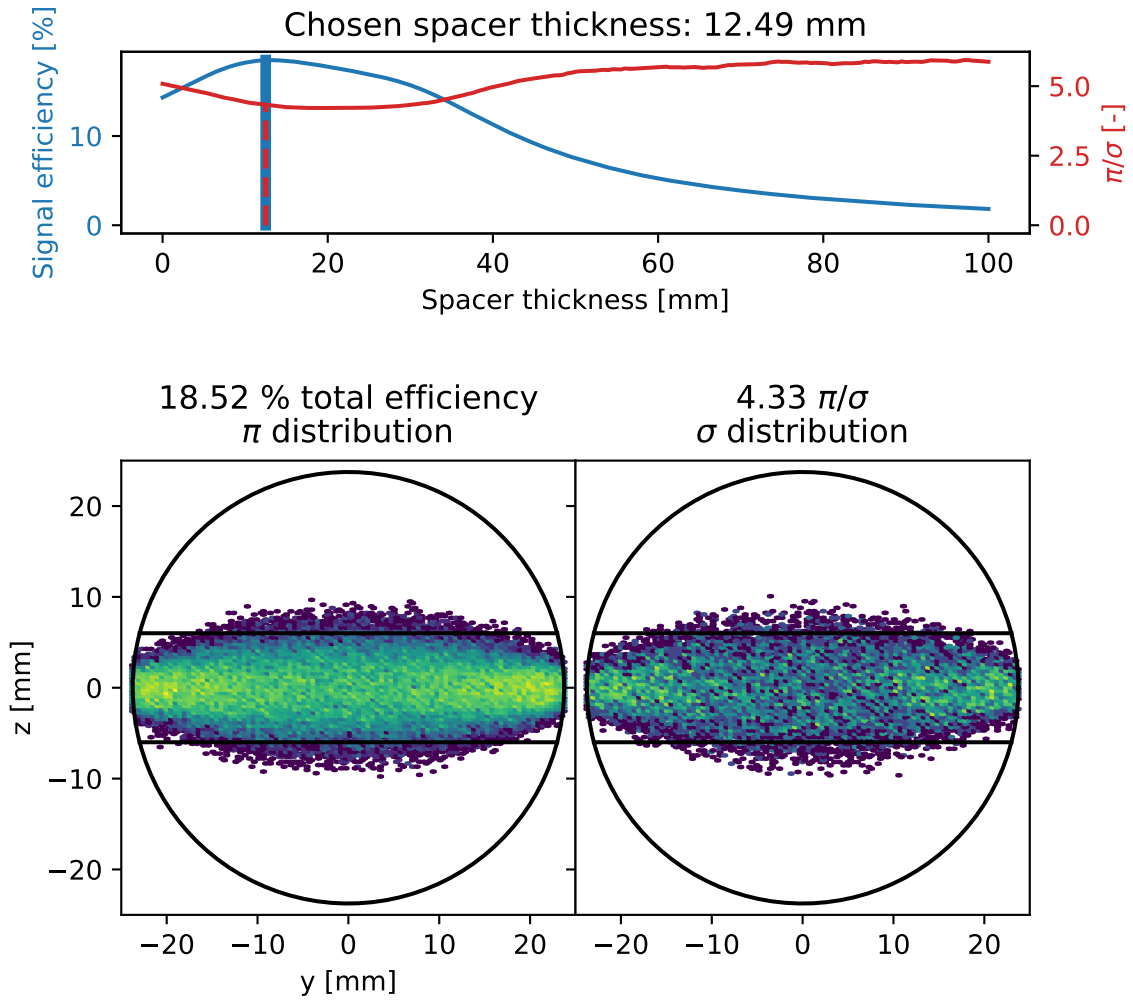

Figure 2: *Result of calculating the light propagation for 217 nm light through the setup with lenses made out of Corning 7960 glass.*

[2] Bram de Greve. *Reflections and Refractions in Ray Tracing*. 2006. URL: https://graphics.stanford.edu/courses/cs148-10-summer/docs/2006-degreve-reflection_refraction.pdf (cit. on p. 3).

[3] Ingolf Hertel. *Introduction to Quantum Physics*. 2002. URL: http://staff.mbi-berlin.de/hertel/physik3/chapter8/8.7html/01.htm#top (cit. on p. 3).

[4] L. J. Curtis. *Atomic Structure and Lifetimes*. 2002. URL: http://astro1.panet.utoledo.edu/~ljc/chapa6.html (cit. on p. 3).

Appendix F

Documentation of the Collisional Excitation Data Fitting Tool

To obtain peak parameters such as peak width and area from a collisional excitation measurement, the *Collisional Excitation Data Fitting Tool* has been created. This tool is tailored to fit data with frequently occurring peaks as obtained from collisional excitation, CLS measurements or simulation data. Yet the tool is versatile in the possible configurations and fit constraints.

In this appendix, you can find references and examples on how to use the *Collisional Excitation Data Fitting Tool*. This is not a complete list of all functions, for a full reference, also see the documented source code in the GitLab repository[1].

F.1 A Few Words on Lmfit

The *Collisional Excitation Data Fitting Tool* is a wrapper library for lmfit[2]. It provides functionality to fit data that has many peaks with almost constant peak distance (as it is the case for collisional excitation data). Therefore, some concepts of lmfit apply directly when using this tool.

To avoid confusion in the further sections and in the source code, please note that the lmfit parameter names are sometimes misleading. For the Lorentzian model[3], the Gaussian model[4] and maybe also other built-in fitting models, the *peak area* is called `amplitude`.

The peak height can be obtained with the variable `height`. This is not a free parameter but it is calculated from the peak area and the peak width. Therefore, it will significantly decrease the fit performance if you set constraints on this parameter. The same applies the parameter `fwhm` which is calculated from the peak width `sigma`.

[1] https://gitlab.cern.ch/MIRACLS/collexc-analysis-and-fitting-tool

[2] https://lmfit.github.io/lmfit-py/index.html

[3] https://lmfit.github.io/lmfit-py/builtin_models.html#lmfit.models.LorentzianModel

[4] https://lmfit.github.io/lmfit-py/builtin_models.html#lmfit.models.GaussianModel

F.2 Peak Shapes

Different peak shapes have been considered to fit the results from collisional excitation measurements and simulation. Figure F.1 shows the peak from a simulated signal with two different fit models, where one can clearly see that the **Gaussian** model is the better choice.

While writing and checking the fit routines for different data sets, it has however been found that the fit algorithm is more stable when a **Lorentzian** model is used for the smaller peaks of $^{25}Mg^{+}$ and $^{26}Mg^{+}$. The reason is that Lorentzian peaks are broader at the base and therefore better incorporate noise and fluctuations into the fit function.

Figure F.2 shows this fit model configuration on experimental data. Again, one can see that the Gaussian model matches better for $^{24}Mg^{+}$ peaks, but for the smaller peaks, the Lorentzian model is fine.

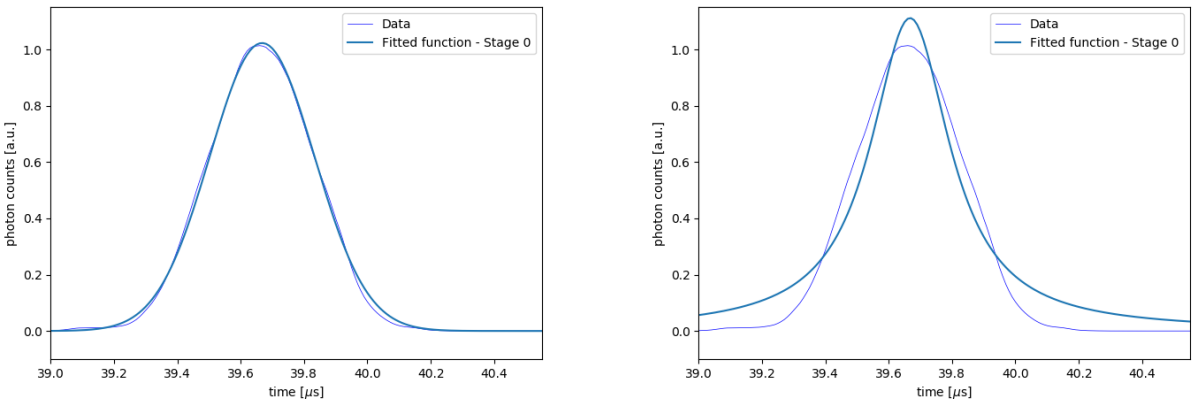

(a) Gaussian fit model *(b) Lorentzian fit model*

Figure F.1: *Simulated collisional excitation peaks with two different fit models.*

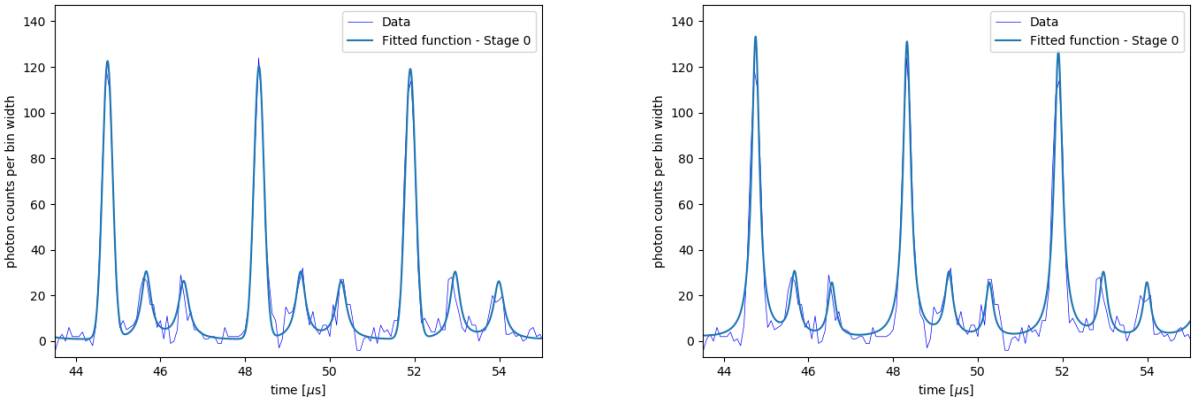

(a) Gaussian model for $^{24}Mg^{+}$ peaks *(b) Lorentzian model for $^{24}Mg^{+}$ peaks*

Figure F.2: *Fit of a collisional excitation measurement with different fit models for the big $^{24}Mg^{+}$ peaks. The smaller peaks of $^{25}Mg^{+}$ and $^{26}Mg^{+}$ have been fitted with a Lorentzian model in both cases.*

F.3 Work flow of the Collisional Excitation Data Fitting Tool

The *Collisional Excitation Data Fitting Tool* is composed of the following components:

1. The first component is the plot scanner, which finds the positions of all peaks and provides initial guesses for all peak parameters. This process is mostly done by an algorithm, the user only has to provide the positions of a few starting peaks.
2. Using the results of the plot scanner, the fitter object creates a fit model and performs the fit. There is a wide range of adjustments that can improve fit performance or the quality of the output.
   The results of each fit are saved to files so that the fitting process does not have to be repeated each time.
3. The fit statistics tool provides utilities to generate plots out of the fit parameter, for example a plot of peak widths for different revolution numbers.

F.3.1 Fitting Experimental Data

The first step in fitting experimental data is a **pre-fit** on a small part of the overall data (e.g. a few tens of revolutions). This pre-fit is used to get better initial parameter values for the fit of the whole data area.

To boost the performance of the fitting procedure, it is possible to split the model into several different parts – so-called **fit stages** – and fit them separately. To avoid unsteady jumps of the fit parameters between adjacent stages, the stages can be configured to overlap by a few revolutions. Figure F.3 shows the complete fit of a collisional excitation measurement that has been split in 11 stages.

For higher numbers of revolution, the peaks of $^{25}Mg^{+}$ and $^{26}Mg^{+}$ get smaller due to losses in the MR-ToF device and eventually fade in with the background noise. Due to the lower statistics (and higher background), this is mostly a problem with lower loading times, as there are fewer ions injected into the MR-ToF apparatus. There are different ways to overcome this problem, depending on the individual situation.

- The parameters of the smaller $^{25}Mg^{+}$ and $^{26}Mg^{+}$ can be estimated by another pre-fit and in the main fit they are fixed parameters that are no longer varied.
- Smaller peaks can be included only in the first fit stages where they are distinguishable from the background.

For measurements with sufficient statistics – usually the measurements with higher loading times – it is possible to fit the complete data set with all peaks from injection to ejection. However, in some cases the fit has to be aborted earlier when even the $^{24}Mg^{+}$ peaks disappear in the background noise.

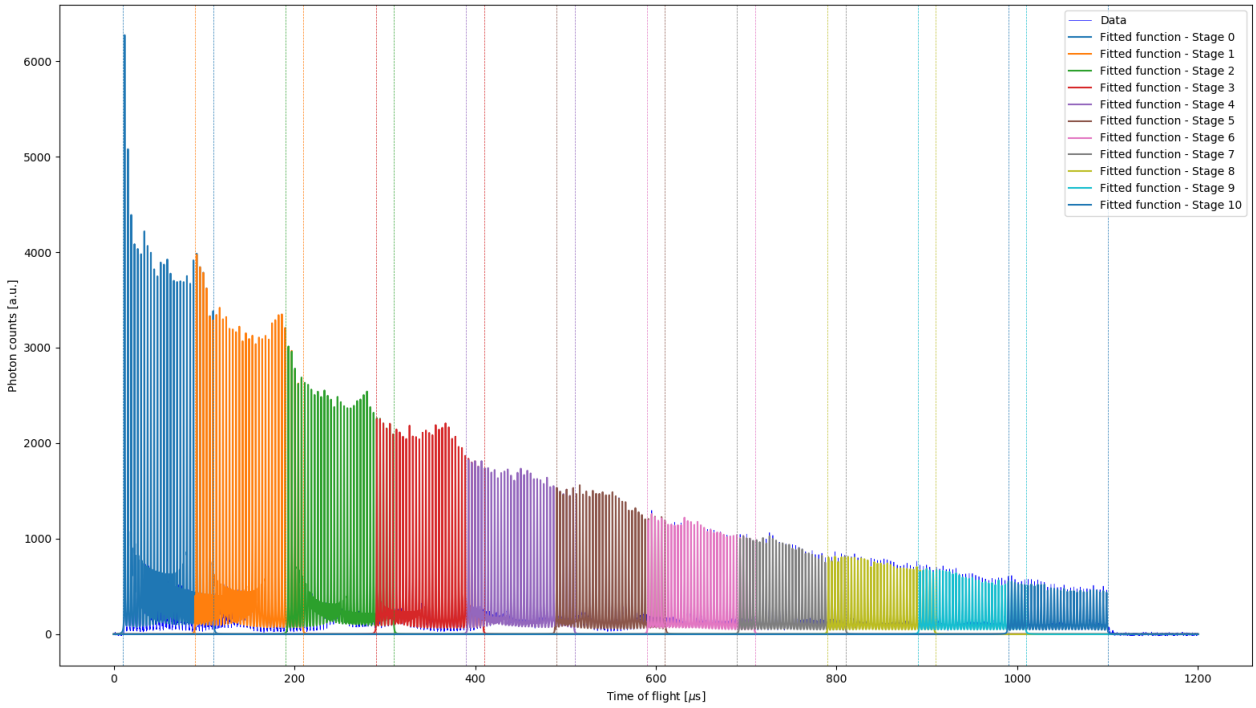

Figure F.3: *Full fit of a collisional excitation measurement. The different fit stages are plotted in different colors. This data has been obtained during the first collisional excitation campaign in March 2019, using a loading time of* 800 µs *and an in-trap lift voltage of* 700 V*.*

F.3.2 Fitting Simulation Data

Fitting the data obtained from simulations is a lot easier. There are significantly less peaks because the simulation is only done for $^{24}Mg^{+}$ and in the simulation, ions are only excited in one flight direction. Moreover, there is no background noise in the simulation. This makes the fitting procedure a lot easier and no pre-fits are required, but in principle fitting still works the same as with experimental data.

F.4 How To Use the Collisional Excitation Data Fitting Tool

F.4.1 Example Usage: Step-by-Step Code

The code below is a minimal example of how to perform a fit with the *Collisional Excitation Data Fitting Tool*. The actual fitting process might be more complicated and involve several steps.

```
from PlotFitter import PlotFitter
from PlotScanner import PlotScanner
```

The x and y data of the plot have to be numpy arrays. In the following code snippet, the plot scanner is created, which searches for peaks and provides initial parameters for the fit. The scanner is configured to look for peaks in the scan area (between x=36 and x=180). The

scan area can be extended to the data area which starts at 9 (start of the peaks) and reaches to the end of the x axis.

```
bin_width = 0.08
model = LorentzianModel
start_of_peaks = 9
scanner = PlotScanner(x, y, bin_width, model, [start_of_peaks],
   scan_area=[36, 180])
```

To scan for a series of peaks, you have to provide the x positions of two starting peaks. The scanner will then look for more peaks assuming that the distance between the peaks stays almost constant. If you have different masses in you data (e.g. 24Mg, 25Mg and 26Mg), you can call this command multiple times. For each scan, a so-called **row** is created. The index of the row and the revolution number is in the prefix of every lmfit fit model.

```
scanner.scanBasedOnTwoPeaks(37.35, 41.1)   # row 0: 24Mg
scanner.scanBasedOnTwoPeaks(38.2, 41.85)   # row 1: 25Mg
scanner.scanBasedOnTwoPeaks(42.8, 46.45)   # row 2: 26Mg
```

The plot scanner has now identified peaks in the scan area. With the following command, the scanner extrapolates to the whole data area (assuming that the distance between the peaks stays constant).

```
scanner.expandToDataArea()
```

The fitter object `PlotFitter` is the wrapper class for lmfit functions. Required parameters of the constructor are the scanner object and a **configuration object** which is described in section F.4.2.

In the example below, we also specify that the data area shall be split in three different stages. The first stage goes from the start of the data to x=300, the second stage goes from x=300 to x=500 and the third stage goes from x=500 to the end of the x axis. Each stage is fitted separately. The stages overlap by a width of 30 on the x axis.

The method `prepareFit` creates the fit model and initializes all the fit parameters. It should be called right after initializing the fitter object.

```
fitter = PlotFitter(scanner, fit_config, stages=[300, 500],
   stage_overlap=30)
fitter.prepareFit()
```

After all the preparation has been done, we can actually start fitting by running the following command. The fit results will be saved `fit_results/fit_result_sample-fit.json` so that the results can be reloaded later. If the parameter `recreate` is set to True, the fit will be recreated and an existing fit result file will be overwritten.

```
fitter.fit(file_name="sample-fit", recreate=False, print_report=
   True)
```

F.4.2 The Fit Parameter Config Object

Basics

A fit parameter configuration object is a dictionary with parameter names as keys. The parameter name can be unique for the whole fit model (apply to all peaks) or only apply to specific rows.

The config object *always* contains at least the following keys:

- `amplitude`: The area of the peak.
- `center`: The peak center (position on the x axis).
- `sigma`: The peak width (but not the FWHM).

The value for each key can either be a dictionary or a list:

- If the value is a **dictionary**, this configuration applies to all peaks
- With a **list of dictionaries**, you can set individual configurations for each **row** (i.e. for each mass in the MR-ToF device). The number of dictionaries in the list has to be exactly the number of rows in the fit model.

A simple example of the configuration object could look like this:

```
fit_config = {
  "amplitude": {...},
  "center": [{...}, {...}, {...}],
  "sigma": {...}
}
```

The config object shown above sets the same configuration for all peak areas and widths, but specifies different configurations for the peak center of each row.

Configuration of a Fit Parameter

Configuring a parameter works similar as in lmfit directly. Check out the lmfit Parameter documentation[5] for reference.

You can set the following keys to configure a fit parameter:

- `val`: Initial value of the fit parameter. The same as lmfit's `value`. If `val` is not defined, a guess is used as initial value for the fit parameter.
- `min`, `max`: Bounds for the parameter, same as in lmfit.
- `range`: Set parameter bounds to interval $(val - range, val + range)$.
- `dev`: Set parameter bounds to interval $(val \cdot (1 - range), val \cdot (1 + range))$.
- `vary`: Boolean value: if False, the parameter is not a variable in the fit (default is True), same as in lmfit.

[5] https://lmfit.github.io/lmfit-py/parameters.html

- `expr`: Mathematical expression (as a string) that defines this parameter with respect to other fit parameters. See below for further information.

Except for `vary` and `expr`, all these keys can either have a number (`int` or `float`) or a function of the peak index as a value. The peak index is an integer starting with 0 at the leftmost peak of each row.

Expressions

You can use mathematical expressions to define the value of a parameter. This is a feature of lmfit. For example, the parameter `fwhm` of the Gaussian model is constrained to the parameter `sigma` with $fwhm = 2\sigma \cdot \sqrt{2 \cdot \ln 2}$.

There are three additional keywords introduced in the *Collisional Excitation Data Fitting Tool*. These are specifically designed to work with many peaks in different rows:

- `[INDEX]` will be replaced with the index of the peak in each expression. The peak index is an integer starting with 0 at the leftmost peak of each row.
- `[ROW]` will be replaced with the index of the peak's row in each expression.
- `[REF]` name of the **reference parameter**.

If the expression does not contain the keyword `[REF]`, specifying an expression overrides all other configuration.

If the expression contains the keyword `[REF]`, the parameter of one peak will be the **reference parameter**. This parameter's name will be pasted into all other expressions of the same data row and replace the keyword `[REF]`.

Keys like initial value and bounds will only apply to the reference parameter if there is one. The reference parameter is either the peak where the scan started or just the peak with index 0.

Additional Fit Parameters

If needed in the expressions, further fit parameters can be defined by adding configuration for them. Additional parameters can either be unique for the whole fit model or for each row. The keyword `[ROW]` is the only one that can also be applied to parameter names.

Debugging

If you want to debug your configuration or just find out what is going on, set the flag `print_vars` of `PlotFitter.fit()` to `True`. You then get an output like in figures F.4 and F.5.

Example of a Fit Config Object

The following example could be used to fit collisional excitation data with three masses (therefore three rows in the fit model). It uses many of the options described above.

Name	Value	Min	Max	Stderr	Vary	Expr	Brute_Step
offset_0_c	0	-inf	inf	0	False	None	None
p0_peak_dist	7.167	-inf	inf	2.247e-05	True	None	None
p0_rev00_amplitude	1.502	-inf	inf	0.03415	True	None	None
p0_rev00_center	10.08	-inf	inf	0.0005441	False	p0_rev06_center + p0_peak_dist * -6	None
p0_rev00_fwhm	0.3047	-inf	inf	0.009802	False	2.0000000*p0_rev00_sigma	None
p0_rev00_height	3.138	-inf	inf	0.07123	False	0.3183099*p0_rev00_amplitude/max(1.e-15, p0_rev00_sigma)	None
p0_rev00_sigma	0.1524	0	inf	0.004901	True	None	None
p0_rev01_amplitude	2.987	-inf	inf	0.03406	True	None	None
p0_rev01_center	17.25	-inf	inf	0.0005248	False	p0_rev06_center + p0_peak_dist * -5	None
p0_rev01_fwhm	0.3044	-inf	inf	0.004908	False	2.0000000*p0_rev01_sigma	None
p0_rev01_height	6.247	-inf	inf	0.07124	False	0.3183099*p0_rev01_amplitude/max(1.e-15, p0_rev01_sigma)	None
p0_rev01_sigma	0.1522	0	inf	0.002454	True	None	None
p0_rev02_amplitude	2.977	-inf	inf	0.03404	True	None	None
p0_rev02_center	24.42	-inf	inf	0.0005058	False	p0_rev06_center + p0_peak_dist * -4	None
p0_rev02_fwhm	0.304	-inf	inf	0.004915	False	2.0000000*p0_rev02_sigma	None
p0_rev02_height	6.234	-inf	inf	0.07128	False	0.3183099*p0_rev02_amplitude/max(1.e-15, p0_rev02_sigma)	None
p0_rev02_sigma	0.152	0	inf	0.002458	True	None	None
p0_rev03_amplitude	2.969	-inf	inf	0.03403	True	None	None
p0_rev03_center	31.58	-inf	inf	0.000487	False	p0_rev06_center + p0_peak_dist * -3	None
p0_rev03_fwhm	0.3038	-inf	inf	0.004924	False	2.0000000*p0_rev03_sigma	None
p0_rev03_height	6.222	-inf	inf	0.0713	False	0.3183099*p0_rev03_amplitude/max(1.e-15, p0_rev03_sigma)	None
p0_rev03_sigma	0.1519	0	inf	0.002462	True	None	None
p0_rev04_amplitude	2.969	-inf	inf	0.03403	True	None	None
p0_rev04_center	38.75	-inf	inf	0.0004686	False	p0_rev06_center + p0_peak_dist * -2	None
p0_rev04_fwhm	0.3038	-inf	inf	0.004924	False	2.0000000*p0_rev04_sigma	None
p0_rev04_height	6.221	-inf	inf	0.0713	False	0.3183099*p0_rev04_amplitude/max(1.e-15, p0_rev04_sigma)	None
p0_rev04_sigma	0.1519	0	inf	0.002462	True	None	None

Figure F.4: *Fit parameters of row 0 generated with example 1. The reference parameter for the peak center is the center of peak 6 (highlighted in blue). The index (yellow) is relative to the reference parameter. The peak distance (green) is a common parameter for all peaks of row 0 (indicated by the prefix `p0_`.*

Example 1

- All peak areas (called `amplitude` in lmfit) and peak widths (called `sigma`) shall be fitted without contraints. This is indicated by the empty dictionaries.
- The peak centers should have a constant distance for *all* rows. The `[REF]` in this expression works as constant offset for the peak centers.
- The additional parameter `[ROW]peak_dist` will create three fit parameters for the distance between the peaks of each row.: `p0_peak_dist`, `p1_peak_dist` and `p2_peak_dist` .

```
fit_config = {
  "amplitude":          {},
  "center":             {"expr": "[REF] + [ROW]peak_dist * [INDEX]"
     },
  "sigma":              {},
  "[ROW]peak_dist":     {}
}
```

Figure F.4 shows a part of the fit parameters generated with this example configuration.

Example 2

- The parameters `amplitude` and `sigma` are defined differently for each row. Both parameters are completly free for row 0 (which could be 24Mg).
- The peak areas `amplitude` of the rows 1 and 2 (which could be the less intense peaks for 25Mg and 26Mg) will all have the same reference value in the fit. The minimum for the reference value is 0.
- The peak widths `sigma` of the rows 1 and 2 will all have the same reference value in the fit. They may not deviate by more than 50% from the initial guess.

Name	Value	Min	Max	Stderr	Vary	Expr	Brute_Step
p1_rev00_amplitude	32.96	0	inf	1.357	True	None	None
p1_rev00_center	7.846	-inf	inf	0	False	None	None
p1_rev00_fwhm	0.2565	-inf	inf	0.01213	False	2.3548200*p1_rev00_sigma	None
p1_rev00_height	120.7	-inf	inf	4.906	False	0.3989423*p1_rev00_amplitude/max(1.e-15, p1_rev00_sigma)	None
p1_rev00_sigma	0.1089	0.04	0.12	0.005149	True	None	None
p1_rev01_amplitude	32.96	-inf	inf	1.357	False	p1_rev00_amplitude	None
p1_rev01_center	11.31	-inf	inf	0	False	None	None
p1_rev01_fwhm	0.2565	-inf	inf	0	False	2.3548200*p1_rev01_sigma	None
p1_rev01_height	120.7	-inf	inf	0	False	0.3989423*p1_rev01_amplitude/max(1.e-15, p1_rev01_sigma)	None
p1_rev01_sigma	0.1089	0	inf	0.005149	False	p1_rev00_sigma	None
p1_rev02_amplitude	32.96	-inf	inf	1.357	False	p1_rev00_amplitude	None
p1_rev02_center	14.78	-inf	inf	0	False	None	None
p1_rev02_fwhm	0.2565	-inf	inf	0	False	2.3548200*p1_rev02_sigma	None
p1_rev02_height	120.7	-inf	inf	0	False	0.3989423*p1_rev02_amplitude/max(1.e-15, p1_rev02_sigma)	None
p1_rev02_sigma	0.1089	0	inf	0.005149	False	p1_rev00_sigma	None
p1_rev03_amplitude	32.96	-inf	inf	1.357	False	p1_rev00_amplitude	None
p1_rev03_center	18.25	-inf	inf	0	False	None	None
p1_rev03_fwhm	0.2565	-inf	inf	0	False	2.3548200*p1_rev03_sigma	None
p1_rev03_height	120.7	-inf	inf	0	False	0.3989423*p1_rev03_amplitude/max(1.e-15, p1_rev03_sigma)	None
p1_rev03_sigma	0.1089	0	inf	0.005149	False	p1_rev00_sigma	None
p1_rev04_amplitude	32.96	-inf	inf	1.357	False	p1_rev00_amplitude	None
p1_rev04_center	21.71	-inf	inf	0	False	None	None
p1_rev04_fwhm	0.2565	-inf	inf	0	False	2.3548200*p1_rev04_sigma	None
p1_rev04_height	120.7	-inf	inf	0	False	0.3989423*p1_rev04_amplitude/max(1.e-15, p1_rev04_sigma)	None
p1_rev04_sigma	0.1089	0	inf	0.005149	False	p1_rev00_sigma	None

Figure F.5: *Fit parameters of row 1 generated with example 2. The parameters* `sigma` *and* `amplitude` *of the first peak are reference parameters. In this case, this means that all other peaks of this row are fixed to these reference values. You can see that the property* `vary` *is set to* `False` *for* `sigma` *and* `amplitude` *of all other peaks.*

- The peak centers are fixed to the initial values. They are not varied in the fit.

```
ampl_config = {"expr": "[REF]", "min": 0}
sigma_config = {"expr": "[REF]", "dev": 0.5}

fit_params_stage_2 = {
  "amplitude":  [{}, ampl_config, ampl_config],
  "center":     {"vary": False},
  "sigma":      [{}, sigma_config, sigma_config]
}
```

Figure F.5 shows a part of the fit parameters generated with this example configuration.

F.4.3 Further Options and Functions

Below you can find a few more suggestions on how to work with the fitting tool.

Do a fit in multiple steps: Scan a small area, fit this area, use the fit for a new scan, fit again, and so on. This is particularly useful when you want to determine some parameters in a prefit and fix them in the next fit.

As opposed to providing the positions of two starting peaks, you can use a fit result to initialize a new, more accutrate scan. The following code takes all peaks of a fitter object and scans a bigger data area based on these inital peaks. The data area is defined in the constructor of the scanner object.

```
scanner2.scanBasedOnFit(fitter)
scanner2.expandToDataArea()
```

Adapt the trend of a fit: The intensity of rarer isotopes may decrease during the measurement and eventually disappear in the background noise. This fitting tool provides the

option to abort the fit after a few stages and analyze the results already obtained. Based on that, all parameters of a row can be fixed so that they are no longer varied in the next fits.

In the example below, the peak area and peak width of the rows 1 and 2 (in this example 25Mg and 26Mg) are fixed after the first three fit stages. For all the following stages, these parameters are extrapolated and fixed as well. The row 0 (24Mg) is not altered. After this process, all stages are fitted again.

```
fitter.fit(file_name="sample-fit-pre", stages=range(3))

fitter.adaptTrend("sigma", [1, 2])
fitter.adaptTrend("amplitude", [1, 2])

fitter.fit(file_name="sample-fit")
```

Bibliography

1. Malbrunot-Ettenauer, S., Blaum, K., Nörtershäuser, W., Schweikhard, L. & Wienholtz, F. *Letter of Intent to the ISOLDE and Neutron Time-of-Flight Committee Benchmarking of a Multi Ion Reflection Apparatus for Collinear Laser Spectroscopy of radionuclides May 31* in (2017).
2. Wolf, R. *et al.* ISOLTRAP's multi-reflection time-of-flight mass separator/spectrometer. *International Journal of Mass Spectrometry* **349-350.** 100 years of Mass Spectrometry, 123–133. ISSN: 1387-3806 (2013).
3. Lechner, S. *et al. Flourescence Detection as a new Diagnostics Tool for Electrostatic Ion Beam Traps* 2019.
4. Jonson, B. & Riisager, K. The ISOLDE facility. *Scholarpedia* **5.** revision #90796, 9742 (2010).
5. *ISOLDE: Facility* http://isolde.web.cern.ch/facility (2019).
6. Jonson, B. & Richter, A. More than three decades of ISOLDE physics. *Hyperfine Interactions* **129,** 1–22. ISSN: 1572-9540 (2000).
7. Catherall, R. *et al.* The ISOLDE facility. *Journal of Physics G: Nuclear and Particle Physics* **44,** 094002 (2017).
8. Demtröder, W. *Experimentalphysik 3: Atome, Moleküle und Festkörper* ISBN: 9783662490945. https://books.google.ch/books?id=tR5kDAAAQBAJ (Springer Berlin Heidelberg, 2016).
9. Yordanov, D. T. *From ^{27}Mg to ^{33}Mg: transition to the Island of inversion* PhD thesis (KU Leuven, Faculteit Wetenschappen, Departement Natuurkunde an Sterrenkunde, Instituut voor Kern- en Stralingsfysica, 2007).
10. Blaum, K., Dilling, J. & Nörtershäuser, W. Precision Atomic Physics Techniques for Nuclear Physics with Radioactive Beams. *Physica Scripta Volume T* **T152.** doi:10.1088/0031-8949/2013/T152/014017 (2012).
11. Garcia Ruiz, R. F. *et al.* Unexpectedly large charge radii of neutron-rich calcium isotopes. *Nature Physics* **12,** 594–598 (2016).
12. Cheal, B. & Flanagan, K. Progress in laser spectroscopy at radioactive ion beam facilities. *Journal of Physics G: Nuclear and Particle Physics* **37,** 113101 (2010).
13. Nörtershäuser, W. & Geppert, C. in *The Euroschool on Exotic Beams, Vol. IV* (eds Scheidenberger, C. & Pfützner, M.) 233–292 (Springer Berlin Heidelberg, Berlin, Heidelberg, 2014). ISBN: 978-3-642-45141-6. doi:10.1007/978-3-642-45141-6_6. https://doi.org/10.1007/978-3-642-45141-6_6.

14. Paul, W. Electromagnetic traps for charged and neutral particles. *Rev. Mod. Phys.* **62,** 531–540 (3 1990).

15. Petrascheck, D. & Schwabl, F. *Elektrodynamik* ISBN: 9783662481806. https://books.google.ch/books?id=eSA3CwAAQBAJ (Springer Berlin Heidelberg, 2015).

16. Herfurth, F. & Blaum, H. K. *Trapped Charged Particles and Fundamental Interactions* ISBN: 978-3-540-77816-5. doi:https://doi.org/10.1007/978-3-540-77817-2 (Springer, Berlin Heidelberg, 2008).

17. Kriesch, A. *Wikimedia Commons: File:Paul-Trap.svg* This file is licensed under the Creative Commons Attribution-Share Alike 3.0 Unported license. https://commons.wikimedia.org/wiki/File:Paul-Trap.svg (2019).

18. Zajfman, D. *et al.* Electrostatic bottle for long-time storage of fast ion beams. *Physical Review A - PHYS REV A* **55.** doi:10.1103/PhysRevA.55.R1577 (1997).

19. Wolf, R. N., Eritt, M., Marx, G. & Schweikhard, L. A multi-reflection time-of-flight mass separator for isobaric purification of radioactive ion beams. *Hyperfine Interactions* **199,** 115–122. ISSN: 1572-9540 (2011).

20. Wolf, R. N., Marx, G., Rosenbusch, M. & Schweikhard, L. Static-mirror ion capture and time focusing for electrostatic ion-beam traps and multi-reflection time-of-flight mass analyzers by use of an in-trap potential lift. *International Journal of Mass Spectrometry* **313,** 8–14. ISSN: 1387-3806 (2012).

21. Sels, S. *et al.* First steps in the development of the Multi Ion Reflection Apparatus for Collinear Laser Spectroscopy. *Nuclear Instruments and Methods in Physics Research Section B: Beam Interactions with Materials and Atoms.* ISSN: 0168-583X. doi:https://doi.org/10.1016/j.nimb.2019.04.076. http://www.sciencedirect.com/science/article/pii/S0168583X19302605 (2019).

22. *Longer term LHC schedule* https://lhc-commissioning.web.cern.ch/lhc-commissioning/schedule/LHC-long-term.htm (2019).

23. Leo, W. R. *Techniques for Nuclear and Particle Physics Experiments A How-to Approach* ISBN: 978-3-642-57920-2 (Springer, Berlin Heidelberg, 1994).

24. *Wikimedia commons: File:Photomultiplier schema en.png* This work has been released into public domain by the author. https://commons.wikimedia.org/wiki/File:Photomultiplier_schema_en.png (2019).

25. *Wikimedia commons: File:Mcp-de.svg* This work has been released into public domain by the author. https://commons.wikimedia.org/wiki/File:Mcp-de.svg (2019).

26. *ETP Ion Detect homepage* https://www.etp-ms.com/ (2019).

27. *A New Class of Robust Sub-nanosecond TOF Detectors with High Dynamic Range* Presented at the 54th ASMS Conference on Mass Spectroscopy, Seattle, Washington, 2006 (Sydney, 2006). https://www.etp-ms.com/file-repository/26.

28. *MagneTOF^{TM}: A New Class of Robust Sub-nanosecond TOF Detectors with Exceptional Dynamic Range* Product Data. 2013. https://www.etp-ms.com/file-repository/8.

29. Maier, F. M. *Laser Spectroscopy of Short-Lived-Radionuclides in an Ion Trap: MIR-ACLS' proof-of-principle experiment and the simulation of the future 30-keV MR-ToF device* Master's Thesis (Johannes Kepler University Linz, Altenbergerstraße 69, 4040 Linz, Austria, 2019).

30. A. Kramida, Yu. Ralchenko, J. Reader & and NIST ASD Team. NIST Atomic Spectra Database (ver. 5.6.1), [Online]. Available: `https://physics.nist.gov/asd` [2019, July 29]. National Institute of Standards and Technology, Gaithersburg, MD. 2018.

31. Pedersen, H. B. *et al.* Diffusion and synchronization in an ion-trap resonator. *Phys. Rev. A* **65,** 042704 (4 2002).

32. Pedersen, H. B. *et al.* Ion Motion Synchronization in an Ion-Trap Resonator. *Phys. Rev. Lett.* **87,** 055001 (5 2001).

33. Breitenfeldt, C. *et al.* Spreading times of ion-bunches in the Cryogenic Trap for Fast ion beams. *International Journal of Mass Spectrometry* **396,** 1–4. ISSN: 1387-3806 (2016).

34. Strasser, D. *et al.* Negative Mass Instability for Interacting Particles in a 1D Box: Theory and Application. *Phys. Rev. Lett.* **89,** 283204 (28 2002).

35. *MagneTOF^{TM} C Detector Application Notes* 2015.

36. Fischer, L. *Improvements of the beam intensity of stable Mg ions for the proof-of-principle experiment of Collinear Laser Spectroscopy on short-lived nuclides in a Multi Ion Reflection Apparatus* Bachelor's Thesis (Karlsruhe Institute of Technology, 2018).

37. Kreim, K. *et al.* Nuclear charge radii of potassium isotopes beyond N=28. *Physics Letters B* **731,** 97–102. ISSN: 0370-2693 (2014).

38. Sailer, S. *Improvements of the Optical Detection Setup for Collinear Laser Spectroscopy of Short-Lived Radioactive Nuclides and Spectroscopic Studies on the Hyperfine Parameters of ^{208}Bi* Master's Thesis (Technische Universität München, Physics Department, 2016).

39. Maier, F. M. *et al.* Simulations of a proof-of-principle experiment for collinear laser spectroscopy within a multi-reflection time-of-flight device. *Hyperfine Interactions* **240,** 54. ISSN: 1572-9540 (2019).

40. *SIMION Homepage* `https://simion.com/` (2019).

41. Manura, D. J. & Dahl, D. A. *SIMION® Version 8.0/8.1 User Manual* 5th ed. Scientific Instrument Services, Inc. (2011).

42. IAEA Nuclear Data Section. *LiveChart of Nuclides* `https://www-nds.iaea.org/relnsd/vcharthtml/VChartHTML.html` (2019).

43. Zinkstok, R. T., van Duijn, E., Witte, S. & Hogervorst, W. H. *Hyperfine structure and isotope shift of transitions in Yb I using UV and deep-UV cw laser light and the angular distribution of fluorescence radiation* in (2002).